TESIS DE DOCTORADO

Thermoelectric Properties of SrTiO$_3$ and CaTiO$_3$ Thin Films

Alexandros Sarantopoulos

SANTIAGO DE COMPOSTELA

AÑO 2018

DECLARACIÓN DEL AUTOR DE LA TESIS

Thermoelectric Properties of SrTiO$_3$ and CaTiO$_3$ Thin Films

D. Alexandros Sarantopoulos

Presento mi tesis, siguiendo el procedimiento adecuado al Reglamento, y declaro que:

1) *La tesis abarca los resultados de la elaboración de mi trabajo.*
2) *En su caso, en la tesis se hace referencia a las colaboraciones que tuvo este trabajo.*
3) *La tesis es la versión definitiva presentada para su defensa y coincide con la versión enviada en formato electrónico.*
4) *Confirmo que la tesis no incurre en ningún tipo de plagio de otros autores ni de trabajos presentados por mí para la obtención de otros títulos.*

En Santiago de Compostela, 14 de Noviembre de 2018

Fdo

AUTORIZACIÓN DEL DIRECTOR / TUTOR DE LA TESIS

Thermoelectric Properties of SrTiO$_3$ and CaTiO$_3$ Thin Films

D. José Francisco Rivadulla Fernández

INFORMA:

Que la presente tesis, corresponde con el trabajo realizado por D Alexandros Sarantopoulos, bajo mi dirección, y autorizo su presentación, considerando que reúne los requisitos exigidos en el Reglamento de Estudios de Doctorado de la USC, y que como director de ésta no incurre en las causas de abstención establecidas en Ley 40/2015.

En Santiago de Compostela, 14 de Noviembre de 2018

Fdo

Acknowledgements

First and foremost, I would like to thank the director of my thesis, Prof. Francisco Rivadulla. I feel very lucky for the opportunity that he gave me to take on this challenging project, and I hope that I have justified his decision. I am very grateful to have been learning from him every day, not only in the lab, but in every aspect of life. He has been an example of scientific insight, hard work and attention to detail. Great part of my growth as a scientist and a human being, is undoubtedly owed to him.

I want to thank all of my work colleagues, starting from the first ones that I met when I joined this lab, Bea, Camilo, Elías, José and Víctor. I thank you for making me feel welcome here, and for showing me the ways of the lab-life. I want to especially thank Víctor for all the solutions that he has provided during these years, in and outside the lab. I also want to thank the newer members of this group, Carlos, David, Daniela, Eric, Lucia and Tinh. Thank you for all the help and support during this challenging period.

I would also like to thank Prof. Jonathan A. Malen for allowing me to be a part of his group, during my two visits to the department of Mechanical Engineering at the Carnegie Mellon University. I appreciate the opportunity to learn another valuable skill and enhance the content of my thesis. Moreover, I want to thank Wee-Liat, Dipanjan, Kevin and Minyoung for taking me in the group and making me feel welcome.

I want to thank all the people in Santiago de Compostela who have been a part of a fun group. LAR for sharing his incomparable knowledge in drumming, María José, Sabela, Ana and Pablo for the fun conversations and concert attending. I also want to thank Ana, Adri, Diego, Cati, Eva and Josiño for being the first group of friends to welcome me in Santiago.

Furthermore I want to thank Lolo, one of my closest friends here in Santiago. Thank you for always being there for me, and for all the deep, fun and weird conversations that we have had. Moreover, I am grateful for a long-lasting friendship with Nikos K.

Even though we have lived in different countries for so many years, it's like you have always been beside me, and I thank you for that. Also, I would like to thank A. for helping me find my balance during the most troubling times.

I want to especially thank Inés for the incredible time that we have spent together. I am very grateful to you for all the love that you have given me and for making Santiago feel like home. *Quérote moito, Inesita.*

Last but not least, I want to thank my family, for all the love and support that they have given me all these years. To my parents Dimitris and Spyridoula, I wouldn't have been here without you. To my brother Christos and his wife Lila, thank you for all your support and great time that we have had together. And of course, I want to give my warmest welcome to the newest members of their family, Dimitris and Harry. I can't wait to see you more and be the most fun uncle!

Abstract

The rapid development of technology has been accompanied by a huge increase in energy consumption, which requires the implementation of newer, more efficient energy sources, replacing the environmentally hostile industry of fossil fuels. One promising class of renewable energy is thermoelectricity, which can take advantage of the enormous amount of energy wasted in the form of heat. A necessary development is the discovery of new thermoelectric devices based on materials that are safe for the environment and the users. A class of promising materials are the oxide-based perovskites, such as $SrTiO_3$ and $CaTiO_3$.

Moreover, the vast improvement of the physical deposition techniques in the last decades has permitted the fabrication of atomically precise nanostructures, such as thin films, which exhibit high quality crystal structure and interfaces. One of the advantages of the nanostructures is that their reduced dimensionality alters their functional properties, opening new windows of designing and obtaining more efficient systems, compared to their bulk counterparts.

In this thesis we are studying the transport and thermoelectric properties of two different oxide-based perovskites, the $SrTiO_3$ and $CaTiO_3$, in the form of thin films, fabricated in a pulsed laser deposition system. We begin by studying how making changes in the deposition process parameters can influence the structural properties of the thin films, and how this structural modification can influence their transport and electronic properties. We examine the role of incorporated anionic/cationic defects and epitaxial strain on the thermoelectric power and the appearance of a magnetic phase, and compare these results to systems based on oxide interfaces, discussing the origin of these behaviors.

Moreover, we study the thermal transport in thin films with different degrees of epitaxial strain and how the structural distortion and a ferroelectric transition can lead to a large decrease of the

thermal conductivity. In addition, we study the structural requirements that could lead to, or prevent a ferroelectric phase transition, and how the manipulation of oxygen vacancies can lead to a similar phenomenology to that of an established ferroelectric state.

Contents

Motivation

The beginning of the new century has been marked from an exponential growth in technology, which has provided humanity with faster, smaller, and more capable devices, present in everyday life. However, this exponential increase in the use of, mostly, electronic devices has been accompanied by enormous power consumption which, unfortunately, still depends on traditional means of energy production, such as fossil fuels, endangering the environment. It is of utmost importance to seek more efficient ways of producing cleaner, cost-efficient and reliable renewable energy sources.

A great effort has been made the last 15 years in creating electricity from solar and wind energy, however in the majority of energy consumption/conversion processes, there is a vast amount of energy lost in the form of heat. This energy can be harvested by thermoelectric materials. Thermoelectric power (or Seebeck coefficient) is the property of conducting materials, where a voltage difference appears as a consequence of a temperature gradient in the absence of any electrical current (open circuit conditions). Essentially, the heat current flowing across the material produces an asymmetry in the electron/hole distribution at the hot/cold side of the material, thus creating this voltage difference.

The efficiency of the thermal-to-electrical energy, commonly known as thermoelectric effect, is evaluated by the dimensionless *figure of merit* , zT, which is defined as $zT = \frac{S^2\sigma}{\kappa}T$, where S is the Seebeck coefficient, σ the electrical conductivity, κ the thermal conductivity and T is the absolute temperature. Commercial thermoelectric devices need at least a value of $zT \approx 1$. Nowadays, the

materials that present zT values on that range are mainly constituted by post-transition metal elements, like Pb, Sb and Te, that are prone to degradation or evaporation at high temperatures and are, in some cases, toxic. Therefore, their replacement by other types of materials is highly desirable. However, the design of efficient thermoelectric (TE) materials is not an easy task. In order to improve the zT value, a material needs to have a high Seebeck coefficient (low density carrier semiconductors), high electrical conductivity (metals) and low thermal conductivity (mostly insulators).

Unfortunately, these three parameters are not easily disentangled, which leaves as the best option doped semiconductor materials. Normally, the carrier concentration is tuned via doping, which would affect both the electrical conductivity as well as the Seebeck coefficient, and the thermal conductivity can be reduced by means of incorporated defects or reduced dimensionality. A promising family of semiconductor materials are the oxide-based perovskite materials, which present many advantages, like thermal and electrical stability, and great chemical versatility, which made them the subject of extensive study during the last decades.

The recent technological advances in the fabrication of materials via physical deposition methods such as Molecular Beam Epitaxy (MBE), Pulsed Laser Deposition (PLD), Atomic Layer Deposition (ALD) or Sputtering, have permitted the atomically precise control of the composition and the geometry of oxides, opening a new window in the improvement of their functional properties. Thin film fabrication has been one of the most prominent ways of tailoring the properties of these materials, and combined with their reduced dimensionality, can give way to a lot of exciting properties. Now it is possible to fabricate atomically precise monolayers, thin films, multilayers, or superlattices, where many interesting phenomena take place.

One of the most interesting materials in the oxide perovskite family is the strontium titanate (SrTiO$_3$ or STO). It has been widely used both as a substrate for the epitaxial deposition of numerous different oxides, as well as a standalone functional mate-

rial. In fact, it was the first oxide to present superconductivity at very low temperature [1] almost 50 years ago. In its bulk form, STO is a diamagnetic, quantum paraelectric insulator, with an indirect/direct bandgap of 3.2/3.75 eV and a very large dielectric constant (up to 10^4 at very low temperature). [2, 3] It can easily be turned conductive either by cationic (La, Nb) or anionic ($SrTiO_{3-\delta}$) doping, even by a small percentage. It has been reported to present ferromagnetic behavior, ferroelectricity and also has been used as the base material for resistive switching applications. [4, 5, 6]

Reducing its dimensionality, has lead to huge increase in its thermoelectric power [7, 8], making it a serious candidate for thermoelectric applications. Its chemical stability allows for a numerous different tailoring of its properties, since apart from doping, it is easy to manipulate its lattice parameters and its unit cell dimensions, either by strain engineering or manipulating the TiO_6 octahedral rotations. Moreover, the interface with $LaAlO_3$ develops a two-dimensional electron gas (2DEG) [9], with abnormally high electron mobility.

Another interesting (and very close) perovskite is calcium titanate ($CaTiO_3$ or CTO). In its stoichiometric state, CTO is an insulating material, however it can become electrically conductive when it is oxygen deficient, or by cation replacement. It has been reported to be incipient ferroelectric material, such as STO, where a ferroelectric state can be stabilized through strain engineering. [10, 11, 12] Moreover, the formation of a 2DEG has been reported at its interface with $YTiO_3$ as well as at its bare surface. [13, 14] This versatile behavior of CTO can open many possibilities for the fabrication of functional devices or even be incorporated in more complex oxide systems.

The scope of this thesis is to study the fundamental electrical and thermal transport properties of these two Ti-based perovskite oxides and investigate how deliberate changes on their thin-film growth conditions, cationic /anionic vacancies, and other structural parameters related to epitaxial stress relaxation during growth, can ultimately affect their functional properties. We will start by inves-

tigating how strain engineering and deliberate defect incorporation, changes the behavior of STO thin films and how we can manipulate their structure in order to understand their effect on thermoelectric response of this material. In addition, we will present the results of the study of CTO, where we study the differences compared to STO. Finally, we also performed a complete study of the thermal conductivity of such films, particularly on how strain engineering, as well as different structural parameters and cationic/anionic defects affect their thermal transport.

Chapter 1

Introduction

In this chapter we present the recent advances in the deposition of complex oxides and heterostructures, focusing in the famous LaAlO$_3$/SrTiO$_3$ (LAO/STO) interface, and the fascinating properties that emerge from these heterostructures. The main theoretical explanations about the mechanism behind these phenomena is being discussed, as well as the similarity with the properties of simple thin-film oxides. We also show how to derive the transport coefficients on the basis of the Boltzmann transport equation, in order to understand the electrical and transport experiments discussed in this thesis. We will describe with more detail the theory of the thermal conductivity, to discuss how the structural factors can heavily affect the thermoelectric (TE) behavior of oxide thin films.

1.1 The LaAlO$_3$/SrTiO$_3$ interface & the two-dimensional electron gas (2DEG)

During the last two decades, there has been a great advance in the control of the deposition processes that allows the fabrication of atomically precise surfaces and interfaces. The progress made has been so significant that complex structures can be man-

ufactured on demand, and study phenomena previously predicted using first-principle calculations. This control of the deposition methods allowed the fabrication of atomically smooth interfaces between different materials, including oxides, enabling the emergence of surprising phenomena, such as the appearance of a metallic interface between two insulating materials, enhanced magnetoresistivity, ultra-thin magnetic layers and phase transition from superconducting to insulating, among others. [15]

In 2004 Ohtomo & Hwang [9] reported the formation of a two-dimensional electron gas (2DEG) of extremely high mobility ($\approx$ 10.000 cm^{2}V^{-1}s^{-1}) at the interface between SrTiO$_3$ and LaAlO$_3$ (STO and LAO), two insulating oxides. STO is an interesting, apparently simple oxoperovskite, with a very large variety of properties and functionalities, mostly linked to small deviations from stoichiometry. When stoichiometric, it has a cubic crystal structure at room temperature, and it is a robust electrical insulator ($E_g = 3.2 - 3.75eV$) [2] with a large dielectric constant ($\varepsilon_r(298K) \approx 300$). [3] When it is subjected to tensile strain, it becomes ferroelectric, due to rotations of the TiO$_6$ octahedra. [5] Moreover, it can be easily doped either by cation substitution (La^{3+} for Sr^{2+} and Nb^{5+} for Ti^{4+}, for example) or by oxygen reduction (SrTiO$_{3-\delta}$), exhibiting metallic behavior in both cases. [16, 17, 18]

LAO is also a perovskite insulator with a large bandgap ($E_g = 5.6eV$) and rhombohedral crystal structure at room temperature. Its pseudocubic lattice parameter of 3.79Å makes for $\approx$ 2.9% of mismatch with respect to the 3.905Å lattice parameter of the STO.

In order to fabricate a functional LAO/STO interface, several unit cells of LAO are deposited on top of a (001)-oriented STO single crystal substrate. In general, the STO substrates have a mixed surface termination, mainly due to the cutting and polishing procedure that leaves a miscut angle between the crystallographic axes and the polishing angle. Several techniques have been proposed to obtain a single chemical termination, that is, pure SrO or TiO$_2$. These methods consist in a series of wet etching and thermal treatments. [19, 20, 21] Having a TiO$_2$ terminated STO surface is crucial

to obtain a conductive LAO/STO interface.

The LAO/STO interface is constructed normal to the [001] crystallographic axes of the two materials (see Fig. 1.1). Assuming an ionic picture for both oxides, we could see STO as an alternating stacking of charge-neutral $(Sr^{2+}O^{2-})^0$ and $(Ti^{4+}O_2^{2-})^0$ planes along the [001] direction. On the other hand, the stacking in LAO is of $(La^{3+}O^{2-})^{+1}$ and $(Al^{3+}O_2^{2-})^{-1}$ charged planes. Therefore, growing LAO on top of TiO_2-terminated STO will result in a polar $(TiO_2)^0/(La^{3+}O^{2-})^{+1}$ interface. This discontinuity produces a metallic interface (n-type) when a critical thickness of ≈ 4 unit cells of LAO are grown on STO. On the other hand, depositing LAO on top of SrO-terminated STO results in insulating interface, irrespective of the thickness.[9, 22]
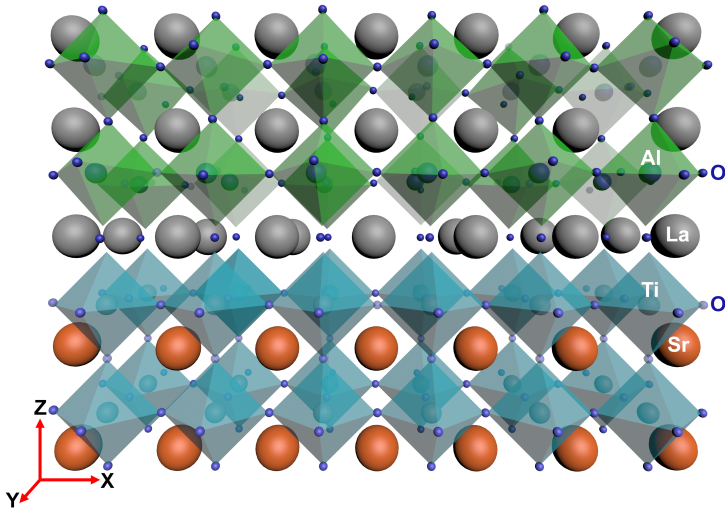
Figure 1.1: The *n-type* LAO/STO interface. The 2DEG is created between the polar layer of $La^{3+}O^{2-}$ and the charge-neutral layer of TiO_2.

Since the discovery of the 2DEG at the LAO/STO interface the study of the phenomena of transport and magnetism in oxide interfaces has aroused enormous interest. In 2010, Perna *et al.* [23] reported a metallic interface between $LaGaO_3$ deposited on top of STO substrate. They observed similar values of electrical

conduction as in LAO/STO, as well as a superconducting transition at very low temperature.

More attempts to achieve conductive interface have been made using La-based compounds, such as $LaVO_3$ [24], where a thickness-dependent metal-insulator transition was also reported. J. Biscaras *et al.* [25] observed metallic behavior and a superconducting transition at low temperature (≈ 300 mK) at the interface of $LaTiO_3$/STO . In another example, Huang *et al.* [26] observed a 2DEG in $(La_{0.3}Sr_{0.7})(Al_{0.65}Ta_{0.35})O_3$(LSAT)/STO interface, where they were able to improve the electron mobility at low temperatures, almost 30 times higher (≈ 35.000 $cm^2V^{-1}s^{-1}$) compared to the one reported for LAO/STO.

In addition, non La-based oxides have been used to create conductive interfaces with STO. Moetakef *et al.* [27] have reported conductive interface between $GdTiO_3$ and STO, although they highlight the role of oxygen-deficient STO as potential source of the conductivity. At the $CaZrO_3$/STO non-polar (001) interface, Chen *et al.* [28] have reported electron mobility of the order of 60.000 $cm^2V^{-1}s^{-1}$, via strain-induced polarization, which is among the highest achieved for perovskite-type interfaces. Moreover, at the γ-Al_2O_3/STO interface, where no polar discontinuity is present, extremely high electron mobility has been reported (≈ 140.000 $cm^2V^{-1}s^{-1}$). [29, 30]

Furthermore, Jackson *et al.* [31, 4] have reported metallic interfaces in embedded quantum wells of STO between $GdTiO_3$ and $SmTiO_3$. Angular dependent magnetoresistance experiments demonstrated exchange-coupling induced ferromagnetism in $GdTiO_3$/ STO/$GdTiO_3$ quantum wells, and antiferromagnetism in $SmTiO_3$/ STO/$SmTiO_3$ quantum wells.

Finally, the phenomenology of the 2DEG was also extended beyond STO, to the surface of $KTaO_3$ [32] and $CaTiO_3$[14], or interfaces like $CaTiO_3$/$YTiO_3$. [13]

Over the last few years different mechanisms have been put forward to explain the metallic behavior of the LAO/STO interface. One of them, the so called "Polar Catastrophe" considers an

intrinsic electronic reconstruction to avoid the effect of a polar discontinuity at the interface. Alternative pictures to this one rely on the effect of extrinsic factors, like the presence of oxygen vacancies in STO and/or LAO; cation intermixing at the interface; or surface adsorption of polar molecules, which can undergo electrochemical reactions. These mechanisms are discussed in the next section.

1.1.1 Origin of the 2DEG

The Polar Catastrophe

One of the most widely accepted hypothesis to explain the formation of the 2DEG at the LAO/STO interface is the *Polar Catastrophe*. According to this model, the polarity of the $(LaO)^+$ and $(AlO_2)^-$ layers build up an electric field in the LaO layer, which acts as a gate field on STO (Fig. 1.2A). For a sufficiently large field (thickness of LAO), the valence bands of LAO may reach the Fermi energy forming holes at its surface. To compensate this charge, electrons are attracted to the interface forming a 2D electron gas, 2DEG, at the Ti:d_{xy} interfacial bands (Fig. 1.2B). This electronic reconstruction of the interface compensates the charged surface of LAO.

Additionally, the unit cells of STO closer to the interface undergo an (intrinsic) tetragonal distortion and compression, due to the epitaxial tension with LAO. Due to the mismatch between the octahedral rotation pattern between the STO and LAO [33, 34, 35], the $3d_{xy}$ orbital of the Ti atom may be preferentially occupied, contributing to the *n-type* conductivity. [36, 37]

First-principle calculations [38, 39, 40] have predicted that the critical thickness of LAO for the Zener breakdown to take place is ≈ 3.5 unit cells, which has been experimentally confirmed by Thiel *et al.* and later on by numerous groups. [41, 42, 43, 36, 44] However, the experimental value of the carrier density falls below the expected value of $n \approx 3.3 \times 10^{14}$ cm^{-2}.

In another experiment that supports the picture of the polar catastrophe, Warusawithana *et al.* [46] studied the role of La stoi-
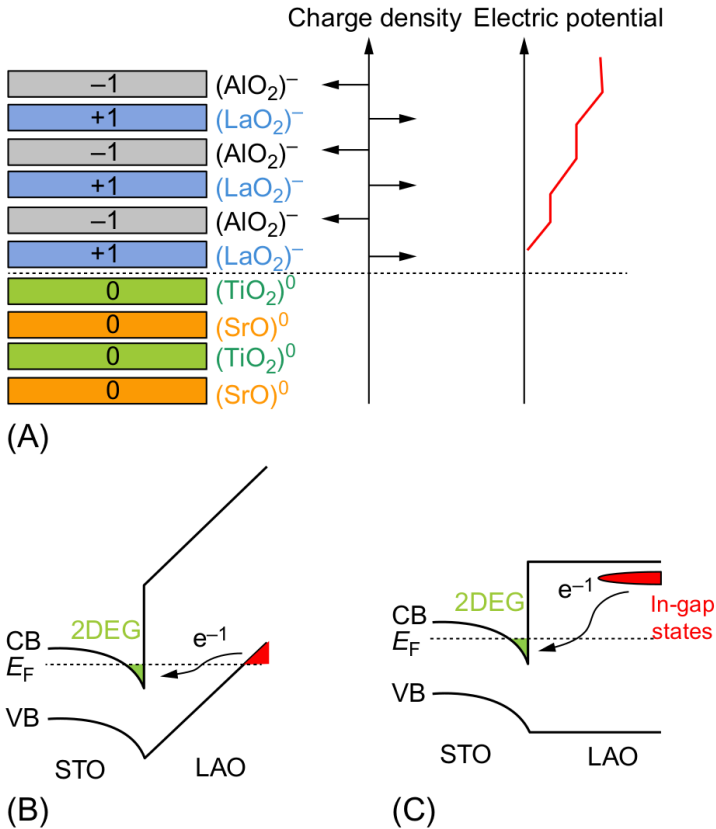
Figure 1.2:   A) Schematic representation of the polar catastrophe case: the stacking of layers of polar LAO leads to a build-up potential that is essential for the formation of the 2DEG. B) Electronic reconstruction at the LAO/STO interface: when the maximum of the valence band reaches the bottom of the STO conduction band, there is a net charge transfer to the interface. C) Schematic representation of the in-gap states introduced by V_O or other defects, that act as charge donors. Reprint from [45]

chiometry in the formation of the 2DEG. They have studied samples deposited side-by-side but with a continuous gradient of La:Al ratio, based on the position and control of the MBE guns of La and Al. From their findings, they concluded that a necessary condition for a conductive interface was that the La:Al ratio was $\leq 0.97 \pm 0.03$. Since all the samples of different stoichiometry were all deposited at the same time, they argue that mechanisms previously reported as the source of the 2DEG (V_O in STO due to low PO_2 during the deposition of substrate preparation, bombardment of STO by the energetic ions during growth and chemical intermixing between STO and LAO) can be discarded - at least for this particular study.

They report a consistent presence of B-site vacancies at the insulating interface, whereas at the conducting interfaces no vacancies were observed. Supported by first principle calculations, they attribute this behavior to different ways to compensate the polar discontinuity of the interface, depending on the stoichiometry of the sample. In the insulating samples, the cation vacancies form at the interface of La-rich samples in order to avoid the polar catastrophe, whereas in the conductive Al-rich samples, the diffusion of cations away from the interface is blocked, leading to electronic reconstruction, so that the polar catastrophe is avoided.

On the other hand, G. Herranz *et al.* [47], demonstrated the formation of metallic 2DEG at interfaces between LAO and (111), and (110) oriented STO. Furthermore, they observed similar results for interfaces between STO and amorphous LAO, STO and yttria-stabilized zirconia (YSZ). The lack of polar discontinuity at the (110) interface, and the demonstration that a perfect crystalline interface is not essential to the formation of a 2DEG, calls for an alternative (or at least additional) interpretation for the origin of this phenomena. Many authors suggested that the spontaneous formation of oxygen vacancies during growth plays a fundamental role in the appearance and properties of the 2DEG.

Oxygen vacancies

Even though there is excellent control over the deposition methods used to fabricate the thin films and interfaces, there is always the possibility that defects, such as anionic/cationic vacancies, antisite defects, impurities, etc will be incorporated in the crystal structure. Although, in general, their contribution in the physical properties of the materials is minimal, when it comes to atomically thin interfaces, combined with the presence of an electric field - such as in the case of polar interfaces, the effect of vacancies and impurities becomes very important.

One of the major drawbacks of the physical depositions systems, is the difficulty to achieve the correct oxidation state of the compound, particularly when dealing with transition metal oxides, since they can coexist in different valence states.

In order to achieve high crystalline quality, it usually necessary to reach high deposition temperatures. On the other hand, the vast majority of the LAO/STO interfaces fabricated in a PLD system are usually produced at very low oxygen pressure, which in combination with the high temperature, can lead to the creation of oxygen vacancies. It is well known that STO is greatly susceptible to creating oxygen vacancies, which determine the transport properties of the material. For each ionized V_O, two free electrons are incorporated to the $3d$ conduction band of the STO, changing it from insulating to metallic (Fig. 1.3) [45] according to the following equilibrium relations:

$$SrTiO_3 \longleftrightarrow SrTiO_{3-\delta} + \frac{\delta}{2}O_2 \uparrow$$
$$O^{2-} \longleftrightarrow V_{\ddot{O}} + 2e^-$$
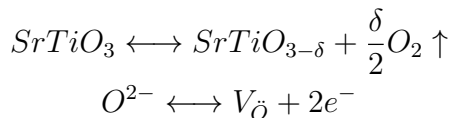
Post-deposition annealing at high oxygen pressure, may result to insufficient recovery of the oxygen stoichiometry.

In an effort to understand the contribution of the oxygen vacancies in STO on the origin and properties of the 2DEG at the
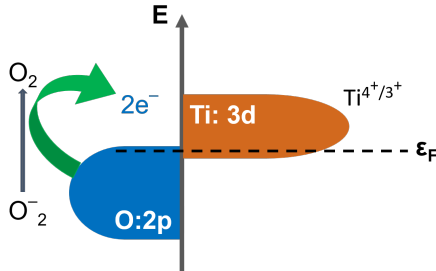
Figure 1.3: Schematic illustration of the process of the ionization of an oxygen vacancy. The ionized V_O yields two free electron to the Ti:3d conduction band, creating in gap states which contribute to the electrical conductivity of STO.

LAO/STO interface, Cancellieri *et al.* [48] have reported a conductive interface for 2-3 unit cells of LAO (less than the critical thickness) when deposited at low oxygen pressures. The carrier concentration measured by Hall effect was of the order of $\approx 10^{17}$ cm^{-2}. Post-deposition annealing of the sample at oxygen-rich atmosphere, completely suppressed this behavior, which confirms the V_O as responsible for the metallic conduction.

In a different approach, Yu and Zunger [49] proposed a mechanism, based on first principles calculations, that could explain the appearance of conductivity at the LAO/STO interface. According to their proposal, the built-in polar field that resides inside the LAO, produces a linear decrease in the formation energy of superficial V_O as the thickness of the LAO increases. After the critical thickness of ≈ 4 unit cells is surpassed, the formation energy of the superficial V_O becomes negative, meaning the spontaneous formation of the defects, even at ideal growth conditions. In return, the free electrons travel from the surface to the interface, where they eventually cancel out the built-in polar field that created them in the first place. In addition, they claim that the density of the formed 2DEG is controlled by antisite defects (where the Al_{Ti} defects are the more favorable energetically), which act as acceptors in the STO side of the interface. However, their concentration decreases dramatically when the LAO thickness is larger than ≈ 4

9

u.c, which is consistent with the picture so far.

In 2011 Santander-Syro *et al.* [50] observed by angle-resolved photoemission spectroscopy (ARPES) the formation of a highly metallic 2DEG at the surface of STO crystals cleaved under vacuum. They observed that the 2DEG was confined withing 5 u.c. of the STO surface with a sheet carrier density similar to the observed in LAO/STO interfaces. Furthermore, they studied STO crystals with different bulk doping (from non-doped to highly doped) and concluded that the observed 2DEG was decoupled from the bulk electrons in all cases, suggesting that the principal mechanism behind the 2DEG formation was the formation of oxygen vacancies at the surface.

Another interesting work about the formation of a confined 2DEG on the surface of STO was reported by Bruno *et al.*. [51] In this work, low energy Ar^+ ion bombardment created a high concentration ($\approx 6\%$) of V_O, the presence of whom was confirmed by cathodoluminescence measurements, creating a 2DEG of carrier density $n = 2.4 \times 10^{17}$ cm^{-2}. The sample was metallic with resistance values similar to the ones reported for LAO/STO interfaces, although the confinement zone of the 2DEG was calculated to be of the order of 200-300 nm, one order of magnitude larger, compared to the LAO/STO interface. They also report the appearance of a negative magnetoresistance due to spin-orbit interactions and a change of sign in MR at lower temperatures, due to enhanced scattering at the disordered region of the V_O, highlighting the role of the V_O in the interpretation of magnetotransport phenomena.

In the following years, similar results were reported for the (111) bare surface of the STO by Walker *et al.*. [52] Moreover, the formation of a 2DEG at the bare surface of a film was reported for two different materials than STO: King *et al.* [32] observed a confined 2DEG at the surface of a $KTaO_3$ (KTO) thin film and Muff *et al.* [14] at the surface of a $CaTiO_3$ thin film when cleaved under vacuum. In all cases, the density of carriers of the 2DEG can be tuned via UV radiation and exposure to oxygen, signaling towards V_O as a possible source of the conductive states.

Finally, the work by G. Herranz *et al.* [47] discussed above, showing that a non-polar interface between amorphous oxides can support a 2DEG demonstrates the main role played by oxygen vacancies in this phenomenology.

Surface Adsorption

Another mechanism proposed to explain interfacial conductivity is based on the adsorption of polar molecules on surface of the films. Zhang *et al.* [53] studied the effect of water adsorption on the conductivity of the interface between STO and different oxides, including polar and non-polar band and Mott insulators. They concluded that surface oxygen vacancies interacting with water can modulate the conductivity at the interface. [53]

Bristowe *et al.* [55] have proposed surface redox reactions as the origin of the 2DEG at the LAO/STO interface, where surface O^{2-} anions close to an oxygen vacancy transform to molecular O_2, releasing 2 electrons to the interface conduction bands. This process is similar to surface protonation, where H atoms from adsorbed water attach to the oxygen atoms of the surface, promoting the dissociation of water:

$$H_2O \rightarrow \tfrac{1}{2}O_2 + 2e^- + 2H^+$$
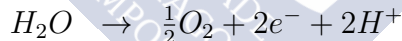
and donating two electrons to the interface.

Later on, Brown *et al.* [54] were able to change up to 4 orders of magnitude the conductivity of the LAO/STO interface by liquid immersion and light exposure. According to their proposal, when the heterostructure is immersed in various Lewis basic solvents (acetaldehyde, ethanol, nitromethane, acetonitrile, dimethylformamide, water or formamide) the hydroxylated LAO gets deprotonated which leads to an insulating LAO/STO interface. Subsequent exposure of the heterostructure to light reprotonates the LAO surface though a photocatalytic oxidation of surface adsorbed water that restores the conduction at the LAO/STO interface (Fig 1.4).
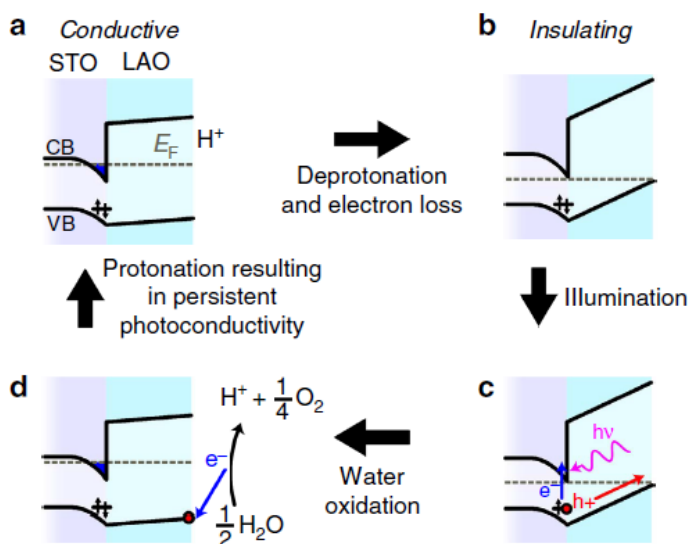
Figure 1.4: **Surface protonation/deprotonation** a) Initially, the conduction band (CB) and valence band (VB) of the LAO/STO interface bend to create an occupied conductive state at the interface. b) Solvent immersion deprotonates the surface through an acid-base reaction, removing the source of electrostatic attraction that holds the electron at the interface. Thus, an electron leaves the system either through the electrodes or through exchange with the solvent at the leads. With the interface state vacant, the system is insulating. c) Ultraviolet light creates electron-hole pairs at the oxygen vacancy, which are separated by the polar LAO potential. Specifically, the hole "bubbles up" the VB potential in the LAO and segregates to the surface. d) The surface hole oxidizes the adsorbed water, thereby generating a proton. This proton can then interact with Lewis basic sites of the LAO. Reprint from [54]

Cation Intermixing

Another mechanism proposed to explain the conductivity of the LAO/STO interface considers the effect of cation intermixing at the interface. This could be the result of either the polar field of the interface, inducing an ionic reconstruction, or an effect of the kinetic growth of the heterostructures during the physical deposition processes, by PLD or sputtering.

In general, the majority of the models used to predict and explain the conductivity of the LAO/STO interface assume an abrupt interface. However, this seems rarely the case. Qiao *et al.* [56] have performed an extensive study of the composition of the interface, as well as the adjacent regions, by means of Rutherford backscattering spectroscopy (RBS) and secondary-ion-mass spectroscopy (SIMS).

They have studied different samples with varying stoichiometry in La:Al ratio (0.9, 1.0 and 1.1) and have observed a deep diffusion of La into the STO substrate, as well as Sr diffusion into the LAO films, for all three different compositions. They argue that not only this intermixing is thermodynamically favored in order to compensate interfacial dipoles due to the polar nature of the interface, but also due to the energetic nature of the ions of the ablation plume that promotes cation displacement in the substrate, and additionally the possible creation of V_{Sr} during the deposition process of the LAO film (since Sr^{2+} and La^{3+} have similar ionic radii).

Nakagawa *et al.* [57] studied both types of LAO/STO interfaces (*n-type* and *p-type*) and concluded that cation intermixing at the interface was induced as a compensation mechanism against the polar discontinuity (see Fig. 1.5), where the *p-type* interface exhibits less interdiffusion. Furthermore, they reported the creation of interfacial oxygen vacancies as an additional means of compensation. Surprisingly they reported that at the *p-type* interface the concentration of oxygen vacancies was higher than the one at the *n-type* interface, even though the *p-type* was insulating, while the *n-type* interface conductive.

In another case, cation intermixing at the interface can result
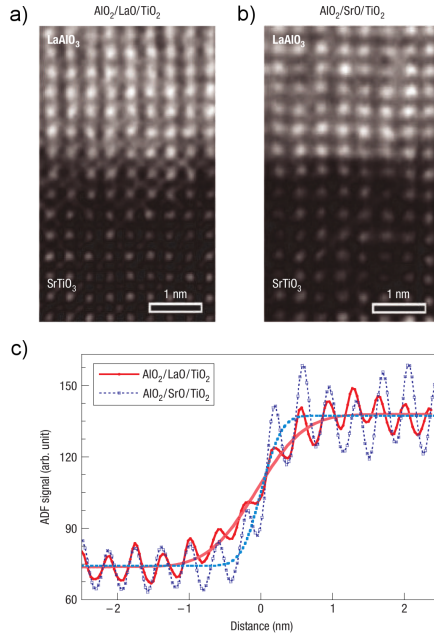
Figure 1.5: ADF-STEM Images of the LAO/STO interface structure. a) LAO grown on top of TiO_2 terminated STO. b) LAO grown on top of SrO terminated STO. c) Averaged line profiles across the interfaces of **a** and **b**. The lines correspond to the fit of an error-function curve to extract the average interface width. The extracted interface roughness is $\sigma = 1.90 \pm 0.11$ u.c. for the $AlO_2/LaO/TiO_2$ interface and $\sigma = 0.77 \pm 0.13$ u.c. for the $AlO_2/SrO/TiO_2$ interface. Reprint from [57]

into "doped" STO, where the La^{3+} substitutes the Sr^{2+} ions. [58] $La_xSr_{1-x}TiO_3$ has been known to be metallic for more than 5% doping, [59] so it is plausible that this particular intermixing could be contributing to the formation of the conductive interface. Moreover, the cation intermixing at the interface, also produces a tetragonal distortion of the unit cells around the interface that favors the high mobility of the electrons.

Electrostatic Doping

Another way to induce the formation of a 2DEG is through the application of an external electric field (see Fig. 1.6). Implementing oxide heterostructures in a field-effect transistor (FET) configuration, has been demonstrated to yield similar results as the STO-based oxide interfaces in regards of carrier density, high electron mobility and even superconducting transitions.

In 2006 Thiel *et al.* [41] demonstrated the formation of a quasi-2DEG at the LAO/STO interface, induced by a gate voltage. They confirmed that 4 unit cells of LAO is the critical thickness for conductive interface, while demonstrating that for an insulating (3 u.c. LAO) interface the applied gate field was able to provoke a metal-insulator transition with changes in conductance up to 7 orders of magnitude. For the already conductive interfaces, they were able to modulate the conductance of the interface but without reaching a metal-insulator transition.
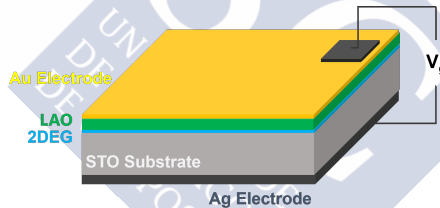
Figure 1.6: Schematic illustration of the creation of a 2DEG at the LAO/STO interface though the application of an external electric field.

In a simultaneous work, Ueno *et al.* [60] reported the formation of a 2DEG at the interface between STO and polyethetylene (a polymer electrolyte) with carrier density $n_{2D} > 10^{14}$ cm^{-2} in FET configuration. They found a superconducting transition at T$_C$ = 0.28K while demonstrating the ability to modulate the 2DEG confinement as a response to the gate voltage applied.

Another example of reversible metal-insulator and superconducting transition in a 2DEG was reported by Nakamura *et al.* [61] in a FET configuration of STO/parylene interface. More ex-

amples were later on reported on LAO/STO interfaces and the ability to modulate the carrier density and the confinement of the induced 2DEG and control the insulator to superconductor transitions. [62, 63, 64]

Nevertheless, extreme caution must be had when using high electric fields or field effect devices based on ionic liquids. Jeong *et al.* [65] have reported the creation of V_O in a VO_2 electrolyte-gated system, where they have used ionic liquid as the gate material. They have reported the manipulation of the metal-insulator transition (MIT) temperature for VO_2 thin films, depending on the gate voltage. Their findings reveal that the mechanism behind the conductive and insulating states was the creation and annihilation of V_O in the thin film, due to the migration of oxygen ions towards the ionic liquid, and not due to electrostatic doping.

1.1.2   Thermoelectricity and the 2DEG in STO

A very important observance is that the 2DEG has demonstrated the possibility of a large modulation of its thermoelectric efficiency by a gate voltage. Ohta *et al.* [66] reported an unusually large increase of the Seebeck coefficient of a 2DEG formed at the STO surface capped by nanoporous calcium aluminate (CAN) which served as a gate insulator. Even though they observed a monotonically increased carrier density for increasing gate voltage, they reported a 5-fold increase of the Seebeck coefficient when the 2DEG is confined below a critical thickness.

Generally, the Seebeck coefficient is decreased with increasing carrier density. However in this case, while the carrier density increases, the thickness of the conductive sheet becomes extremely thin due to the fact that the residual electrons in a thermoelectric material are strongly confined by the electric field, leading to an ultimate modification of the density of states (DOS). The increase in the Seebeck coefficient occurs after the critical thickness for DOS modification. [67, 68]

Using the formation of a 2DEG as a means to improve the ther-

moelectric efficiency has also been studied at interfaces. Pallecchi *et al.* [69] have reported a very large phonon-drag contribution to the thermopower of LAO/STO interface, which results into a huge increase of the Seebeck coefficient, reaching values of $\approx mV/K$ at very low temperatures. Since phonon-drag is hard to observe in bulk STO, they attribute this effect to the two-dimensional confinement and localization of the charge carriers to the interface.
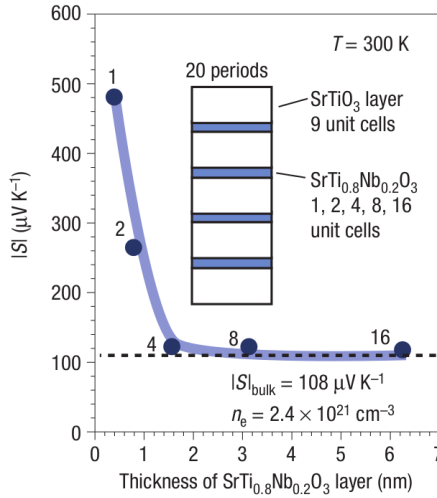
Figure 1.7: Seebeck coefficient at room temperature, as a function of the $SrTi_{0.8}Nb_{0.2}O_3$ layer thickness. An almost 5-fold increase of the Seebeck coefficient is observed for $SrTi_{0.8}Nb_{0.2}O_3$ layer thickness less than 1.56 nm (four unit cells of STO). Reprint from [7]

In addition, Ohta *et al.*, [7, 8] have proposed a similar concept for the fabrication of highly efficient thermoelectric materials. They proposed the fabrication of STO superlattices, where electron-doped ($SrTi_{0.8}Nb_{0.2}O_3$) layers are embedded in insulating STO films (see Fig. 1.7). They observed a dramatic increase in the Seebeck coefficient, when the thickness of the conductive layers was less than 4 unit cells. The value of the Seebeck coefficient for 1 unit cell thickness reached 480 $\mu V/K$, which is more than 4 times larger than the one of the bulk $SrTi_{0.8}Nb_{0.2}O_3$.

These improvements in thermoelectric efficiency, opens new paths in the search for novel ways to obtain efficient, environmentally-friendly thermoelectric materials, taking advantage of the reduced dimensionality and the customization of the component materials, tailoring their properties during the fabrication process.

1.2 Derivation of the general equations for the thermoelectric parameters

The following sections discuss the basic derivation of the general equations that describe the thermoelectric parameters, based on the Boltzmann's transport equation. The following theoretical description has been extracted mainly from J.M. Ziman's *Principles of the Theory of Solids* [70] and *Electrons and phonons: the theory of transport phenomena in solids.* [71]

1.3 The phenomenological transport coefficients

For en electronic system under small perturbations, the electric current density $\mathbf{J}$ and thermal flux density $\mathbf{Q}$, which tries to restore the equilibrium of the system, can be described as linear functions of the gradients of the electric potential $\vec{E} = \partial \vec{V}/\partial x = \nabla \vec{V}$ ($\mathbf{E}$) and the temperature gradient $\nabla \mathbf{T}$: [70, 71]

$$\mathbf{J} = L_{EE}\mathbf{E} + L_{ET}\nabla T$$
$$\mathbf{Q} = L_{TE}\mathbf{E} + L_{TT}\nabla T \qquad (1.1)$$

In an isotropic system we can treat these coefficients as scalar products, rather than tensors. From these relations, we can obtain microscopic expressions for the physical quantities that we measure on our experimental setup, such as the electrical and thermal conductivity, the Seebeck coefficient and so on. In the absence of a

temperature gradient ($\nabla T = 0$) and under the influence of a constant electric field $\mathbf{E}$, it is easy to see from Eq. 1.1 that the electrical conductivity σ equals the coefficient

$$L_{EE} = \sigma \tag{1.2}$$

In the opposite case, where the sample is under a temperature gradient ∇T and with $\mathbf{E} = 0$, we can find the expression for the thermal conductivity, κ, $\mathbf{Q} = -\kappa \nabla T$. Putting $\mathbf{J} = 0$ in the Eq. 1.1 yields

$$\mathbf{E} = -\frac{L_{ET}}{L_{EE}}\nabla T \tag{1.3}$$

Substituting the expression for $\mathbf{E}$ in the second part of Eq. 1.1, we get

$$\mathbf{Q} = L_{TT}\nabla T - \frac{L_{TE} \cdot L_{ET}}{L_{EE}}\nabla T \tag{1.4}$$

which yields the expression for the electronic contribution to the thermal conductivity:

$$\kappa_e = -\left(L_{TT} - \frac{L_{TE} \cdot L_{ET}}{L_{EE}}\right) \tag{1.5}$$

Taking a close look at the above expression for the thermal conductivity we can conclude that an electric field is built up in order to oppose the flow of electric current due to the heat flux inside the sample. This way, the built-up electric field reduces the thermal current in the sample.

The appearance of this electric field as a result of the thermal gradient in the sample is a well known phenomenon and can be measured experimentally. From Eq. 1.3 we see that the field is described as

$$\mathbf{E} = S\nabla T \tag{1.6}$$

where S is called *thermopower* or *Seebeck coefficient* of the material and is defined as

$$S = -\frac{L_{ET}}{L_{EE}} \tag{1.7}$$

In similar fashion we can see that in the absence of a temperature gradient $\nabla T = 0$, a thermal current $\mathbf{Q}$ appears due to the presence of the electric field $\mathbf{E}$, which is no other than the *Peltier* effect. From this we can define as the *Peltier coefficient*

$$\Pi = \frac{L_{TE}}{L_{EE}} \tag{1.8}$$

which is the conjugate of the *Seebeck coefficient*. Since the *Seebeck* and *Peltier* coefficients are linked by the expression $\Pi = ST$, we can rewrite the Eq. 1.1 as

$$\begin{aligned}
\mathbf{J} &= \sigma \mathbf{E} - S\sigma \nabla T \\
\mathbf{Q} &= S\sigma T \mathbf{E} - \kappa^{'} \nabla T
\end{aligned} \tag{1.9}$$

where $\kappa^{'} = \kappa + \sigma T S^2$, the lattice and electronic contributions to the thermal conductivity, as will be discussed latter.

Now that we have reached simple relations for the electrical and thermal current densities, we can proceed and calculate the macroscopic transport coefficients that describe the behavior of the materials, such as the *Seebeck coefficient* and *thermal conductivity*. For this purpose, we are going to consider that the fields and the current flow along the z direction, in an isotropic conductive material with cubic symmetry and simple parabolic band for the conduction of the carriers. Under these conditions we can rewrite the transport coefficients more explicitly in terms of the Boltzmann distribution function: [70, 71]

$$L_{EE} = -\frac{2q^2}{3m^*} \int\limits_{E=0}^{\infty} \frac{\partial f_0}{\partial E} g(E) E \tau dE \tag{1.10}$$

$$L_{ET} = -\frac{2q}{3m^*T} \int\limits_{E=0}^{\infty} \frac{\partial f_0}{\partial E} g(E) E (E - \zeta) \tau dE \tag{1.11}$$

$$L_{TE} = -\frac{2q}{3m^*} \int\limits_{E=0}^{\infty} \frac{\partial f_0}{\partial E} g(E) E (E - \zeta) \tau dE = T L_{ET} \qquad (1.12)$$

$$L_{TT} = -\frac{2}{3m^*T} \int\limits_{E=0}^{\infty} \frac{\partial f_0}{\partial E} g(E) E (E - \zeta)^2 \tau dE \qquad (1.13)$$

where q and m^* is the charge and the effective mass of the electron, respectively, f_0 is the equilibrium distribution function, $g(E)$ describes the density of states of the system, τ is the scattering mean free time, ζ is the chemical potential, and E is the electron's energy. These equations consider the variation of the distribution function from the equilibrium f_0, highlighting the non-equilibrium nature of the transport phenomena.

1.3.1 The Seebeck coefficient

Using the definition of the transport coefficients, we can write the general equation for the Seebeck coefficient as:

$$S = \frac{L_{ET}}{L_{EE}} = -\frac{1}{qT} \frac{\int\limits_{E=0}^{\infty} \frac{\partial f_0}{\partial E} g(E) E (E - \zeta) \tau dE}{\int\limits_{E=0}^{\infty} \frac{\partial f_0}{\partial E} g(E) E \tau dE}$$

$$S = -\frac{1}{qT} \left(\zeta - \frac{\int\limits_{E=0}^{\infty} \frac{\partial f_0}{\partial E} g(E) E^2 \tau dE}{\int\limits_{E=0}^{\infty} \frac{\partial f_0}{\partial E} g(E) E \tau dE} \right) \qquad (1.14)$$

The integrals in the above equation can be expressed generally as:

21

$$K_s = -\frac{2T}{2m^*} \int\limits_0^\infty g(E) \tau E^{s+1} \frac{\partial f_0(E)}{\partial E} dE$$

$$= -\frac{8\pi}{3} \left(\frac{2}{h^2}\right)^{\frac{3}{2}} (m^*)^{\frac{1}{2}} T\tau_0 \int\limits_0^\infty E^{s+r+\frac{3}{2}} \frac{\partial f_0(E)}{\partial E} dE \tag{1.15}$$

where we have taken into account that the scattering mean free time depends on the energy as $\tau = \tau_0 E^r$, and the density of states is given by the expression $g(E) = \frac{(2m)^{3/2}}{2\pi^2\hbar^3} E^{1/2}$. Integrating by parts, we get:

$$\int\limits_0^\infty E^{s+r+3/2} \frac{\partial f_0}{\partial E} dE = -\left(s + r + \frac{3}{2}\right) \int\limits_0^\infty E^{s+r+1/2} f_0(E) dE \tag{1.16}$$

This way, the transport integrals K_s take the form:

$$K_s = \frac{8\pi}{3} \left(\frac{2}{h^2}\right)^{\frac{3}{2}} (m^*)^{\frac{1}{2}} T\tau_0 \left(s + r + \frac{3}{2}\right) (k_B T)^{s+r+3/2} F_{s+r+1/2} \tag{1.17}$$

where

$$F_n(\eta) = \int\limits_0^\infty f_0(\xi, \eta) \xi^n d\xi \tag{1.18}$$

where we can make use of the reduced energy $\xi = E/k_B T$. The numerical values of the Fermi-Dirac integrals F_n can be obtained for various values of the reduced Fermi energy $\eta = \zeta/k_B T$.

The expression for the Seebeck coefficient, in terms of the K_s integral would be:

$$S = -\frac{k_B}{q} \left(\eta - \frac{K_1}{K_0}\right) \tag{1.19}$$

and more explicitly

$$S = -\frac{k_B}{q}\left(\eta - \frac{\left(r + \frac{5}{2}\right)F_{r+\frac{3}{2}}(\eta)}{\left(r + \frac{3}{2}\right)F_{r+\frac{1}{2}}(\eta)}\right) \qquad (1.20)$$

Solving this equation requires the use of numerical methods. However, if the reduced Fermi energy, η, is either much greater or much less than zero, there is the possibility to use simple approximations to the Fermi distribution function. We will analyze the expressions of S in the limits which are relevant for the results presented in this thesis.

Seebeck Coefficient for Metals and Degenerate Semiconductors

In this case we are on the limit of $\eta = \zeta/k_B T \gg 0$, the Fermi level is well above the edge of the conduction band. The Fermi-Dirac integrals can be rewritten in the form of a converging series

$$
\begin{aligned}
F_n(\eta) &= \int_0^\infty f_0 \xi^n d\xi = -\frac{1}{n+1}\int_0^\infty \frac{\partial f_0}{\partial \xi}\xi^{n+1}d\xi \\
&= -\frac{1}{n+1}\int_0^\infty \frac{\partial f_0}{\partial \xi}\left(\eta^{n+1} + \sum_{m=1}^\infty \frac{d^m(\xi^{n+1})}{d\xi^m}\big|_{\xi=\eta}\frac{(\xi-\eta)^m}{m!}\right)d\xi \\
&= \frac{\eta^{n+1}}{n+1} + n\eta^{n-1}\frac{\pi^2}{6} + \cdots
\end{aligned}
$$

$$\qquad (1.21)$$

To obtain a non-zero value for the Seebeck coefficient we need to use the first two terms of the series to describe the Fermi-Dirac integrals in Eq. 1.20 and take $q = -e$ for the charge carriers. Therefore, we end up with the expression:

$$S = -\frac{\pi^2 k_B}{3e}\frac{k_B T}{\zeta}\left(\frac{3}{2} + r\right) \qquad (1.22)$$

23

From an experimental point of view, we can use the experimentally measured magnitudes available and obtain information about the more "internal" properties of a system, such as its degree of degeneracy of the conduction bands, for example. As it is going to be discussed later on the *Results and Discussion* section, it is possible to extract meaningful information about the band degeneracy of doped $SrTiO_3$ system from the S(T) measurements.

Heikes Formula: The High Temperature Limit

Another significant limit to consider for the Seebeck coefficient is at very high temperatures. Heikes [72] predicted that the thermopower at higher temperatures would be independent of the temperature and it would only depend on the entropy contributed by each carrier (see Fig. 1.8). Starting from the definition of the chemical potential ζ:

$$\zeta = -T\left(\frac{\partial \Sigma}{\partial N}\right)_{E,V} \tag{1.23}$$

where Σ is the system's entropy, N is the number of particles, E is the internal energy and V the volume. As $T \to \infty$, we can calculate the entropy of the system in terms of the degeneracy g of the high temperature state, using Boltzmann's configurational entropy equation:

$$\Sigma = k_B \ln g \tag{1.24}$$

so that

$$\zeta = -k_B T\left(\frac{\partial \ln g}{\partial N}\right)_{E,V} \tag{1.25}$$

Substituting the above term for the chemical potential in Eq. 1.19 we get:

$$S = -\frac{1}{qT}\left(\zeta - \frac{K_1}{K_0}\right) = \frac{1}{qT}\left(k_B T\frac{\partial \ln g}{\partial N} + \frac{K_1}{K_0}\right) \tag{1.26}$$

where K_0 and K_1 are the transport integrals of the Eq. 1.15. At the limit of $T \to \infty$ the second term of the above equation vanishes, so that the final relation of the Seebeck at the high temperature limit is:

$$S = \frac{k_B}{q} \frac{\partial \ln g}{\partial N} \tag{1.27}$$

Now if we consider the particles present in our system as spinless fermions, then from Pauli's rule, two particles cannot occupy the same site, which makes the degeneracy:

$$g = \frac{N_A!}{N!(N_A - N)!} \tag{1.28}$$

Using Stirling's approximation and differentiating with respect to N, we arrive at the expression of the well-known *Heikes formula*:

$$S_{T \to \infty} = \frac{k_B}{q} \ln \left(\frac{1 - \rho}{\rho} \right) \tag{1.29}$$

where $\rho = N/N_A$ is the ratio of particles to available sites.

As we saw, the Heikes formula treats the particles as spinless fermions in order to get to the final expression 1.29. However, thermopower is very susceptible to the degeneracy, so it is very important to account for the spin and orbital degeneracy as well. Koshibae *et al.* [73] proposed a modified Heikes formula, taking into account the spin and orbital degeneracy. In the proposed model, there are two kinds of sites, occupied and unoccupied. These site are denoted as (I) and (II), respectively. Therefore, the degeneracy g is going to be given by the total number of ways of arranging the two kinds of sites:

$$g = [g_{(I)}]^{2L-N} [g_{(II)}]^{N-L} \frac{L!}{(N-L)!(2L-N)!} \tag{1.30}$$

where L denotes the number of unit cells, N the number of particles and $g_{(I)}$ and $g_{(II)}$ are the degeneracies of the sites (I) and

(II) respectively. Using Stirling's approximation in the previous expression, yields the formula:

$$S = \frac{k_B}{q} \ln \left(\frac{g_{(I)}}{g_{(II)}} \frac{x}{1-x} \right) \tag{1.31}$$

where $x = (2 - N)/L$. From this expression we can see the importance of the fraction of conducting sites $x/(1-x)$, but furthermore we can appreciate the importance of the ratio of the electronic degeneracy for the ions responsible for the conduction. A large value of this ratio yields a large contribution to the Seebeck coefficient from spin and orbital entropy.
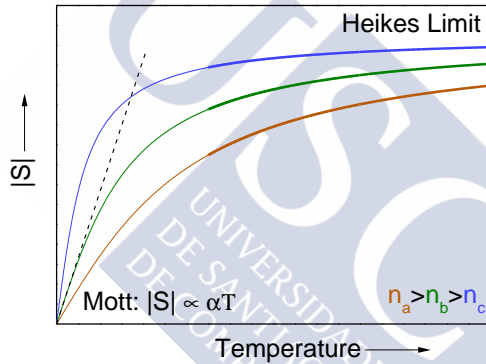
Figure 1.8: Illustration of the temperature dependence of the Seebeck coefficient for three different values of carrier concentration. As the carrier concentration increases, the value of |S| decreases. At the low temperature limit, the value of |S| increases linearly with the temperature, whereas, when the temperature reaches the Heikes high temperature limit, the value of |S| is independent of the temperature.

1.4 Thermal conductivity - Basic theory

Heat transport is a very important field of study in a world of continuous technological advances, especially regarding micro- and

nanodevices and their applications. For example, one needs materials and composites with very high thermal conductivity in order to address issues with thermal management, especially in the field of electronics, where overheating can be a very limiting factor in performance. On the other hand, new thermoelectric materials need to have a very low thermal conductivity to achieve desirable levels of efficiency.

Either way, we need to deeply understand the basics of thermal transport and use it to our advantage in both ends of the thermal conductivity range. The following theoretical description has been extracted mainly from T. M. Tritt's *Thermal conductivity: theory, properties, and applications* [74] and *High lattice thermal conductivity solids* from D.T. Morelli and G.A. Slack. [75]

In general, heat can be transported inside a solid through various different ways, such as electron diffusivity, lattice vibrations (phonons), spin waves (magnons), etc. Irrespective of the nature of the excitations responsible for the heat transport, the thermal conductivity describes the rate of energy transport in response to a heat gradient. Therefore, it must be proportional to the energy stored by the system, times the velocity at which this energy is transported along a given length. This gives rise to a kinetic equation:

$$\kappa = \frac{1}{3} \sum_{\alpha} C_{\alpha} v_{\alpha} \Lambda_{\alpha} \qquad (1.32)$$

where C, v and Λ correspond to the heat capacity, velocity and mean free path of the different α excitations. Generally Eq. 1.32 is very useful in estimating the orders of magnitude of the thermal conductivity and can provide a decent phenomenological description. However, a more developed microscopic theory is needed in order to understand the effect of the different parameters in a real system (crystal structure, defects, etc) on the thermal conductivity.

27

1.4.1 Electronic thermal conductivity

The electronic contribution to the thermal conductivity κ_e can be obtained from Eq. 1.5:

$$
\begin{aligned}
\kappa_e &= -\left(L_{TT} - \frac{L_{TE} \cdot L_{ET}}{L_{EE}} \right) = -\left(L_{TT} - \frac{T L_{ET}^2}{L_{EE}} \right) \\
&= -\left(-\frac{2}{3m^*T} \int_0^\infty g(E)\tau E(E-\zeta)^2 \frac{\partial f_0}{\partial E} \right. \\
&\quad \left. - \left[\frac{T\left(-\frac{2q}{3m^*T} \int_0^\infty \frac{\partial f_0}{\partial E} g(E) E(E-\zeta)\tau dE \right)^2}{-\frac{2q^2}{3m^*} \int_0^\infty \frac{\partial f_0}{\partial E} g(E) E\tau dE} \right] \right)
\end{aligned}
\tag{1.33}
$$

In terms of the transport integrals, previously defined, K_s (Eq. 1.15), the above expression can be summed up as:

$$
\kappa_e = \frac{1}{T^2}\left(K_2 - \frac{K_1^2}{K_0} \right)
\tag{1.34}
$$

A convenient way to express the electronic part of the thermal conductivity, is in terms of the *Lorenz number*, $L = \kappa_e/\sigma T$. From the expression 1.34 and the electrical conductivity, we can express the Lorenz number L as:

$$
L = \frac{1}{q^2 T^2}\left(\frac{K_2}{K_0} - \frac{K_1^2}{K_0^2} \right)
\tag{1.35}
$$

Examining the electronic thermal conductivity in the limit of $\zeta/k_B T \ll 0$, in the **non-degenerate approximation** yields:

$$
L = \left(\frac{k_B}{q} \right)^2 \left(r + \frac{5}{2} \right)
\tag{1.36}
$$

which demonstrates that L does not depend on the Fermi energy, as long as r in the dependence of the relaxation time on the energy, is constant.

In the case of **metal or degenerate semiconductor approximation** $(\zeta/k_B T \gg 0)$ the expression 1.35 yields

$$L = \frac{\pi^2}{3}\left(\frac{k_B}{e}\right)^2 \tag{1.37}$$

which demonstrates that the Lorenz number L should be the same for all metals and degenerate semiconductors and it should not depend on the scattering law for the charge carriers. Therefore, we can obtain a quite reliable value of the electronic thermal conductivity from the electrical conductivity, at least in the limits considered here.

1.4.2 Lattice thermal conductivity

The heat transport in insulating, or even semiconducting materials, is mostly carried out by collective crystal lattice vibrations, known as phonons. Depending on their type of oscillation (in-phase or out-of-phase), phonons are distinguished in acoustic or optical phonons. Optical phonons don't really contribute much to the thermal conduction in the solid, mainly due to the small group velocity $\vec{v}_g = \frac{\partial \omega_{\vec{q}}}{\partial q}$. Nevertheless, optical phonons may affect the heat conduction by interacting with the acoustic phonons. In order to find the general expression for the thermal conductivity, we need to setup the phonon distribution function, *i.e.* the average number of phonons with a wave vector $\vec{q}$ $(N_{\vec{q}})$. The phonon distribution function in equilibrium is given by the Bose - Einstein distribution:

$$N_{\vec{q}}^0 = \frac{1}{e^{\hbar\omega_{\vec{q}}/k_B T} - 1} \tag{1.38}$$

The different scattering processes tend to restore any phonon distribution $N_{\vec{q}}$ to its equilibrium $N_{\vec{q}}^0$, at a rate

$$\frac{N_{\vec{q}} - N_{\vec{q}}^0}{\tau_{\vec{q}}} = -\left(\vec{v_g} \cdot \nabla T\right)\frac{\partial N_{\vec{q}}^0}{\partial T} \qquad (1.39)$$

where $\vec{v_g}$ is the group velocity, and $\tau_{\vec{q}}$ is the phonon scattering relaxation time. The total heat flux of all phonon modes is the sum of the product of the average energy and group velocity of each phonon mode $\vec{q}$:

$$\vec{Q} = \sum_{\vec{q}} N_{\vec{q}} \hbar \omega_{\vec{q}} \vec{v_g} \qquad (1.40)$$

Combining Eq. 1.39 and 1.40 yields:

$$\begin{aligned}
\vec{Q} &= \sum_{\vec{q}} N_{\vec{q}} \hbar \omega_{\vec{q}} v_g^2 < \cos^2 \theta > \tau_q \frac{\partial N_{\vec{q}}^0}{\partial T} \vec{\nabla} T \\
&= -\frac{1}{3} \sum_{\vec{q}} N_{\vec{q}} \hbar \omega_{\vec{q}} v_g^2 \tau_q \frac{\partial N_{\vec{q}}^0}{\partial T} \vec{\nabla} T
\end{aligned} \qquad (1.41)$$

where θ is the angle between $\vec{v_g}$ and $\vec{\nabla} T$. We already know that the lattice thermal conductivity due to an established thermal gradient is given by $-\vec{Q}/\vec{\nabla} T$, so we end up with the expression:

$$\kappa_{ph} = \frac{1}{3} \sum_{\vec{q}} N_{\vec{q}} \hbar \omega_{\vec{q}} v_g^2 \tau_q \frac{\partial N_{\vec{q}}^0}{\partial T} \qquad (1.42)$$

Although this expression seems familiar and relatively simple, it is meaningless to try and calculate the value of κ_{ph} for a real solid. In order to be able to calculate the lattice thermal conductivity, we need to make some approximations and then to evaluate different phonon scattering relaxation times. Starting from the approximations, according to the Debye theory, i) we will use an average velocity v that replaces v_g for all the phonon branches and ii) all phonon velocities are the same for all polarizations. After the Debye assumption, we replace the sum with an integral in the above expression (Eq 1.42) as

$$\kappa_{ph} = \frac{1}{3} \int \hbar\omega_{\vec{q}} v_g^2 \tau_q \frac{\partial N_{\vec{q}}^0}{\partial T} f(q) d\vec{q} \tag{1.43}$$

where $f(q)d\vec{q} = (3q^2/2\pi^2)dq$, and therefore $f(\omega)d\omega = (3\omega^2/2\pi^2 v^3)d\omega$. The Debye assumptions (Eq. 1.43) combined with Eq. 1.38 and 1.42 yields

$$\kappa_{ph} = \frac{1}{2\pi^2 v} \int\limits_0^{\omega_D} \hbar\omega^3 \tau_q(\omega) \frac{(\hbar\omega/k_B T^2)e^{\frac{\hbar\omega}{k_B T}}}{[e^{\frac{\hbar\omega}{k_B T}} - 1]^2} d\omega \tag{1.44}$$

where ω_D is the Debye frequency. Substituting $x = \hbar\omega/k_B T$ and defining $\theta_D = \hbar\omega/k_B$ as the Debye temperature, Eq. 1.44 becomes

$$\kappa_{ph} = \frac{k_B}{2\pi^2 v} (\frac{k_B}{\hbar})^3 T^3 \int\limits_0^{\theta_D/T} \tau_q(x) \frac{x^4 e^x}{(e^x - 1)^2} dx \tag{1.45}$$

This expression is called the *Debye approximation for the lattice thermal conductivity*.

The effect of the different parameters of the solid in the thermal conductivity is accounted by their effect on the relaxation times $\tau_i^{-1}(x)$, which are supposed to be additive:

$$\tau_q^{-1}(x) = \sum_i \tau_i^{-1}(x) \tag{1.46}$$

In the following, we will discuss the contribution of some of the most common scattering processes to the relaxation time. We will only consider the scattering processes in which there is a change in the wave vector of the phonons, (*Umklapp* or U-processes).

Phonon - phonon relaxation time

The Debye temperature, θ_D, defines the characteristic energy scale of the crystal lattice, and determines the intrinsic mechanisms of phonon dispersion in the material. At temperatures not too far away from θ_D, anharmonic phonon-phonon *Umklapp* scattering is

the main mechanism responsible for $\kappa(T)$, which can be approximated by [75]:

$$\kappa = \epsilon \frac{\overline{M}\delta\theta_D^3}{\gamma^2 T n^{3/2}} \qquad (1.47)$$

where $\overline{M}$ is the average molar mass per atom in a crystal with n atoms per formula unit (Z molecules per unit cell), $\delta=(V/nZ)^{1/3}$ is the cubic root of the volume per atom, γ is the Grüneisen factor and ϵ is a constant.

Taking into account that multiple phonon frequencies contribute to the thermal conductivity, the relaxation time to be included in equation 1.46 and 1.45 would be [76]:

$$\tau_U^{-1} \approx \frac{\hbar\gamma^2}{\overline{M}v^2\theta_D}\omega^2 T e^{-\frac{\theta_D}{3T}} \qquad (1.48)$$

At sufficiently high temperatures $\kappa_{ph} \propto 1/T$ in most crystalline materials, reflecting the dominance of phonon-phonon *Umklapp* scattering.

Phonon scattering by point defects.

When the linear dimensions of the defects are much smaller than the phonon wavelength, then the scattering rate can be approximated by [77]:

$$\tau_{PD}^{-1} = \frac{V}{4\pi v^3}\omega^4 \sum_i f_i(\frac{\overline{M} - m_i}{\overline{M}})^2 \qquad (1.49)$$

where V is the average volume per atom, v is the average sound velocity, m_i is the mass of a defect, f_i is the fraction of defects, and $\overline{M}$ is the average mass per atom. This approximation is valid for point-defect scattering, like that produced by vacancies, atomic substitution (interdiffusion) and isotope scattering.

Phonon scattering by crystal and domain boundaries.

The phonon - boundary scattering rate is independent of the phonon frequency and temperature, and can be approximated by the expression:

$$\tau_{PB}^{-1} = \frac{v}{d} \tag{1.50}$$

where v is the phonon velocity and d is related to the size of grains in polycrystalline materials, or the diameter of an effective cross-sectional area in the case of a single crystal. The effect of domain boundary scattering over $\kappa(\text{T})$ can become very important at low temperature, as the mean free path of the long-wavelength acoustic phonons increases.

In Figure 1.9 we summarize the contribution of the scattering mechanisms to $\kappa(\text{T})$, in the different temperature ranges.
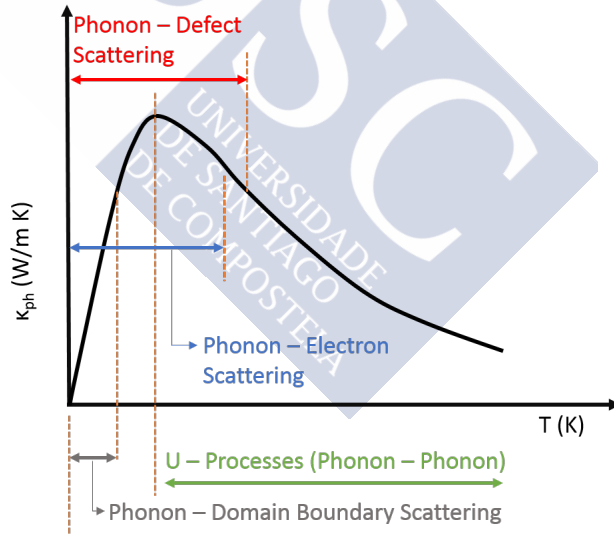

Figure 1.9: *Illustration of the temperature dependent phonon thermal conductivity for a crystalline solid, with the different scattering mechanisms associated with each temperature segment.*

For the particular case of the thin films studied in this thesis, we will see that the effect of epitaxial strain, film thickness, phonon

instabilities (ferroelectric distortions), vacancies, etc. play a very important role over their thermal conductivity. As we will discuss in the experimental chapters, the effect of these parameters can be accounted for within the framework of the Debye approximation to $\kappa(T)$ in the τ approximation.

1.5 The perovskite lattice: crystal symmetry & octahedral rotations

In this work, we are going to focus on the oxide-family of perovskites, of chemical formula ABO_3; A and B are cations, normally with valence 2^+, 3^+ or 4^+. A common way or representing this structure is through a network of corner-sharing BO_6 octahedra, where the A-cation is in the center of a cube defined by 8 corner sharing octahedral units. In the undistorted cubic structure the A-cation is surrounded by 12 oxygen ions, the B-cation is octahedrically coordinated by 6 oxygens, and the oxide ions are coordinated by two B-cations and 4 A-cations. An example of an ideal cubic perovskite structure is the $SrTiO_3$ (see Fig. 1.10).
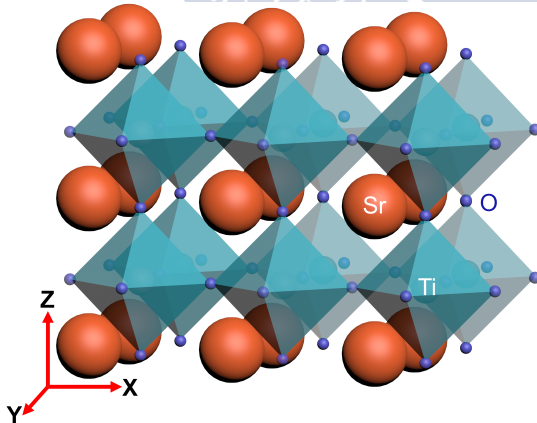

Figure 1.10: Illustration of the undistorted STO perovskite structure.

On the other hand, most of the perovskite compounds do not

present this cubic structure. Substituting the A and B cations introduces some stress into the structure, which changes its bond-distances accordingly, in order to keep the maximum packing density. The Goldschmidt tolerance factor represents a geometric measure of closed-sphere packing, relating the A-O and B-O bond lengths to the crystal stability: [78]

$$ t = \frac{R_A + R_O}{\sqrt{2}(R_B + R_O)} \tag{1.51} $$

where R_A, R_B and R_O are the ionic radii of the A and B cations and oxygen, respectively. [79] The perovskite structure is stable in the interval $0.78 < t < 1.0$. [80] Ionic replacement decreases t from the cubic value ($t = 1$) through different BO_6 octahedral rotations and deformation, *i.e.* variations in $B - O$ and $A - O$ bond lengths, thus lowering the unit cell symmetry. Moreover, due to the coupling between the structural distortions and the transport and magnetic (through spin-orbit coupling) properties, these octahedral rotations may determine, to a great extent, the physical properties of these materials.

This is particularly important in the case of $3d$ oxoperovskites, in which their narrow electronic bands are very susceptible to subtle lattice distortions. This strong coupling between the lattice and electronic degrees of freedom is actually the origin of their rich variety of physical properties, including metal-insulator transitions, ferroelectricity, superconductivity, magnetoresistence, etc. [11, 81, 82, 83, 84]

In the case of thin films, cooperative octahedral rotations is an important type of structural modification that accommodates the tensile/compressive strain on the A-O and B-O bonds produced by epitaxial growth. [85, 86, 87, 88]

Therefore, determining accurately the effect of epitaxial strain and/or the different type of vacancies present in the films studied in this thesis, over the TiO_6 octahedral rotations, is crucial to understand their properties.

1.5.1   Description of the cooperative rotations of BO_6 octahedra in a perovskite

Glazer introduced a notation in order to describe the different octahedral rotations that can be present in a perovskite. [89, 90] In the perovskite structure, when an octahedron is tilted in any way, it provokes the tilting of its neighboring octahedra (cooperative BO_6 octahedral rotation). When present, this cooperative rotation is the most important component in establishing the overall space-group symmetry of the perovskite. In the concept of a generalized classification of the possible ways of tilting, all the available tilts can be described on the basis of three pseudocubic axes, and the magnitude of the tilts are indicated by a set of three letters which refer to rotation about the axes [100], [010] and [001] respectively (Fig. 1.11).
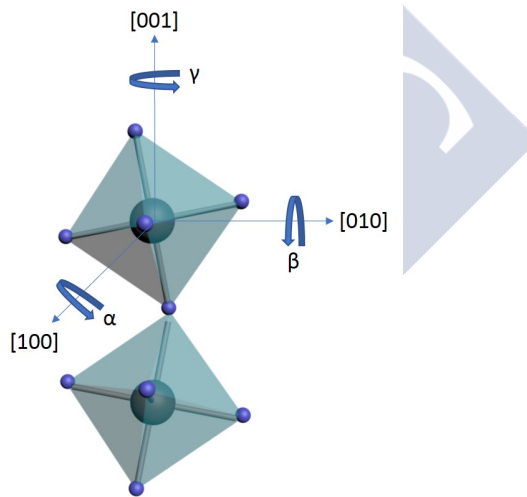
Figure 1.11: Schematic illustration of the tilt angles of two corner-sharing octahedra around the three pseudocubic axes, under the Glazer notation.

When the magnitude of the tilt is different along the three

spatial directions, it is denoted as *abc*. Tilts of the same magnitude are denoted by the same letter, ie. *aac* would correspond to tilts of the same magnitude about the [100] and [010] axes, and an different tilt about the [001] axis. When successive octahedra are tilted the same way along a particular axis, then they are rotating *in-phase*, and the notation would be a superscript + on the corresponding letter. *Out-of-phase* tilting will be denoted as −, and the absence of tilting will be denoted as 0 (Fig.1.12).
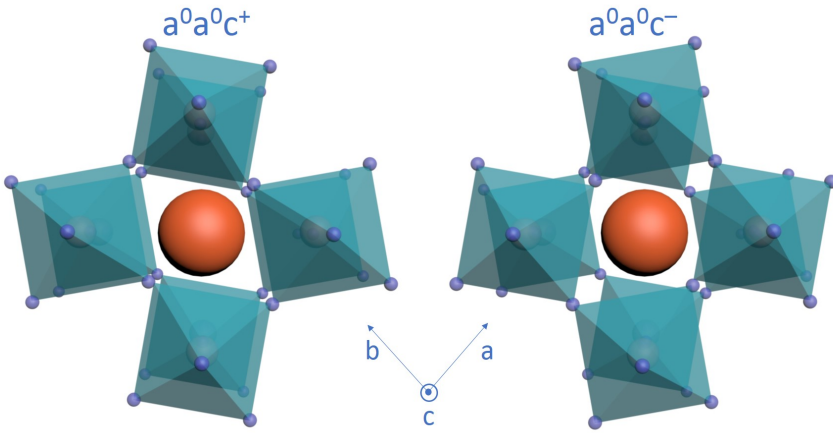

Figure 1.12: Schematic illustration of in-phase [left] and out-of-phase [right] octahedral rotations in a perovskite structure, along the c-axis (001).

In the spirit of this notation and assuming that no repeat period consists of more than two octahedra, there are 10 distinct possibilities:

$a^+b^+c^+$	$a^+b^+c^-$	$a^+b^-c^-$	$a^-b^-c^-$	3 tilts
$a^0b^+c^+$	$a^0b^+c^-$	$a^0b^-c^-$		2 tilts
$a^0b^0c^+$	$a^0b^0c^-$			1 tilt
$a^0b^0c^0$				no tilts

In these possibilities we haven't taken into account the magnitude of the tilts, something that becomes important when we want to

examine the relation between the tilts and the crystal systems. The effect of the tilting of the octahedra can be summed up in the following: *(i) Unit cell lengths, (ii) Unit cell angles* and *(iii) The appearance of distinctive Bragg reflections* The factor that is the most important for this work is the appearance of new Bragg reflections, which allow the identification of a given lattice distortion.

The tilting of the octahedra may result in the doubling of the unit cell and as a consequence extra reflections are produced which lie on the half-integral reciprocal-lattice planes. If we use as a reference the doubled unit cell of the crystal under study, the extra reflections can be indexed having some of the Miller indices (*hkl*) odd, while the main reflections have all their indices even. Luckily, the *in-phase* (+) and *out-of-phase* (-) tilts produce two distinct classes of reflections. + tilts produce at least one *even* Miller index, while − tilts result in *odd-odd-odd* reflections. More specifically:

$$
\begin{array}{llll}
\mathbf{a}^+ & \text{produce } \textit{even-odd-odd} \text{ reflections with} & k \neq l \\
\mathbf{b}^+ & \text{produce } \textit{odd-even-odd} \text{ reflections with} & h \neq l \\
\mathbf{c}^+ & \text{produce } \textit{odd-odd-even} \text{ reflections with} & h \neq k \\
\mathbf{a}^- & \text{produce } \textit{odd-odd-odd} \text{ reflections with} & k \neq l \\
\mathbf{b}^- & \text{produce } \textit{odd-odd-odd} \text{ reflections with} & h \neq l \\
\mathbf{c}^- & \text{produce } \textit{odd-odd-odd} \text{ reflections with} & h \neq k
\end{array}
\tag{1.52}
$$

There are 23 distinct tilt systems differentiated from one another depending on the magnitude and the phase of the tilting of the BO_6 octahedra (see Table 1.1). Although Glazer was the first to propose a guide for the assignation of each tilt system to a space group, later work by Woodward based on computer simulations introduced some corrections on the space group assignation of the tilt systems. [91, 92]

His corrections were made on the basis that some particular tilt systems *must* exhibit small distortions of the octahedra, in order to preserve their connectivity with each other. Furthermore, Woodward made further predictions of the space group assignation of the

tilt systems, taking into account the combined effect of cation ordering where two different $B - O$ bond distances are present which result in the deformation of the BO$_6$ octahedra.
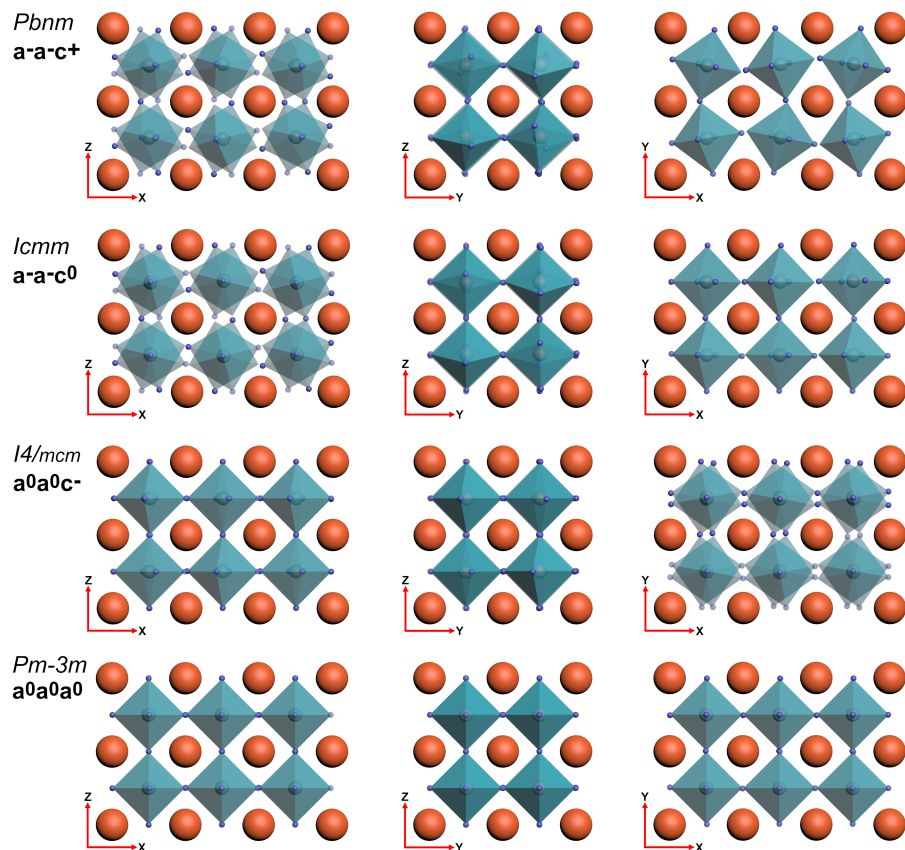

Figure 1.13: Schematic illustration of different octahedral rotation patterns, indexed by their space group symmetries.

The different tilt systems are summarized in Table 1.1 and in Fig. 1.13.

Space groups for all possible simple tilt systems			
Tilt-System Number	Tilt-System Symbol	Space Group (No ordering)	Space Group (1:1 Ordering)
Three tilt systems			
1	$a^+b^+c^+$	Immm (#71)	Pnnn (#48)
2	$a^+b^+b^+$	Immm (#71)	Pnnn (#48)
3	$a^+a^+a^+$	Im$\bar{3}$ (#204)	Pn$\bar{3}$ (#201)
4	$a^+b^+c^-$	Pmmn (#59-2)	P2/c (#13)
5	$a^+a^+c^-$	P4$_2$/nmc (#137-2)	P4$_2$/n (#86)
6	$a^+b^+b^-$	Pmmn (#59-2)	P2/c (# 13)
7	$a^+a^+a^-$	P4$_2$/nmc (#137-2)	P4$_2$/n (#86)
8	$a^+b^-c^-$	P2$_1$/m (#11-1)	P1 (#2)
9	$a^+a^-c^-$	P2$_1$/m (#11-1)	P4$\bar{1}$ (#2)
10	$a^+b^-b^-$	Pnma (#62)	P2$_1$/n (#14-2)
11	$a^+a^-a^-$	Pnma (#62)	P2$_1$/n (#14-2)
12	$a^-b^-c^-$	F$\bar{1}$ (#2)	F$\bar{1}$ (#2)
13	$a^-b^-b^-$	I2/a (#15-3)	F$\bar{1}$ (#2)
14	$a^-a^-a^-$	R$\bar{3}$c (#167-2)	R$\bar{3}$ (#148-2)
Two tilt systems			
15	$a^0b^+c^+$	Immm (#71)	Pnnn (#48)
16	$a^0b^+b^+$	I4/mmm (#149)	P4$_2$/nnm (#134)
17	$a^0b^+c^-$	Cmcm (#63)	C2/c (#15$\bar{1}$)
18	$a^0b^+b^-$	Cmcm (#63)	C2/c (#15$\bar{1}$)
19	$a^0b^-c^-$	I2/m (#12$\bar{3}$)	I$\bar{1}$ (#2)
20	$a^0b^-b^-$	Imma (#74)	I2/m (#12$\bar{3}$)
One tilt systems			
21	$a^0a^0c^+$	P4/mbm (#127)	P4/mnc (#128)
22	$a^0a^0c^-$	I4/mcm (#140)	I4/m(#87)
Zero tilt systems			
23	$a^0a^0a^0$	Pm$\bar{3}$m (#221)	Fm$\bar{3}$m (#225)

Table 1.1: List of all possible 23 simple tilt systems predicted by Glazer (No ordering) and Woodward (1:1 Ordering). In Glazer's predictions, the octahedra were rigid and did not allow for deformations, while in Woodward's predictions, the octahedral deformations were taken into account.

Chapter 2

Experimental techniques

2.1 Synthesis of the thin films

2.1.1 Pulsed laser deposition

All the samples studied in this work were prepared by Pulsed Laser Deposition (PLD). [93] This is one of the most common methods of thin film fabrication, along with Molecular Beam Epitaxy (MBE), [94] Sputtering, [95] and different chemical solution deposition methods. [96] The thin films studied in this thesis were fabricated in a PLD system by Neocera (http://neocera.com/).

Two different lasers were used to prepare the thin films studied in this thesis: a *KrF* Excimer (Coherent COMPex, $\lambda = 248$ *nm*, pulse length $\approx$20 ns) and a solid state Nd:YAG (Q-Smart, $\lambda = 266$ *nm*, pulse length $\approx$6 ns). In our system, the laser enters a 45.72 cm (18 inches) diameter vacuum chamber through a UV-grade laser window, and impacts the surface of the target at $\approx$45° (see Fig. 2.1). Each pulse of the laser rapidly evaporates the material from the target, forming an ablation plume which transfers the atomic species to a substrate, retaining its stoichiometry. [97, 98]

Most of the films studied in this thesis were deposited with a laser repetition rate of 5 Hz. In our chamber the substrate is kept $\approx$5 *cm* above the target, glued with silver paste to a holder. The

sample holder is in contact with an electric heater, which allows to rise the temperature up to 960℃. The target is set to raster circularly at a rate of $91°/min$ as well as horizontally at a rate of $47°/min$ in order to make sure that the laser ablates its whole surface. For the sake of a homogeneous deposition, the sample holder is set to a $51°/min$ rotation.
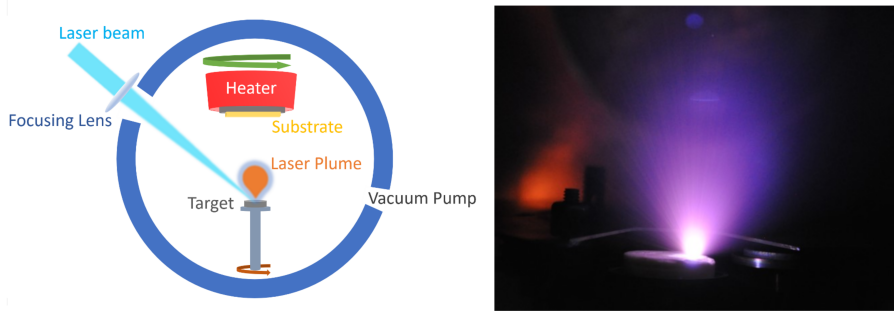

Figure 2.1: Left: Schematic illustration of a typical PLD system. Right: Photograph of the laser ablation plume during a deposition inside the PLD chamber of our system.

The pressure inside the chamber may be controlled between $\approx 10^{-8} - 5 \times 10^{-1}$ Torr during deposition. Both O_2 and N_2 can be used as background gases during deposition.

The final film thickness depends mainly on the background atmosphere of the PLD chamber, the number of pulses and the laser fluence. Ex-situ X-ray reflectivity (XRR) analysis gives the information about the thickness of the films so that the growth rate ($nm/pulse$) can be estimated for each material and growth conditions.

2.1.2   Target preparation

The target materials were synthesized by solid state reaction from commercial reactants. For the fabrication of the ceramic target of Nb:STO, nominal composition $Nb_{0.05}SrTi_{0.95}O_3$, commercial powders of $SrCO_3$ (99.995%), TiO_2 (99%) and Nb_2O_5 (99.99%) (Sigma

Aldrich) were stoichiometrically weighted for a nominal 5 % Nb doping (Nb atoms will substitute the Ti ones), mixed together, first by hand in a ceramic mortar and then in an agate mortar and introduced in a ball mill where it was left to be ground and mixed during 24 hours, at 150 rpm, with a change in the cycling direction every 10 min. After that, the powders were pressed in a hydraulic press for about 3 min at a 5 ton pressure, in order to form a dense pellet of 2.54 cm (1 inch).

Then the pellet was introduced in a tubular furnace with a flow of forming gas (5% H_2 in N_2 gas). The temperature increase was held at 3℃/min until 200℃ for 1 hour, and then increasing with the same rate up to 1200℃ where the target was sintered for 12 hours. The cooling rate was 3℃/min. After the first calcination, the pellet was introduced for another 24 hours in the ball milling. After forming a new pellet at the hydraulic press, a second step of sintering was performed in the presence of forming gas at 1300℃ for 12 hours.

The composition and absence of secondary phases was probed by X-ray powder diffraction (see Fig. 2.2), and energy-dispersive X-ray spectroscopy (EDS)(see Fig. 2.3) in a scanning electron microscope (SEM).

Both techniques show that the ceramic target is single phase after this treatment, with a composition $Nb_{0.02}SrTi_{0.98}O_3$, showing some evaporation of Nb during the thermal treatment. This Nb content was confirmed by EELS analysis on cross-section lamellae studied by electron microscopy, as will be discussed latter.

In the case of the target of $CaTiO_3$, commercial powders of $CaCO_3$ (99.99%) and TiO_2 (99%) (Sigma Aldrich) were stoichiometrically weighted and mixed. The powders were grounded and pressed as explained before. The pellet was subjected to a final thermal treatment at 1400℃ for 12 hours. Same as before, the correct composition was verified by X-ray powder (see Fig. 2.2) diffraction and EDS analysis (see Fig. 2.3).
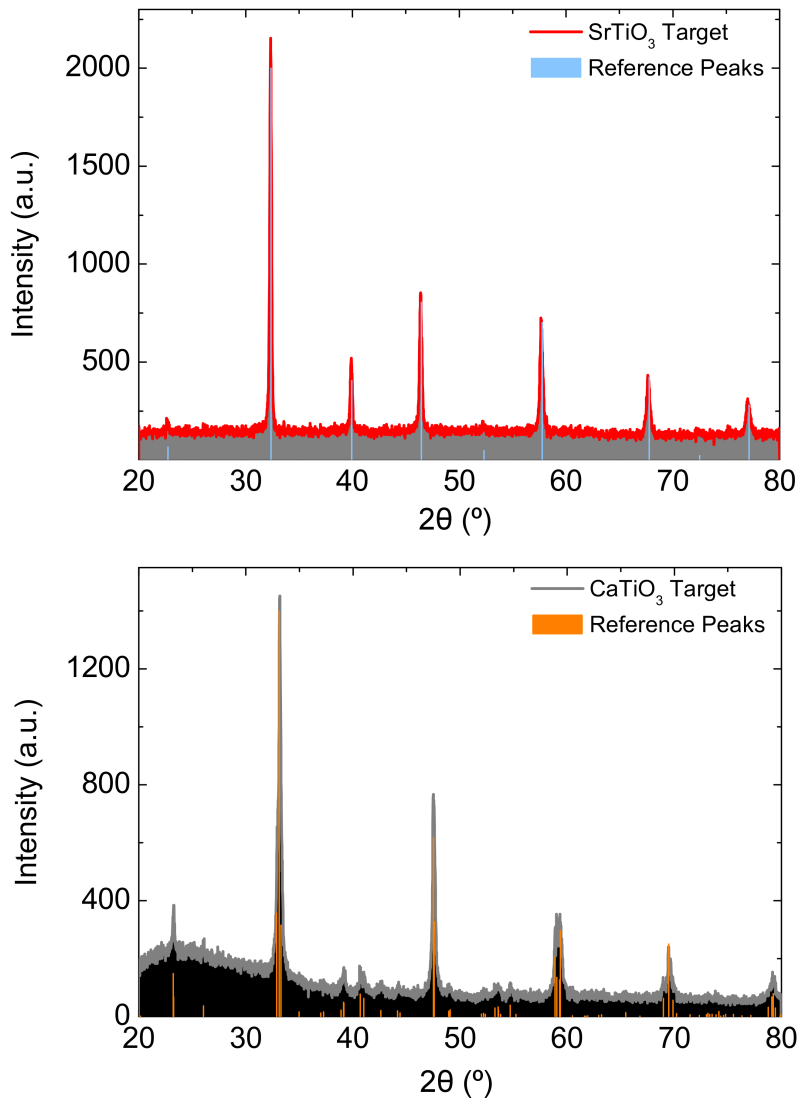
Figure 2.2: X-ray powder diffraction pattern of the Nb:STO [top] and CTO [bottom] target with the corresponding reference peaks for each one.
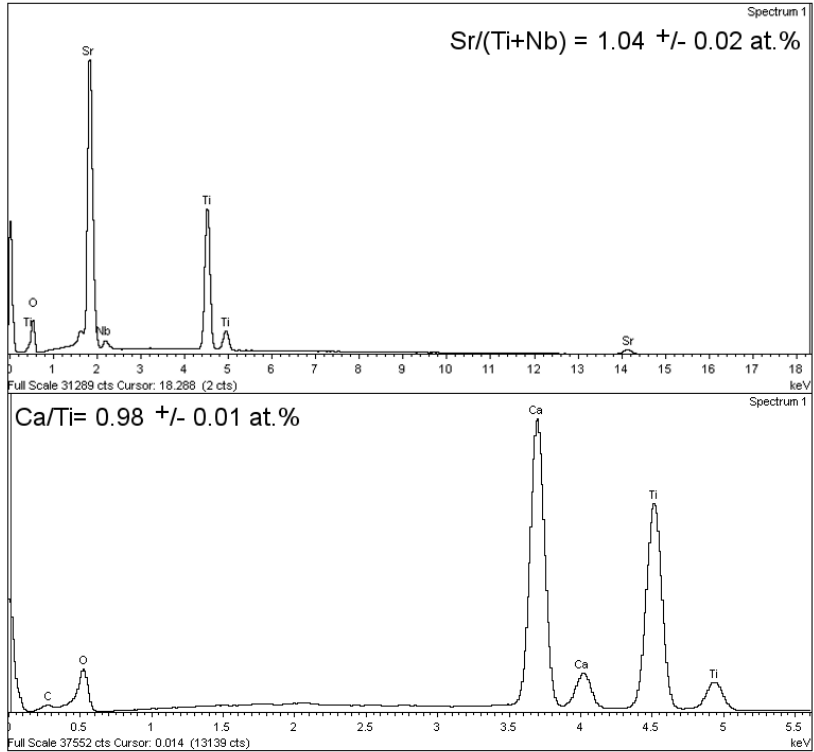
Figure 2.3: EDS spectra of the Nb:STO [top] and CTO [bottom] target, in order to determine their stoichiometry. The Nb:STO and the CTO targets were close to stoichiometric, taking into account the accuracy of the technique.

2.1.3 Substrate preparation

In this work, the thin films were deposited on top of various different single crystalline substrates in order to study the effect of the compressive/tensile strain on the properties of the thin films. Each substrate, had to undergo a different treatment prior to the deposition in the PLD system, in order to secure the desired surface termination. [99] In the case of STO substrates purchased from (Crystec) (http://www.crystec.de/crystec-e.html), a wet etching procedure was followed, as described by M. Kareev *et al.* [100], so that the STO substrates have a TiO_2 termination, in the form of flat terraces.
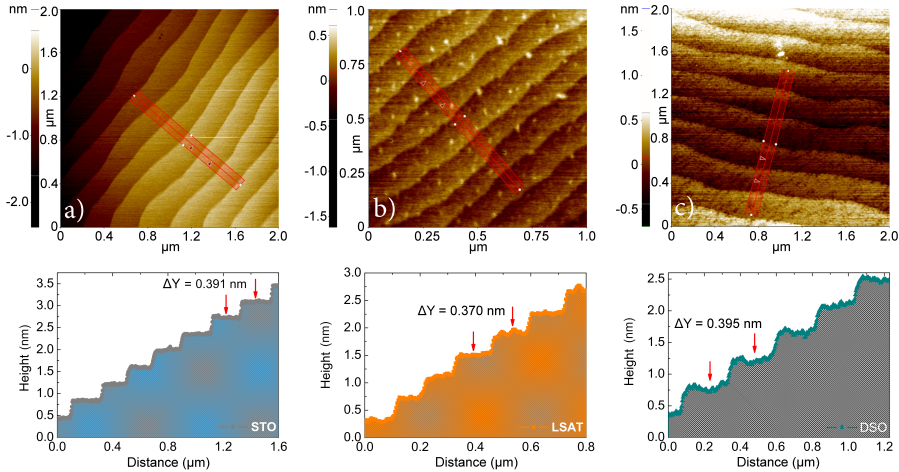

Figure 2.4: AFM image of the topography of (a) an STO, (b) an LSAT, and (c) a DSO substrate after surface treatments. Below each image is the line profile between adjacent terraces with their respective height difference, ΔY.

The STO substrates are submerged into deionized hot water (60℃) for 25 min, in order to induce the surface segregation of SrO particles. Then they are introduced into an acidic solution (3:1 $HCl:HN_2$) for 10 min and subsequently cleaned thoroughly with acetone and methanol (for 10 min each). Each of the previous steps are performed in an ultrasonic bath. Then, the substrates

are treated thermally at 1000℃ for 30 minutes in air, in order to achieve the recrystallization of the surface. After this process, the substrates are left with atomically flat TiO_2 terraces, as observed in AFM (see Fig.2.4).

Concerning the rest of the substrates that were used in this work, the $(LaAlO_3)_{0.3}(Sr_2AlTaO_5)_{0.7}$ (LSAT), $LaAlO_3$ (LAO) and $DyScO_3$ (DSO) as-received substrates were treated thermally in ambient atmosphere at 1300℃, 1000℃ and 1200℃, respectively in order to achieve smoother surface termination and surface reconstruction (see Fig. 2.4).

2.2   Structural characterization of the thin films

After the deposition process, we performed a careful structural characterization of the films. X-ray measurements provide information about the thickness and density of the films, as well as the crystalline quality, orientation, and epitaxial relation to the substrate. The theoretical models and formulas discussed in sections 2.2.1 and 2.2.2 have been extracted for the book *Thin Film Analysis by X-Ray Scattering* by M. Birkholz. [101] The equipment used for this work was a PANalytical's Empyrean diffractometer with an Euler cradle and a *Cu* X-ray source ($\lambda_{K\alpha 1} = 1.5405$ Å, $\lambda_{K\alpha 2} = 1.5443$ Å). This diffractometer permits the individual adjustment of various angles between the sample and the X-ray source/detector, as depicted in the schematic illustration in Figure 2.5

2.2.1   X-ray reflectivity

X-ray reflectivity is a surface-sensitive technique used to characterize the thickness and roughness of thin films and multilayers. In this method the diffractometer is operating in the symmetric $\theta/2\theta$ configuration, at very small θ angles. In contrast to the wide-angle diffraction scan, the XRR experiment has to be performed in
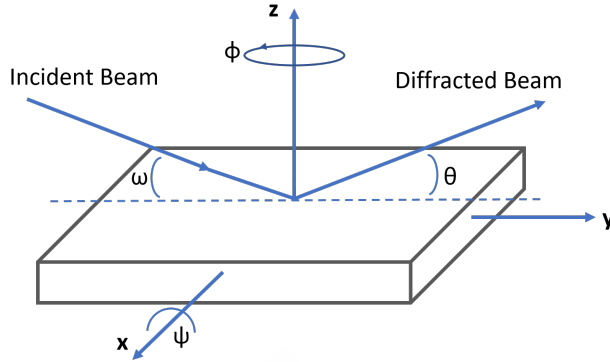
Figure 2.5: Schematic illustration of the adjustable parameters in the diffractometer (PANAlytical, Empyrean) that was used in this work. ω is the angle between the incident X-ray beam and the sample surface, θ is the scattering angle between the sample surface and the detector. ψ is the polar angle and ϕ is the azimuthial angle. In addition, x, y and z correspond to the horizontal and vertical displacements of the sample, which can be adjusted independently of each other.

the parallel beam configuration, i.e. the in-plane beam divergence should not exceed 0.05°and ideally would be even lower.

After the measurement, the plot of the intensity as a function of the scattering angle 2θ presents two characteristic features. The first one is the critical angle: θ_c. When $\theta < \theta_c$, the X-ray beam is totally reflected at the surface of the sample. The position of θ_c depends on the difference between the density of the substrate and the thin film. The second one are the intensity oscillations, or better known as the Kiessig oscillations or Kiessing fringes.

The maximum intensities are observed whenever the phase difference Δ between the reflected and refracted beam is a multiple of the wavelength λ. The phase difference Δ between two beams is given by the relation (see Fig. 2.6)

$$\Delta = (AB + BC)n - AD \qquad (2.1)$$

between the individual path lengths of both beams, where n is the refractive index of the film. Elaborating this relation, we get
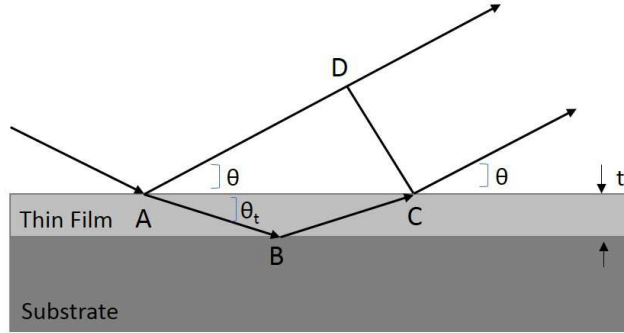
48

Figure 2.6: Schematic representation of the reflected and refracted beams for the derivation of their phase difference, Δ.

$$\Delta = 2\mathrm{t}\sin\theta_t \qquad \text{or} \qquad \Delta \approx 2\mathrm{t}\theta_t = 2\mathrm{t}\sqrt{\theta^2 - \theta_c^2} \qquad (2.2)$$

The left-hand equation of the phase difference relation is similar to the Bragg equation, with the film thickness t substituting the interplanar spacing d. A maximum is observed whenever the phase difference is a multiple of the wavelength $\Delta = m\lambda$. The distance between two adjacent fringes for $2\theta_{m+1}$ and $2\theta_m$, significantly above θ_c scales like

$$2\theta_{m+1} - 2\theta_m \approx \frac{\lambda}{\mathrm{t}} \qquad (2.3)$$

The film's thickness and density analysis of the XRR measurement is made using PANalytical's X'Pert Reflectivity software (see Fig. 2.7). The determination of t is performed automatically by fitting the reflectivity curve with the thickness t, density ρ and surface/interface roughness R, as free parameter. The rest of the parameters (such as number of layers, type of materials, etc) are introduced previously in the fitting software.
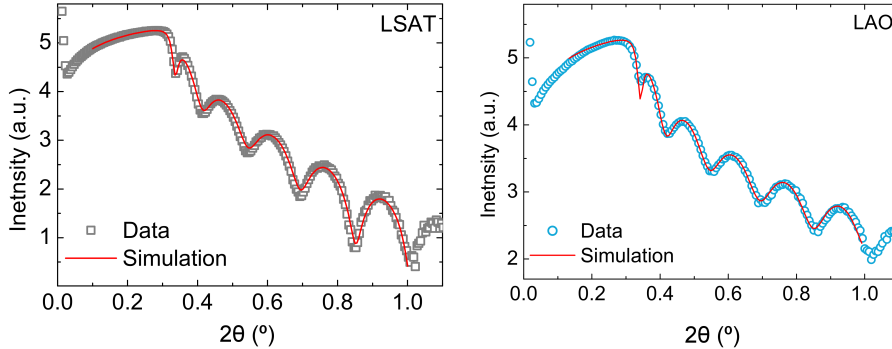
Figure 2.7: Representation of the experimental data (open squares) of the reflectivity measurement for the Nb:STO film on top of LSAT [left] and LAO [right] substrate, along with the simulation (red line) performed by the software X'Pert Reflectivity. The adjusted parameters for the simulation are density, thickness and roughness. For this particular fitting, the results were $\rho = 5.089$ g/cm^3, $t = 25.401$ nm and roughness = 1.47 nm for the LSAT substrate and $\rho = 5.173$ g/cm^3, $t = 25.606$ nm and roughness = 0.64 nm for the LAO substrate.

2.2.2 X-ray diffraction

The lattice parameters of the films were obtained from High Resolution X-Ray Diffraction (HRXRD) experiments in different configurations.

$\theta - 2\theta$ scan In this configuration, the X-ray beam is directed towards the sample at an incident angle ω, while the detector is placed at the same angle $\theta = \omega$ in order to pick up the scattered beam. Throughout the measurement the X-ray source and the detector are placed in various different angles but always maintaining the $\theta = \omega$ relation. In this measurement, only the *hkl* lattice planes that are parallel to the surface contribute to the Bragg reflections, where the Bragg relation has to be satisfied:

$$n\lambda = 2d_{hlk}\sin\theta \qquad (2.4)$$

where n is the order of the reflection, λ is the wavelength used by the X-ray source, d_{hkl} is the inter-planar distance of the crystal
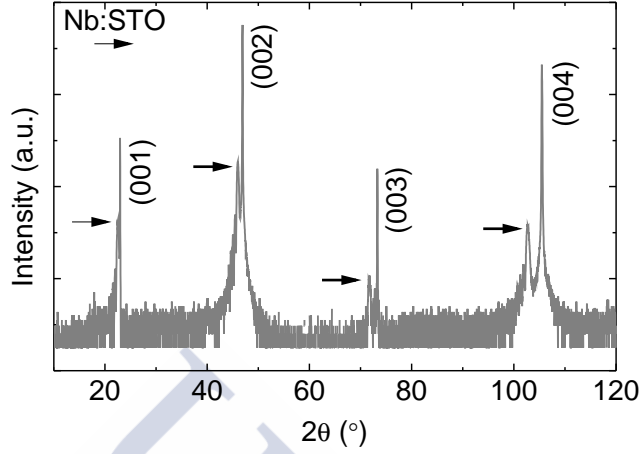
Figure 2.8: XRD $\theta - 2\theta$ pattern of a Nb:STO thin film deposited on top of an STO substrate. Only the (00l) reflections of the film and the substrate are present.

planes with the corresponding Miller index and θ is the Bragg angle. This type of measurement provides information about the relative crystallographic orientation of the thin film and the substrate, and it is the most common way to determine the lattice parameters of the film corresponding to the planes perpendicular to the surface (see Fig. 2.8).

In Figure 2.9 we show the X-ray $\theta - 2\theta$ diffraction pattern for a Nb:STO thin film grown on top of an LSAT substrate. The measurement is centered around the (002) reflection of the film and substrate. The out-of-plane lattice parameter of the film, in this case the c-axis lattice parameter, can be obtained from these data, using :

$$c = \frac{\lambda\sqrt{h^2 + k^2 + l^2}}{2\sin\theta} \qquad (2.5)$$

Moreover, we can observe the presence of interference fringes close to the diffraction peak of the film (Laue oscillations). They
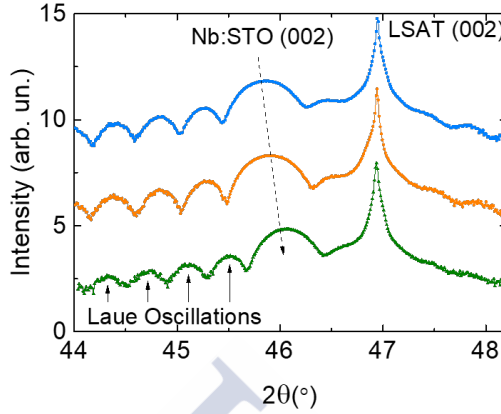
Figure 2.9: XRD $\theta - 2\theta$ pattern around the (002) reflection of the LSAT substrate of a Nb:STO thin film deposited at different PO$_2$ ($10^{-1} - 10^{-3}$ Torr). High crystalline quality of the film produces Laue oscillations in the diffraction pattern. The dashed arrow indicates the displacement of the peak of the film based on the PO$_2$ used during the deposition.

have essentially the same origin as the Kiessig fringes observed in the X-ray reflectivity measurements, but in this case the X-ray interference is caused by the reflection between the atomic planes of the film. Therefore, the observation of these oscillations around the diffraction peak is a signature of the high crystalline quality and low disorder in the film. From the position of the fringes it is possible to calculate the thickness t of the film :

$$t = \frac{\lambda}{\Delta\theta_m} \frac{1}{2\cos\theta} \tag{2.6}$$

where $\Delta\theta_m$ is the distance between the fringes of order m. This formula is a very useful tool to determine the film's thickness from the fringe spacing for planes parallel to the surface.

The film depicted in Figure 2.10 is the same film as in Figure 2.7. The resulting thickness of the film using the calculation from the Laue oscillations yields $t = 25.62$ nm, whereas the calculated thickness for the same film through the XRR fitting was $t = 25.4$
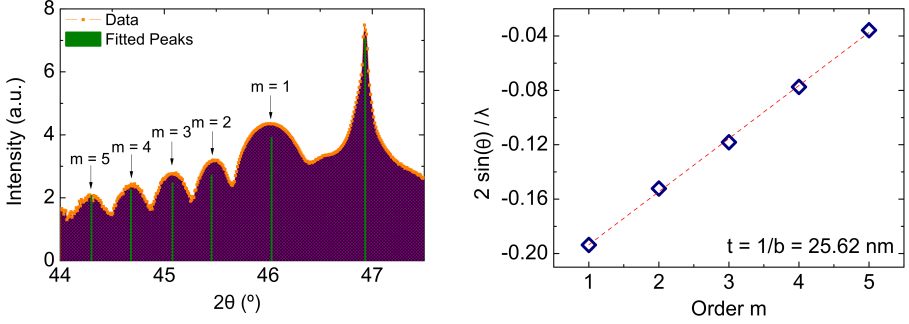
Figure 2.10: Left: XRD $\theta - 2\theta$ pattern of a Nb:STO thin film deposited on top of an LSAT, around the (002) reflection of the substrate. High crystalline quality of the film produces Laue oscillations in the diffraction pattern. Right: Calculating the thickness of the film using Eq. 2.6. Taking into account the results for orders $m = 1 - m = 5$, the resulting thickness is 25.62 nm.

nm, indicating a good agreement between the two methods.

2.2.3 Reciprocal space mapping

Reciprocal Space Mapping is an $\omega - 2\theta$ type of scan, where ω is the angle of the incident X-ray beam. This scan is performed around an asymmetrical reflection and reconstructs a two-dimensional image providing information about the in and out-of plane lattice parameters of the film, as well as the relaxation of the epitaxial stress of the film grown on a given substrate.

A series of 2θ scans are executed for a determined ω angle range, with the rest of the parameters remaining constant. The two-dimensional representation of the scan can be reconstructed by calculating the reciprocal space vectors Q_x and Q_y using the following expressions:

$$Q_x = \sin\theta \sin(\theta - \omega) \tag{2.7}$$

$$Q_y = \sin\theta \cos(\theta - \omega) \tag{2.8}$$

It is possible to extract the real space lattice parameters of the films, using the reciprocal space vectors for determined crystal structures. For the case of cubic lattice, the in-plane ($\alpha = \beta$) and out-of-plane (c) lattice parameters are calculated by the following expressions:

$$a = \frac{\lambda \sqrt{h^2 + k^2}}{2Q_x} \tag{2.9}$$
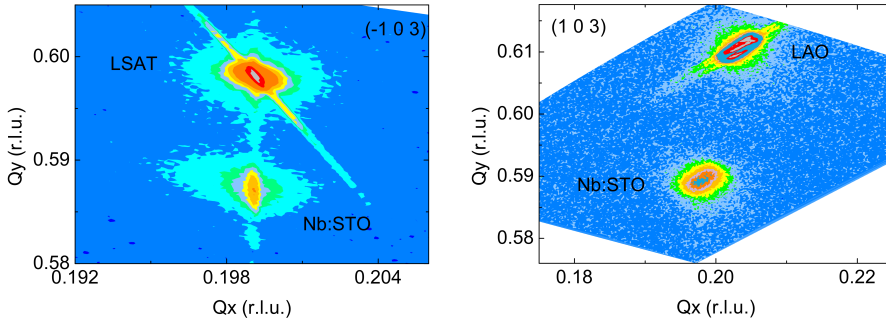
$$c = \frac{\lambda l}{2Q_y} \tag{2.10}$$

Figure 2.11: Reciprocal space maps around the asymmetric (103) and ($\bar{1}$03) reflections for Nb:STO thin films deposited on top of (001)-oriented LSAT [left] and (001)-oriented LAO substrate [right]. The film on LSAT grows fully strained to the substrate, as shown by their identical in-plane lattice parameter, Q_x. The film on top of LAO substrate grows partially relaxed, with a larger in-plane lattice parameter than the substrate.

Performing this type of scans gives visual information whether the thin films grow on top of a substrate adapting their lattice parameters, or not. An example is depicted in Figure 2.11. It is clear that while the in-plane lattice parameters of the STO thin film deposited on top of the LSAT substrate are matched to the substrate, the same film deposited on top of LAO substrate fails to adapt on the much smaller in-plane lattice parameters of the substrate and grows partially relaxed.

2.2.4 Half-order Bragg reflections

The RSM scans are very useful in order to study the rotation/ distortion of the BO_6 octahedra in the crystal structure of the ABO_3 perovskite materials.

As explained in section 1.5, these cooperative octahedral rotations accommodate the reduction of the $B-O-B$ angles and $B-O$ bond lengths produced by cationic substitutions in the perovskite structure. They, therefore, change the orbital hybridization, and may determine, to a large extent, the functionality of many perovskite oxides. [102, 103, 104, 11, 105]

Given that these cooperative octahedral rotations produce a change (doubling along certain directions) in the unit cell symmetry, they can be characterized by following a series of distinctive Bragg peaks occurring at half-order positions.
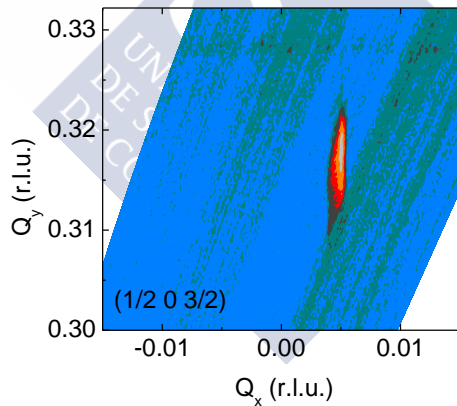
Figure 2.12: Reciprocal space map of the half-order Bragg reflection $(\frac{1}{2}0\frac{3}{2})$ for an STO thin film deposited on top of an STO substrate at $PO_2 = 10^{-5}$ Torr. The existence of this peak indicates an in-phase rotation of the TiO_6 octahedra along the b-axis: b^+ in Glazer's notation.

Using the laboratory Empyrean diffractometer was sufficient to detect the presence or absence of the BO_6 octahedral rotations in the thin films, in spite of their low intensity. In order to detect the

half-order Bragg reflections, a doubled unit cell was constructed in the database of the equipment and then we performed RSM scans around the appropriate half-ordered reflections that would predict the presence or absence of rotations along the three pseudocubic axes (see Fig. 2.12). From the previously measured lattice parameters of our films and using the Bragg equation Eq. 2.4, we predicted the 2θ angle where the peak of the corresponding reflection would appear, and performed careful $\omega - 2\theta$ scans to detect/discard a particular TiO_6 rotation pattern.

2.2.5   Scanning transmission electron microscopy

Another important technique to evaluate the crystal structure quality of the samples is the scanning transmission electron microscopy (STEM). This technique allows to visualize the thin films and the interfaces with the substrates, as well as identify imperfections of the crystal structure, such as dislocations, vacancies, interfacial atomic diffusion with the substrate, etc. The measurements performed for this work were made at The Laboratorio de Microscopías Avanzadas at the Instituto de Nanociencia de Aragón (LMA-INA), ARAID Foundation, in Zaragoza, Spain. The equipment used was a FEI Titan Low Base, with a resolution of <1 Å. The samples (cross-section lamellae) preparation was made using a focused-ion beam (FIB) microscope in order to reduce the thickness of the sample, so that the film and interface can be examined.

A typical STEM image of interfaces captured with a STEM is depicted in Figure 2.13, where identical thin films were deposited side-by-side on two different substrates, STO [left] and LSAT [right].

Furthermore, it is possible to perform qualitative and quantitative stoichiometric analysis of the thin films. The two usually implemented techniques are electron energy loss spectroscopy (EELS) and electron energy dispersive spectroscopy (EDS or EDX). Due to the composition of the films, EELS study could not verify the stoichiometry quantitatively because Nb and Sr high energy loss and very small signal to be detected. However, using EDX it was possi-
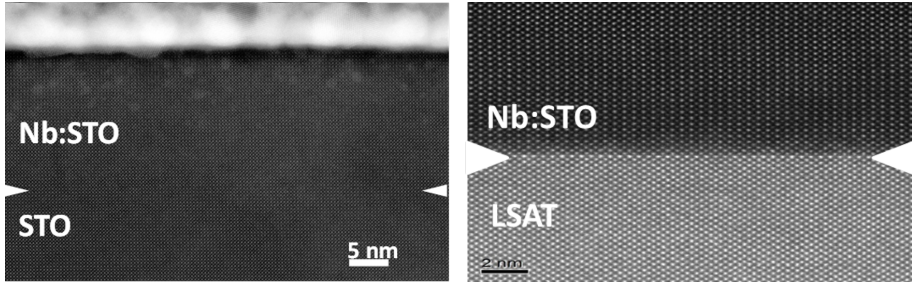
Figure 2.13: TEM image of the interface of a Nb:STO thin film on top of an STO [left] and an LSAT [right] substrate.

ble to determine the composition of the films (see Fig. 2.14). The peaks of Sr and Nb are more separated and somehow more intense. The results of the EDX composition analysis were: Ti $\approx 48 \pm 0.5$ at.%, Sr $\approx 50.3 \pm 1.0$ at.% and Nb $\approx 1.7 \pm 0.4$ at.%, yielding a nearly 1:1 cationic ratio.

Figure 2.14: EDX spectra for a Nb:STO thin film on top of an STO substrate. The peak intensities are relatively high, which permits the extraction of reliable quantitative results about the composition of the thin films.

2.2.6 Atomic force microscopy

Atomic force microscopy (AFM) is a powerful microscopic technique that gives information about the surface properties of the samples. Since its invention by Binning *et al.* [106] in 1986 it has played crucial role in the understanding and exploration of the morphology and the ph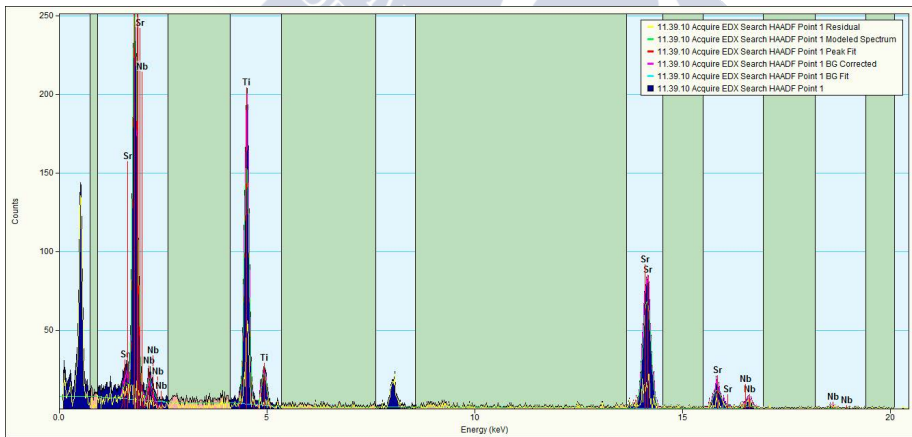ysical properties of the samples' surface in the nanoscale regime. The principle of its function lies on the attractive or repulsive interaction forces between the atoms of the cantilever tip and the atoms of the sample's surface. The attractive forces are mainly short-range chemical forces, van der Waals and electrostatic force. When measuring in this regime, the AFM tip and the sample are not in contact and, depending on the sample-tip distance, one force is more dominant than the other - since their effective range is different.

The AFM tip is mounted on a vibrating cantilever and its motion is being monitored by a laser beam which is being reflected on the cantilever to a photodiode, where the signal is being analyzed (see Fig. 2.15). As the cantilever scans the surface of the sample, any changes in the morphology of the surface provoke changes on the reflected laser beam and, thus, on the signal recorded by the photo-diode. This way, a two-dimensional image can be reconstructed that represents the surface of the sample with atomic accuracy.

In this thesis, topographic imaging were performed in order to examine the surface termination and roughness of the films, mainly using the non-contact mode of measurement. In addition to the topography, electric force microscopy (EFM), piezoelectric force microscopy (PFM) and scanning Kelvin probe microscopy measurements (SKPM) have been implemented in order to study the surface electrical potential and/or the ferroelectric response of the samples.

EFM is a non-contact technique that permits the detection of surface electric potential of the sample due to the electrostatic forces between the sample and the AFM tip, at the same time that the surface topography is measured. In EFM mode, a lock-in amplifier
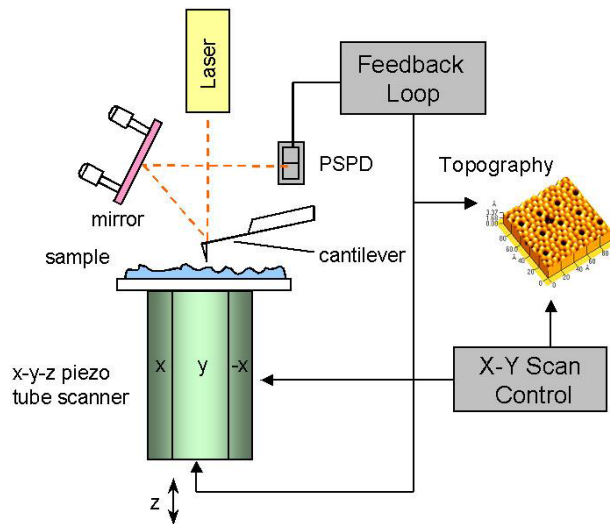
Figure 2.15: Schematic illustration of the AFM working principles. While the cantilever scans the surface of the sample, its movement is being monitored by a laser beam reflected on the cantilever and analyzed by a photodiode which converts the light to electrical signal and then reconstructed by the software to a topography image of the surface. Image by Park Systems. [107]

applies an AC voltage to the conductive EFM tip over a conventional DC bias voltage applied by the controller. The lock-in also reads the same frequency component from the output signal. The total voltage between the tip and the sample can then be expressed as: [108, 109]

$$V(t) = V_{DC} - V_S + V_{AC}\sin\omega t \qquad (2.11)$$

where, V_{DC} is the DC offset potential, V_S is the surface potential of the sample and V_{AC} and ω is the amplitude and frequency of the applied AC potential, respectively. From these data, the surface potential of the sample can be accurately determined. The frequency ω is chosen smaller (14-17KHz) that the cantilever oscillation frequency (70-330KHz) so that the two signals don't interfere.

The SKPM mode uses the same configuration as the EFM mode and can be used to map the surface potential of the sample. However, it is much less sensitive to topographic effects. An example of EFM and SKPM images taken on the same sample is shown in Figure 2.16.

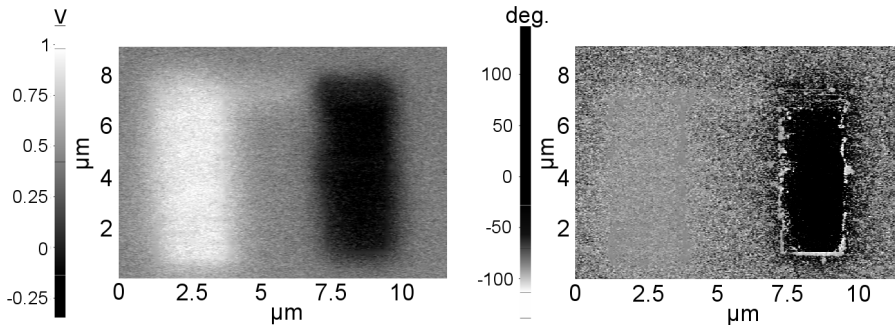Figure 2.16: EFM images of the surface potential SKPM [left] and the EFM phase [right] on a 23 nm film of CTO on top of LAO substrate, deposited at $PO_2 = 10^{-6}$ Torr. The two distinct regions have been previously polled with $-10V$ (left region) and $+10V$ (right region).

In order to study the ferroelectric response of a sample, we can use the PFM mode, in which the tip is in direct contact with the

sample and can detect the distribution of remnant polarization of the sample. While the conductive AFM tip is in contact with the sample, a pre-set voltage is applied between the tip and the sample, establishing an external electric field inside the sample. In a ferroelectric/piezoelectric material this would lead to *electrostriction*, where the sample can locally expand or contract, depending on the direction of the electric field. This local polarization is detected bt the tip, and from this we can estimate the local polarization of the sample.
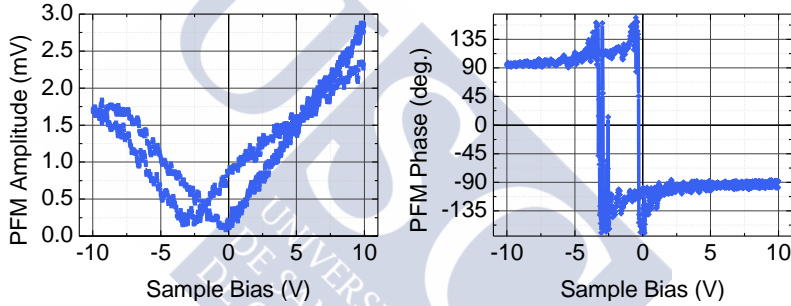
Figure 2.17: Piezoelectric response spectroscopy (PFM spectroscopy) results. The data correspond to a 23 nm CTO thin film deposited on top of LAO substrate at $PO_2 = 10^{-6}$ Torr.

In addition, it is possible to perform PFM spectroscopy in a single point of the sample. While the tip is in contact with the sample and does not move, a voltage sweep is made (typically from $-10V$ to $+10V$) and the response of the sample is recorded. For a ferroelectric sample this would lead to the typical hysteresis loop in the *Phase vs Sample Bias* and butterfly pattern of the *Amplitude vs Sample Bias* graphs (see Fig. 2.17).

The equipment used in this thesis for the AFM/EFM/PFM measurements is an NX-10 Park Systems atomic force microscope, for which there are various modules that can be used in order to perform different types of measurements. The probes used for the sim-

ple topography images were either ACTA (Force constant: 37 N/m, Frequency: 300kHz - Appnano) or AR5-NCHR (Force constant: 42 N/m, Frequency: 320kHz - Nanosensors), both non-contact. For the EFM/SKPM/PFM measurements, the probe that was used is ElectriMulti75-G (Force constant: 3 N/m, Frequency: 75kHz - Budget Sensors), which is Cr/Pt coated and can perform both contact and non-contact measurements.

2.3   Electrical and Seebeck coefficient measurements

In this section we describe the methods used to study the transport properties of the samples (electrical resistivity and Hall effect) and the Seebeck coefficient. For all these measurements the following equipment has been used: a Keithley 2152A nanovoltimeter, a Keithley 6221 AC current source, a Keithley 2400 source meter, a Lakeshore 332 temperature controller, a Keithley 4200-SCS semiconductor characterization system, and a GW magnet with a magnetic field range of ± 1.2 T. All the equipment was controlled and the data collected by custom software designed in Labview. For the electrical contacts, aluminum wire of 25 μm were bonded to the small Cr/Au pads on the sample surface.

All measurements were performed under dynamic vacuum ($\approx$ 10^{-6} mbar). The temperature dependent measurements were performed in the range of $5-300$ K in a Janis Research continuous flow cryostat or in a Helium closed loop ARS cryostat. Specific magnetoresistance measurements at lower temperatures were performed in a PPMS (Quantum Design).

2.3.1   Electrical resistivity

The electrical resistivity of the samples was measured by the Van der Pauw technique. [110]. The samples have a flat shape and a uniform thickness, without holes or inhomogeneities and are isotropic

with respect to the electrical transport. We place four contacts on each corner of the sample. The area of the electrical contacts was always much smaller than the area of the entire sample.
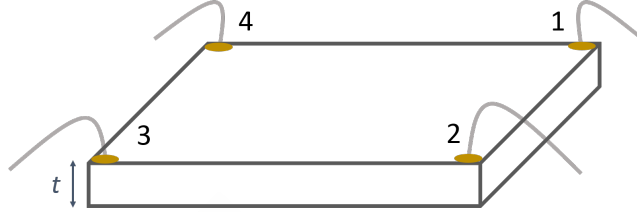
Figure 2.18: Schematic illustration of the measurement setup for the Van der Pauw method. The current is injected from one side (I_{12}) and the voltage drop is measured on the opposite side V_{34}. The measurement is repeated for all four sides of the sample, rotating clockwise the contacts of current injection and voltage drop measurement.

For the measurements, an electrical current is injected from one side of the sample (I_{12}) and the voltage is measured at the opposite side (V_{34}). This way we can define the resistance as:

$$R_{12,34} = \frac{V_{34}}{I_{12}} \tag{2.12}$$

To make this measurement more precise (avoiding contributions from a thermoelectric voltage due to small temperature differences between the edges of the sample) we injected the current through all four sides ($R_{12,34}, R_{23,41}, R_{34,12}, R_{41,23}$) of the sample, and also invert the polarity for each measurement. The value of each R is calculated by the slope of the $I - V$ curve at each temperature. We can define the average resistance for two opposite sides as:

$$R_A = \frac{(R_{12,34} + R_{21,43} + R_{34,12} + R_{43,21})}{4}$$
$$\text{and} \tag{2.13}$$
$$R_B = \frac{(R_{23,41} + R_{32,14} + R_{41,23} + R_{14,32})}{4}$$

Finally this yields the Van der Pauw formula for the sheet resistance:

$$e^{-\pi \frac{R_A}{4R_s}} + e^{-\pi \frac{R_B}{4R_s}} = 1 \qquad (2.14)$$

In the case of our rectangular samples, the condition $R_A = R_B$ is satisfied, so we end up with the sheet resistance R_s as:

$$R_s = \frac{\pi R}{ln2} \qquad (2.15)$$

In order to obtain the resistivity ρ of our samples, it is enough to multiply the R_s with the thickness of the film, obtained by the XRR measurement.

$$\rho = \frac{\pi t}{ln2} R \qquad (2.16)$$

2.3.2 Hall effect

In order to determine the type and concentration of the charge carriers in the films, we performed measurements of the Hall effect.

When a magnetic field is applied in the direction z, while the current moves along the x direction, then the carriers due to the Lorenz force ($\mathbf{F} = q(\mathbf{v} \times \mathbf{B})$) will deviate in a direction perpendicular to both $\mathbf{B}$ and $\mathbf{I}$. This leads to the charge accumulation on one side of the sample and gives rise to the Hall voltage V_H. In the case of the existence of only one of the two type of carriers (*electrons* or *holes*), the sign of the V_H determines the specific type of charge carrier present in the sample. The carrier concentration can, then, be easily determined by the relation

$$V_H = R_H \frac{IB}{t} \qquad (2.17)$$

defining as

$$R_H = \frac{1}{qn} \qquad (2.18)$$
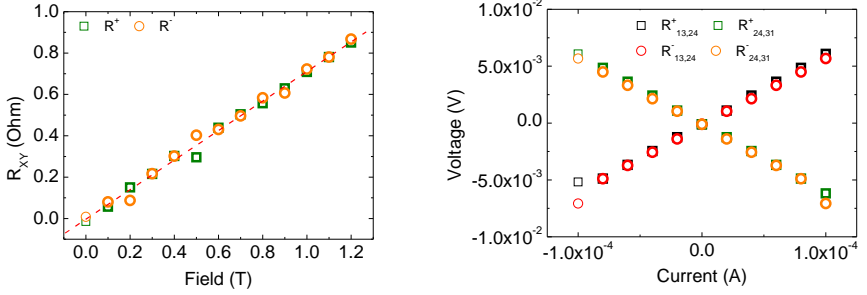
Figure 2.19: Left: Measuring the Hall coefficient twice for inverted direction of the magnetic field, so that offsets can cancel out. Right: I-V curves for the four different configurations of measurement.

the Hall constant.

In order to measure the Hall effect in our samples, we have implemented the Van der Pauw method (see Fig. 2.18), like we did for the electrical resistivity measurements. Extra care must be taken so that any contribution from the longitudinal magnetoresistance is not taken into account. For this reason, we inject the current through contacts 1 and 3 (I_{13}) and measure the voltage drop at 2 and 4 (V_{24}) and taking two measurements, one with positive magnetic field and one for negative (resulting in $R^+_{13,24}$ and $R^-_{13,24}$). After that, we repeat the same procedure by injecting the current I_{24} and measuring the voltage V_{31} (resulting in $R^+_{24,31}$ and $R^-_{24,31}$).

$$R_H = \frac{(R^+_{13,24} + R^+_{24,31}) - (R^-_{13,24} + R^-_{24,31})}{4} \qquad (2.19)$$

To determine R^+ and R^-, we measure the voltage drop for different values of current, keeping the magnetic field constant. The value of R^+ and R^- is given by the slope of the voltage versus the current. The same steps are followed for different values of the magnetic field, typically up to 1.2 T, with a step of 0.1T (see Fig. 2.19).

2.3.3 Seebeck coefficient

As explained in the first chapter of this thesis, the Seebeck coefficient is defined as the ratio of the voltage difference across the material and the temperature difference at these same points. The value of the Seebeck coefficient is given by the slope of ΔV over ΔT

$$S = \frac{\Delta V}{\Delta T} \tag{2.20}$$

For this purpose, we have designed and fabricated our custom setup which is based on the *heat-pulse* method and ensures great temperature gradient resolution (≤ 0.1 K) and immediate response of the Seebeck voltage (V_{Seeb}). The setup is depicted in Fig. 2.20.
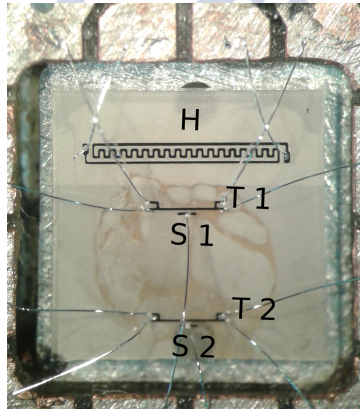
Figure 2.20: Image of the setup used for the Seebeck coefficient measurements. We have deposited via optical lithography and sputtering platinum resistances that are used as local thermometers (T1-T2) and heater (H). The heater has been electrically isolated from the rest of the film to prevent interference with the V_{Seeb} which is measured at the points S1-S2.

The pattern of the thermometers and the heater were transferred to our samples by optical lithography. Afterwards, we deposit via sputtering 5 nm of Cr (as an adhesive layer between the film and the platinum) and 70 nm of Pt - the width of the thermometers and heater was $w = 10\mu$m and the length $l = 1mm$. After the sputtering deposition is complete, we remove the photoresin in an

ultrasonic bath of acetone (5 min) and ethanol (5 min). The thermometers and heater were electrically contacted with aluminum wires, using a wire-bonding equipment.

Once we have the pattern deposited on the film, we glue the sample on a chip-carrier, using thermal or Ag-based paste to ensure good thermal contact. The sample is cooled under vacuum (typically $\approx 1 \times 10^{-6}$ Torr) in a cryostat.

Before the measurements, we injected a constant current (typically 1 mA) during 5 min, at the highest base temperature that will be used for the measurements. This procedure favors the recrystalization of the Pt resistances and favors their thermal stability and reproducibility of the measurements.
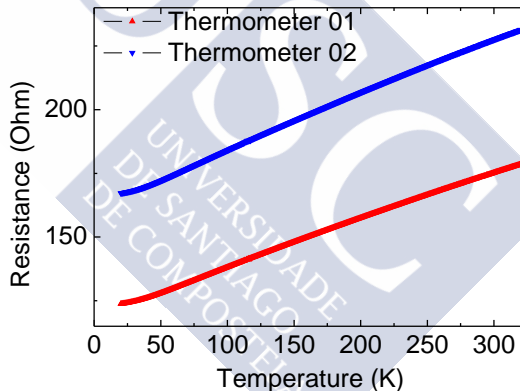
Figure 2.21: Temperature dependent resistance of the two thermometers used in the Seebeck measurements. Each value of the resistance corresponds to a certain temperature, which allows the precise measurement of the local temperature in the film.

The second step is to calibrate the thermometers, running a slow ramp (0.5 to 1 K/min) throughout the whole temperature range for our measurements (see Fig. 2.21). This way we assign a certain temperature to a given value of the Pt resistances, which will be used in order to locally determine the temperature gradient

created later by the heater. After the calibration of the thermome-
ters, we are ready to proceed with the measurement.

We stabilize the sample to the desired base temperature, long
enough so that we can assure that there is no temperature gradient
on the sample, which can be monitored through the signal of the
V_{Seeb}. After the thermal stabilization, we begin to inject current to
the heater in order to create a temperature gradient between the
two thermometers and the adjacent points of measurement of the
V_{Seeb}. After a very short time, the temperature gradient is constant.
Subsequently, we increase the value of the heater's current in order
to create larger thermal gradient, typically up to $\approx 1 - 2$ K. The
stabilization of the thermal gradient and the response of the V_{Seeb} is
rapid and it allows the very accurate determination of the Seebeck
coefficient, as it can be observed in Figure 2.22. Special care was
taken not to increase the base temperature during the measurement
more than ≈ 8 K. This is particularly important when studying
samples close to a phase transition, where the Seebeck coefficient
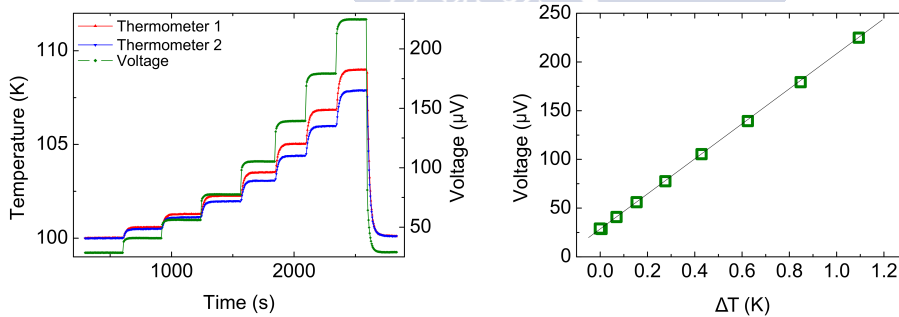may vary rapidly with temperature.

Figure 2.22: Left: Creation of the thermal gradient steps, due to increasing
values of the current injected in the Pt heater (red line: thermometer 1 and
blue line: thermometer 2; green line corresponds to the values of the Seebeck
voltage. Right: Thermal gradient vs Seebeck voltage. The slope of this linear
fit is used to calculate the Seebeck coefficient.

2.4 Thermal conductivity measurements

The thermal conductivity is an important transport property, which may give valuable information about the lattice dynamics in an insulating material. Moreover, it is one of the magnitudes which define the efficiency of a thermoelectric material. In this thesis, two different methods were used to measure the thermal conductivity of the thin films: the frequency domain thermoreflectance (FDTR), and the 3-ω method.

2.4.1 Frequency domain thermoreflectance

All the measurements performed with this technique were done at the Mechanical Engineering department at the Carnegie Mellon University, under the supervision of Professor Jonathan A. Malen, during two separate short-term visits (Sept - Nov. 2016 and Apr - Jun. 2017).

FDTR is a non-contact optical technique used to determine the thermal conductivity of a solid material (liquid materials require a modified setup). It is a quite versatile technique since it is possible to measure numerous different kind of samples, from bulk to thin films and organic to inorganic materials, with a wide range of thermal conductivities, from <1 to 1000 W/m K. FDTR can also measure the interface thermal resistances between the various layers, as long as the values of the resistance is larger than 5 m²K/GW. [111, 112]

In addition, it requires minimal sample preparation; only a thin metal layer (typically Au as the transducer) is deposited on the surface on the sample. One of the limitations is that the sample is required to have a flat and smooth surface, since FDTR relies on laser reflections. The thermal conductivity of the sample and the sum of the interface thermal conductance are calculated by fitting the experimental data to an analytical model, [113] as discussed in Appendix A.

A schematic of the FDTR setup is depicted in Figure 2.23. This
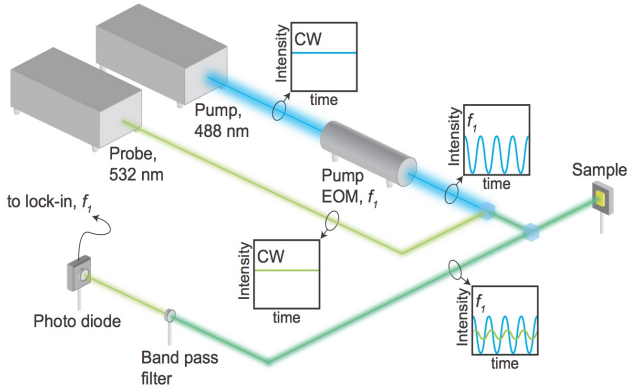
Figure 2.23: Schematic representation of the FDTR setup

technique implements two different continuous wave laser sources, denoted as the *pump* and the *probe*. The pump laser (488 nm) passes through an electro-optical modulator (EOM) in order to obtain a sinusoidally intensity-modulated wave.

Then, the pump and probe laser beams are co-aligned in a beam combiner and passed through a polarizing beam splitter (PBS) that reflects both beams in a 90°angle towards the sample. Just before the mounted sample, the beams pass through a quarter-wave plate and the objective (in this work a $20x$ magnification objective was used) that focuses the beams on the surface of the sample. The pump laser beam impacts on the sample surface (covered by Au), creating a sinusoidal heat flux, and a periodic temperature oscillation. This temperature oscillation is detected by the probe laser beam, by measuring the time variations of the reflective index.

Both beams are reflected by the sample and are guided to a photodiode which converts the incoming laser beams to electrical signal, which is measured by a lock-in amplifier.

After the measurement is made, the experimental data of the phase difference between the pump and the probe laser beams are fitted to a thermal transport model explained in Appendix A (see Fig. 2.24), where the only free parameters are the thermal conductivity of the film and the sum of all the interface thermal resistances
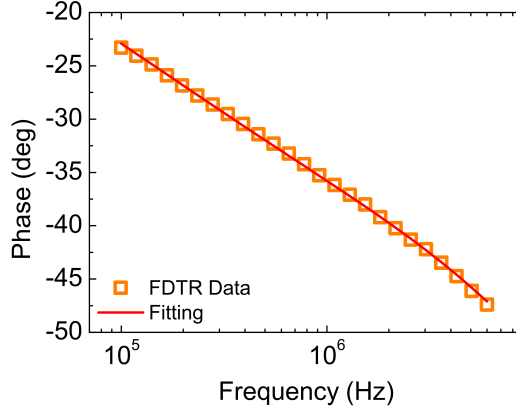
Figure 2.24: Obtained FDTR data (open symbols) and the fitted simulation (solid line) that yields the value of the *effective thermal conductivity*

(the boundaries between substrate/film and film/transducer).

The local heat flux density q'' across the sample is equal to the product of thermal conductivity κ and the local temperature gradient $-\nabla T$ created by the laser (assuming a one-dimensional propagation):

$$
\begin{aligned}
q'' &= -\kappa \nabla T = -\kappa \left(\frac{\Delta T}{\Delta x} \right) \\
&= - \left(\frac{\kappa}{\Delta x} \right) \Delta T \Leftrightarrow \Delta T = -q'' \frac{\Delta x}{\kappa}
\end{aligned}
\tag{2.21}
$$

where Δx would be the thickness of the film and $\Delta x / \kappa$ represents the thermal resistance imposed by the material to the heat propagation. The total thermal resistance includes contributions from the film's thermal resistance, and from the various interfaces (substrate/film/Cr/Au) present in the sample. We can linearize this equation, summing all the resistances of the different interfaces in a single term:

$$
\frac{\Delta x}{\kappa} = \frac{\Delta x}{\kappa_{film}} + R_{Interface}
\tag{2.22}
$$

71
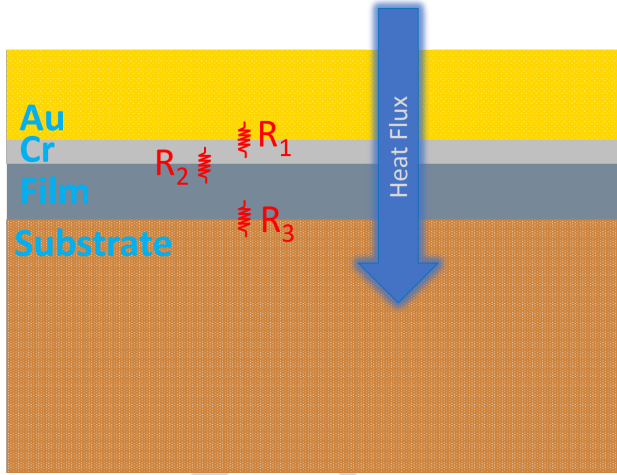
Figure 2.25: Schematic illustration of the cross section of the samples measured using the FDTR method. Between the layers of Au, Cr, thin film and the substrate there are three different interfaces that contribute to the total thermal resistance of the system for the cross plane propagation of the heat flow.

Thus, plotting $\frac{\Delta x}{\kappa_{measured}}$ vs Δx for several different thicknesses of the same film composition, provides the thermal resistance between the film and the interface (see Fig. 2.26). In this model , we have made the assumption that the thermal conductivity is independent of the films' thickness, which is an approximation validated by the results, *i.e.* as long as the data fit to a straight line.

The resulting thermal conductivity values, typically present uncertainties of the order of $10 - 25\%$ due to the goodness of the fittings of the heat conduction model and the input parameter uncertainties, such as the film thickness, heat capacity the laser spot diameter and the Au/Cr film thickness. In an attempt to minimize these uncertainties we have measured different spots of the film, until we could get reproducible results.

In FDTR, it is also necessary to measure the heat capacity of the substrate, as well as the thermal conductivity of the substrate and the transducer Au film.
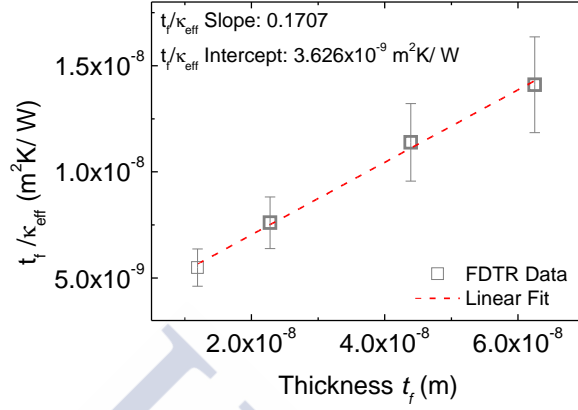
Figure 2.26: Linear fitting of the effective thermal resistance implemented for the four different thicknesses of the films. The thermal conductivity and the interface thermal conductance are extracted by the slope and intercept of the linear fitting, respectively. The data correspond to Nb:STO films deposited on STO substrates at $PO_2 = 0.01$ Torr
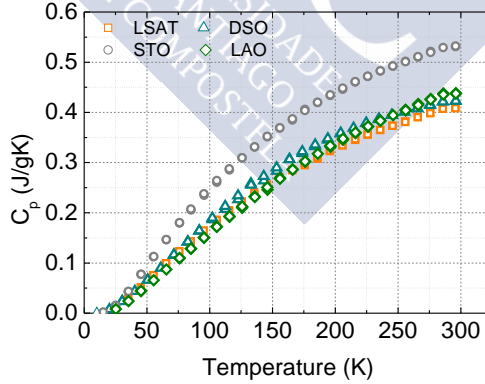
Figure 2.27: Heat capacity of the four different substrates used in this thesis for the thermal conductivity measurements. LSAT, STO, DSO and LAO correspond to $(LaAlO_3)_{0.3}$-$(Sr_2AlTaO_6)_{0.7}$, $SrTiO_3$, $DyScO_3$, and $LaAlO_3$

The heat capacities of the various substrates were measured separately in a PPMS equipment (see Fig.2.27).

For κ the Au film, a glass substrate was introduced to the sputtering chamber and a layer of Cr/Au film was deposited on top of it. We then measured the electrical resistivity and used the Wiedemann-Franz law to obtain its thermal conductivity.

The temperature dependent FTDR $\kappa(T)$ measurements were performed using a cryostat with an optical window, under continuous N_2 flow evaporated from liquid N_2, controlled by an external mass flow controller. The base temperature was adjusted by combining the external N_2 flow and an external heater. The rest of the procedure was identical to the room temperature measurements.

2.4.2 The 3-ω technique

The temperature dependence of some of the films presented in this thesis was independently measured by the $3-\omega$ method. [114, 115] This method uses a metallic strip (in this work Pt) deposited on top of the sample, that serves both as the heater and the temperature sensor. We have deposited a Cr/Pt (10 nm/90 nm) by optical lithography and sputtering, 10 μm wide and 1 mm long (see Fig. 2.30). It is important to have a wide Pt strip compared tho the thickness of the thin film, so that we can assume a one dimensional cross-plane heat flux inside the film.

An AC-current with angular frequency ω is driven through the Pt strip which produces a conventional Joule heating on the sample's surface at a frequency of 2ω. This temperature oscillations (ΔT) on the sample's surface produce a small voltage drop along the Pt strip at a frequency of 3ω, which provides information on the heat transport inside the sample. The magnitude of the temperature oscillations can be described by the following relation

$$\Delta T = \frac{Re[V_{3\omega}]4R}{\frac{dR}{dT}} \qquad (2.23)$$
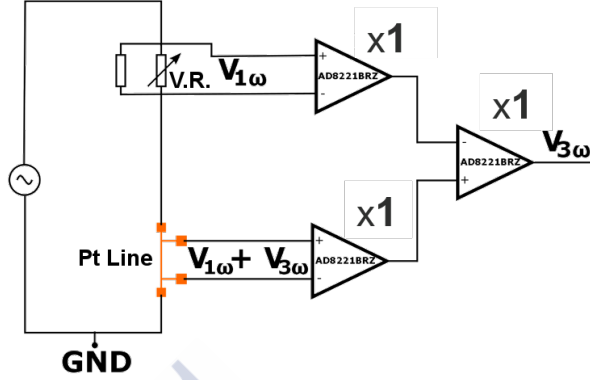
Figure 2.28: Schematic diagram of the setup developed in our lab and used during the thermal conductivity measurement, in order to obtain only the $V_{3\omega}$ component. The output signal from the Pt line contains both $V_{1\omega}$ and $V_{3\omega}$ components of the signal. Adjusting the variable resistance (V.R.), the $V_{1\omega}$ component can be eliminated through the three differential amplifiers (AD8221BRZ). [116]

Both voltages $V_{1\omega}$ and $V_{3\omega}$ are monitored through a lock-in amplifier (Stanford Research Systems SR810/SR830). In order to measure only the $V_{3\omega}$ voltage, we implement the setup described in Figure 2.28, which permits the elimination of the $V_{1\omega}$ voltage. The in-phase component ($Re[V_{3\omega}]$) of the $V_{3\omega}$ shows a linear region in a $V_{3\omega}$ vs $ln(2\omega)$ plot, while the out-of-phase ($Im[V_{3\omega}]$) remains constant (see Fig. 2.29).
Using the expression

$$V_{3\omega} = \frac{V_{1\omega} I^2 R(\frac{dR}{dT})}{4Rl\pi\kappa} ln(2\omega) \tag{2.24}$$

and fitting the experimental data, we can calculate the thermal conductivity of the substrate. Here we have to remark that the aforementioned linear region of the in-phase component of the $V_{3\omega}$ also depends on the power per unit length applied to the Pt strip to produce the heating of the sample. Therefore in every measurement taken, we have optimized the power. In order to determine the
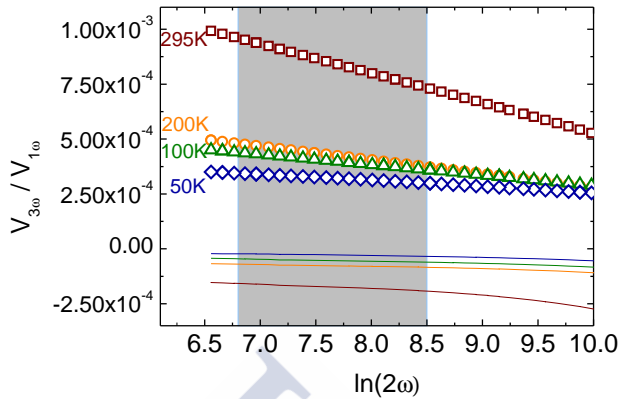
Figure 2.29: Representation of the in-phase components ($Re[V_{3\omega}]$ - open symbols) and out-of phase ($Im[V_{3\omega}]$ - solid lines) of the $V_{3\omega}$ for various temperatures for an LAO substrate. The light gray area indicates the linear region (76 - 362 Hz) where the out-of-phase component of the $V_{3\omega}$ is constant and the linear fit is made to obtain the thermal conductivity.

temperature coefficient (dR/dT) of the Pt resistance, we previously record the resistance values in a range of $\pm 10K$ around the base temperature of the measurement and we use the slope of these data.

In order to determine the thermal conductivity of the film it is necessary to measure both the thin film on top of the substrate, as well as the bare substrate at the same time. Therefore, during the deposition of the thin film inside the PLD chamber half of the substrate is covered by a metallic mask so that the deposited film occupies half of the substrate. Subsequently we evaporate two Pt strips one on the bare substrate and one on the part of the thin film (see Fig. 2.30).

The thin film behaves as a simple thermal resistance and adds a frequency-independent temperature oscillation to the substrate. Therefore, by measuring both the bare substrate and the film at the same time, we can extract the temperature oscillation of only the film by subtracting $\Delta T_f = \Delta T_{tot} - \Delta T_{sub}$ (see Fig. 2.31). The resulting thermal conductivity of the film can, then, be calculated
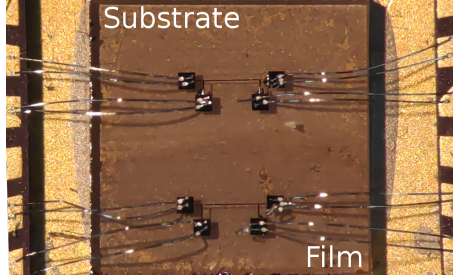
Figure 2.30: Photograph of the actual sample with the electrical connections to the sample holder.
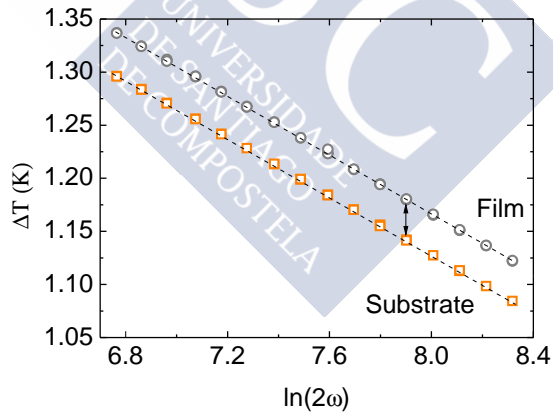
Figure 2.31: Representation of the ΔT of a CTO thin film ($t_f = 104$ nm - $PO_2 = 10^{-6}$ Torr) on top of an LAO substrate (open circles) and the substrate (open squares). From the difference between the two, it is possible to extract the thermal conductivity of the film, as described in Eq. 2.25.

by the following expression:

$$\kappa_f = \frac{I^2 R t}{\Delta T_f l w} \qquad (2.25)$$

The typical uncertainty for this method is $\approx 10\%$ and it is mostly due to the uncertainties introduced by the measurement of the thin-film, rather that measuring the substrate. Compared to the FDTR method described in the previous section, the 3ω method is simpler. However it has other serious limitations, like the impossibility of measuring electrical conductors (due to leaking of the current through the Pt line), or the limitation to the situation in which the thermal conductivity of the substrate must be at least ≈ 5 times larger than the thermal conductivity of the film.

As it is going to be discussed later in this work, there is a very good agreement between the results of κ measured by FTDR and the 3ω method.

Results and discussion

Chapter 3

Electron degeneracy and intrinsic magnetic properties of epitaxial Nb:SrTiO$_3$ thin films controlled by defects

3.1 Introduction

As it was discussed in the first chapter of this thesis, STO presents numerous unexpected properties; for instance, its interface with LAO or its bare surface under vacuum can become highly conductive, magnetic and present improved thermoelectric efficiency, among others. [117, 62, 7] We have reviewed the different mechanisms proposed to explain this type of behavior, although no consensus has been reached about their origin yet. Nevertheless, many of the interesting properties of the STO emerge in a *modified* state from its pristine condition, such as incorporated defects, epitaxial strain, reduced dimensionality, etc. Starting from this point of view, we are going to focus on the properties of STO thin films as a standalone system, in order to explore the possibilities of reproducing some of the phenomenology observed at the LAO/STO interfaces and study the mechanisms that provoke this type of phenomena.

We will study Nb-doped STO thin films and how the deliberate incorporation of point defects and the application of epitaxial strain can modify its structural properties. We have chosen to integrate a small amount of Nb ($\approx 2\ at\%$) so that the sample could be electrically conducting, in order to perform the transport properties characterization and study the further effect of the anionic (electron donors) and cationic (electron acceptors) defects. We then discuss how the induced structural modifications influence the magnetotransport and thermoelectric properties. We will formulate a conclusion about the origin of a magnetic phase and a low temperature minimum in the resistivity of the samples, similar to what has been reported in STO/LAO interfaces.
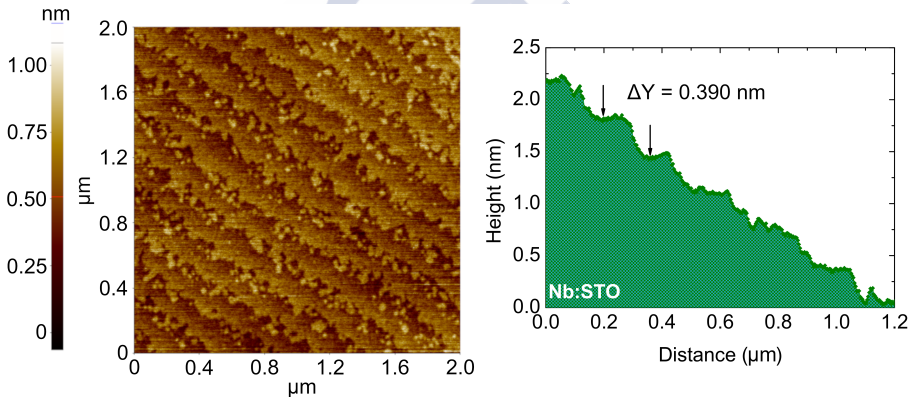
Figure 3.1: Left: AFM image of the surface topography of a 50 nm thick Nb:STO film deposited on top of an STO substrate at $PO_2 = 0.01$ Torr. Right: Graphic representation of the terraces of the Nb:STO film, where the height difference is $\Delta Y \approx 3.905$Å.

3.2 Experimental details

Epitaxial thin films of Nb-doped SrTiO$_3$ (Nb:STO) were grown by PLD (KrF, $\lambda = 248$ nm, laser fluence 0.9 J/cm^2, 5 Hz, at 800 °C) on top of (001) TiO$_2$-terminated STO (a = 3.905 Å), and (001) LSAT (a = 3.87Å) substrates. Different films were fabricated at different

oxygen pressures, in a range from 10^{-5} to 0.2 Torr. After the deposition, the samples were cooled at the same oxygen pressure. The conditions were optimized to obtain layer-by-layer growth, even in films as thick as $\approx$ 50 nm, with high quality interfaces (see Fig. 3.1).

3.3 Results and discussion

Growing stoichiometric films of STO by PLD is only possible in a very narrow range of laser fluence, oxygen pressure and temperature. [118, 119, 120, 121, 97, 98, 122] Away from this window, the samples always present a varying amount of cationic and anionic vacancies, which produce a substantial enlargement of the unit cell. [118] During this study, all the relative deposition parameters were held constant, except for the PO_2, which will be regarded as a means of *tuning* of the composition of the films.
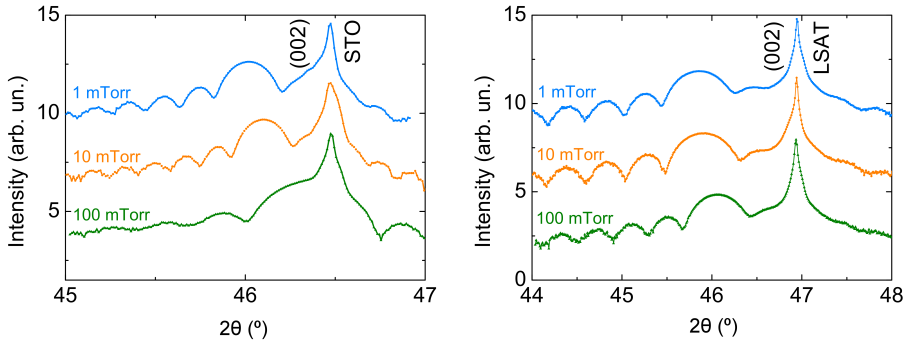
Figure 3.2: XRD patterns of 25(1) nm thick Nb:STO films grown on (001) STO [left] and LSAT [right], at different PO_2.

In Figure 3.2 are represented the XRD patterns for three films deposited at different PO_2, where we can observe the (002) Bragg peak of the film moving towards lower angles of 2θ, which translates to an expansion of the out of-plane lattice parameter of the film (c-axis), as the PO_2 decreases. The same effect is observed for films deposited on both substrates of STO and LSAT. This c-axis

expansion has been related to both cationic (V_{Sr}, V_{Ti}) and anionic (V_O) vacancies in previous studies. [118, 123, 124]

In the case of V_O, the *chemical expansion* phenomenon can occur, in which the crystal lattice expands as a result of the fact that the two electrons donated by the V_O, are located in non-bonding orbitals. [125] This phenomenon is usually more pronounced in oxide perovskites with transition metals, which have the versatility to adapt in various valence states. [126] However, post-annealing of the films in oxygen resulted in a negligible variation of the lattice parameter (see Fig. 3.3). Therefore, V_O can be ruled out as the main source of this expansion.

Other possible sources of expansion could be the formation of defects due to bombardment of the film with highly energetic ions during deposition, [127, 128] or the presence of cationic vacancies. [126, 129, 97, 122] Since the ionic radii of the cations in the perovskite structure are much larger than the one of the oxygen ions, the modification in the bond lengths, and thus, of the lattice expansion, is expected to be more pronounced after the formation of cationic vacancies. In the range of laser fluence and oxygen pressures used in this work, Sr vacancies (V_{Sr}) are energetically favored over V_{Ti}. [120]
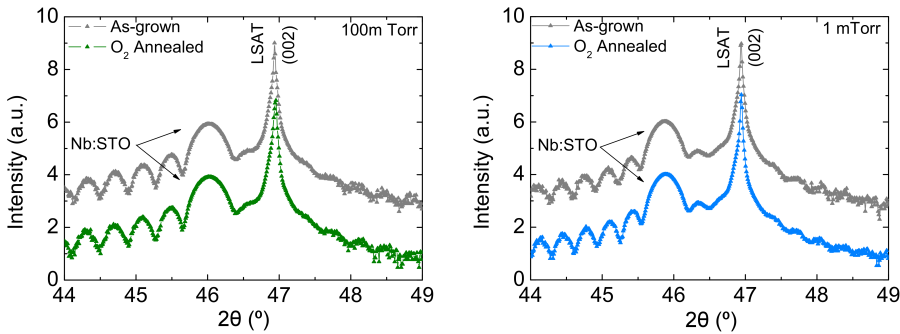
Figure 3.3: XRD patterns for the samples as-deposited and post annealed in oxygen. The samples were grown on LSAT at $PO_2 = 100$ mTorr [left] and 1 mTorr [right] and annealed at $PO_2 = 1$ mTorr and 100 mTorr, respectively. The effect of oxygen annealing over the lattice parameters is negligible.

We performed XPS analysis to determine the stoichiometry of our samples, and confirmed an increasing amount of Sr vacancies as oxygen pressure decreases (see Fig. 3.4). Within the resolution of our analysis, the samples grown at 100-200 mTorr are nearly stoichiometric, and the amount of V_{Sr} increases to $\approx$ 5-7% at lower pressures. The analysis also confirms the equal amount of Nb ($\approx$1.8(1)%) in all samples.

Therefore, although the presence of V_O is expected to be increasingly important as the oxygen pressure decreases, we conclude that the major contribution to the lattice expansion in the whole pressure range is due to doubly charged V_{Sr}. [130]
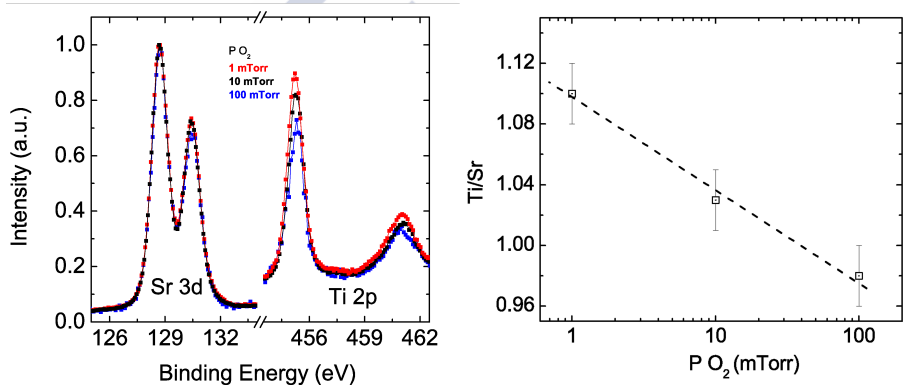
Figure 3.4: XPS spectra for various films. The background was subtracted for each spectra. The data has been normalized to the Sr 3d peak, to make evident the increase of the Ti/Sr ratio as the oxygen pressure decreases. The sample at 100 mTorr is stoichiometric within the error of the measurements.

In addition to this out of-plane lattice expansion, our study adds some important findings to previous works: X-ray analysis shows that the epitaxial films grow fully strained at all pressures (see Fig. 3.5) on top of both substrates, exhibiting high crystalline quality and sharp interfaces (see Fig. 3.5 and 3.6).

High Angle Annular Dark Field- Scanning Transmission Electron Microscopy and Geometrical Phase Analysis (HAADF-STEM and GPA) show that the expansion of the c-axis parameter is homogeneous along the film thickness, even for 50 nm thick films (see Fig.
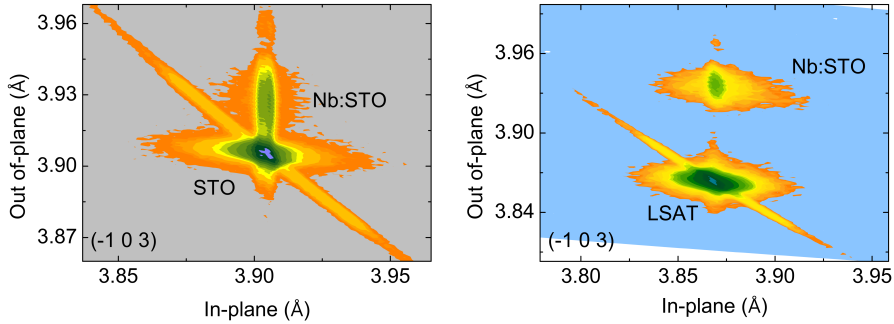
Figure 3.5: High resolution RSM around the (-103) reflection on STO substrate [left] for one film deposited at 1 mTorr and on top of LSAT substrate [right] for one film deposited at 100 mTorr.

3.6h), not influenced by the presence of clustered defects. Therefore, it can be concluded that there is a homogeneous tetragonal distortion of the unit cell as the oxygen pressure is decreased. It is very interesting that a small concentration of cationic vacancies is able to produce a homogeneous tetragonal distortion of the whole film, as shown in Figure 3.6, instead of a local expansion around each defect.

This distortion can be quantified by $\Delta t = (c_f - a_s) \times 100 / a_s$, where f, and s stand for film and substrate, respectively. The analysis of the structural and microstructural data shows a different volume for the films grown on STO and LSAT (see Fig. 3.7 [left]), demonstrating a dependence of the unit-cell expansion on the epitaxial stress. Although growing Nb:STO on LSAT introduces a moderately compressive stress ($\approx 0.9\%$), the continuous increase of the c-axis parameter with decreasing oxygen pressure is totally unexpected, on the basis of Poisson's effect in a stoichiometric system. [131, 132]

Although the role of the V_O seems to be trivial on the structural properties of the films so far, it is really significant when it comes to the transport properties of the films, especially at low PO_2. This increasing influence of oxygen vacancies can be further studied by Hall effect in the whole PO_2 range , given the different nature of V_{Sr}
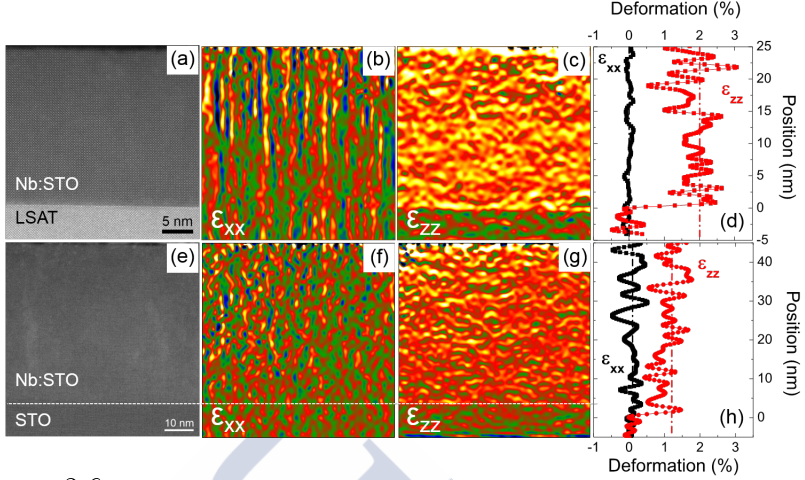
Figure 3.6: HAADF-STEM image of Nb:STO thin films deposited on STO (bottom) and LSAT (top). GPA analysis showing the in-plane ε_{xx} and out of plane ε_{zz} elongation, with respect to the substrate. A profile along the film thickness is shown in panels d) and h). The analysis indicates a total tetragonal distortion $\Delta t \approx 1.5\%$ for STO and $\approx 2.5\%$ for LSAT.
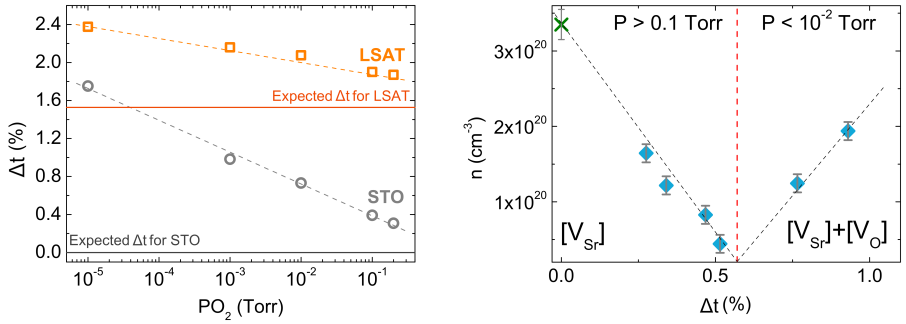
Figure 3.7: Left: Pressure dependence of the tetragonal distortion for thin films deposited on STO and LSAT (open symbols). The solid lines represent the value of tetragonal distortion calculated for Poisson ratio of $\nu = 0.23$. The dashed lines are guide to the eye. Right: Room temperature carrier density as a function of the tetragonal distortion, determined by Hall effect measurements for samples deposited on STO. The cross represents the theoretical value expected for the nominal Nb-doping. The dashed lines are guide to the eye.

(e-acceptor), [133] and V_O (e-donor) over the total charge density.

The electronic density determined by Hall measurements at room temperature is shown in Figure 3.7 [right] for a series of films deposited on STO. The measured charge density shows two distinct regimes as a function of Δt: for samples grown at high oxygen pressure, the carrier density decreases continuously from the expected nominal value, reflecting the increasing presence of electron-trapping defects. Besides, growing samples below $\approx$ 10 mTorr results in an increase of the carrier density, showing the important contribution of oxygen vacancies to the electronic transport below this pressure range.

Therefore, there is a continuous change in the nature of vacancies as a function of the oxygen pressure. However, while they show an opposite contribution to the electrical conductivity, only V_{Sr} produce a significant contribution to the tetragonal distortion of the lattice.

Nevertheless, the presence of the V_O in a system can result into unexpected properties, as it was extensively discussed in section 1.1 of the introductory chapter. Actually, in regard with the electronic band structure of the STO, a change from one- to two-carrier transport has been suggested at a universal critical density in LAO/STO interfaces. [134, 135] Particularly, due to the contribution of lower mobility carriers at large fields, this could result in a non-linear contribution to the Hall effect at low temperatures.

The Hall data at various temperatures is shown in Figure 3.8 [left] for one of our films with Δt = 0.68%. At low temperature there is a clear deviation from the low-field linear behavior, similar to observations in LAO/STO interfaces. [135, 134] This behavior is observed up to a given temperature T*, which marks a minimum in the temperature dependence of the resistivity. An upturn and saturation in the low temperature resistivity as shown in Figure 3.8 [right], was previously reported in electrolyte-gated STO, associated to Kondo effect. [136, 137] The Kondo effect could be described as the interplay between the mobile charge carriers and localized Ti^{3+} magnetic moments.

In order to examine the possibility of the existence of the Kondo
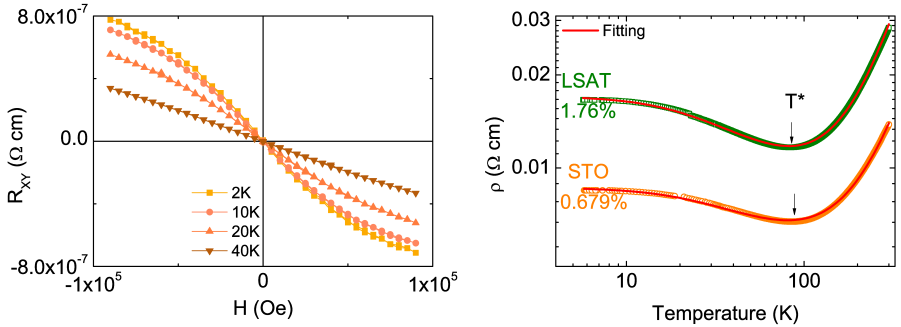
Figure 3.8: Left: Hall resistivity at different temperatures. The non-linear behavior at high field disappears above T*. Right: The resistivity for two samples grown at the same oxygen pressure on different substrates, indicating the T* and the corresponding Δt. The solid line represents the fitting to the Kondo equation (see Eq. 3.2).

effect in our film, we have performed a similar fitting for the resistivity curves of our samples, using the model proposed by Lee *et al.* [136] as can be seen in Figure 3.9 [right]. According to the authors, the resistance, above and below its minimum, can be described by a Kondo model

$$R^{fit} = R_0 + qT^2 + pT^5 + R_K\left(T/T_K\right) \tag{3.1}$$

where T_K is defined as the temperature at which the Kondo resistivity is half relative to its zero-temperature value, R_0 is the residual resistance due to sample disorder, and the T^2 and T^5 terms represent the functional temperature dependence of the electron-electron and the electron-phonon interactions, respectively. For the numerical fitting of this model to the data, an empirical form for the universal resistivity function was used

$$R_K\left(T/T_K\right) = R_K(T = 0)\left(\frac{T_K'^2}{T^2 + T_K'^2}\right)^s \tag{3.2}$$

where $T_K' = T_K/\left(2^{1/s} - 1\right)^{1/2}$, and s was fixed as $s = 0.225$. The numerical fit to our data, using Eqs. 3.1 and 3.2, yielded $R_0 = 30.5\Omega, p = 0.005\Omega/K^2, q \approx 0, R_K(0K) = 135\Omega$, and $T_K = 254K$,

89

for the case of Nb:STO film on top of STO substrate. In the case of the film grown on top of an LSAT substrate, the fitting yields, $R_0 = 222\Omega, p = 0.02\Omega/K^2, q \approx 0, R_K(0K) = 1273\Omega$, and $T_K = 92K$.

Even though the fitting of the proposed model to our data was successful, the first hint that this could not be the case resides in the T_K values. Normally the critical temperature where the Kondo effect is significant are much lower that the ones obtained here. Moreover, as shown in Figure 3.9 [right], T* increases linearly with Δt, showing that the change in the conduction mechanism at low temperature is determined by the total concentration of defects.

In addition, the resistivity of the samples increases as the tetragonal distortion (and the defect concentration) increases (see Fig. 3.9 and further discussion). This, along with the absence of any anomaly in the Seebeck coefficient at the Kondo temperature (see Fig. 3.13), suggests that in this case, the transition to a thermally activated behavior observed below T* is most probably due to conventional vacancy scattering, and not to Kondo effect.
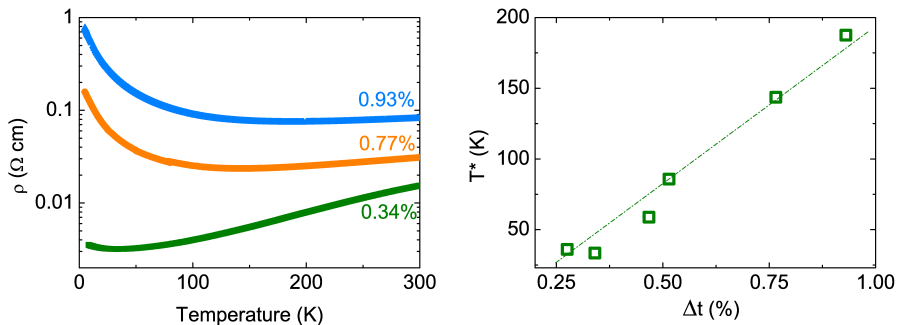
Figure 3.9: Left: Temperature dependence of the resistivity of Nb:STO thin films deposited on STO substrates at different PO_2 (resulting in different tetragonal distortion). Right: Variation of T*, as a function of the tetragonal distortion Δt.

On the other hand, a non-linear Hall effect could be due to an anomalous contribution from a magnetically ordered phase. [138] In fact, the presence of localized magnetic moments and magnetic

order in doped STO and LAO/STO interfaces is a controversial issue, whose origin is still under discussion. [117, 139, 140, 141]

An important test for the presence of localized magnetic moments and spontaneous magnetic ordering will come from the study of the anisotropic magnetoresistance (AMR). Below T*, the transverse MR (H in plane, perpendicular to the current, see Fig. 3.10 [left]) is positive at low field, and it turns to negative at ≈ 5 T. This behavior is identical to that been reported for an STO quantum well embedded in antiferromagnetic $SmTiO_3$. [4] Their results are depicted in Figure 3.10 [right].

According to Jackson *et al.*, this type of MR is attributed to the proximity effect induced by the antiferromagnetic ordering of the $SmTiO_3$ matrix. They have reported that the magnitude of the positive MR depends directly on the thickness of the quantum well of the STO and it disappears after 3 layers of SrO. The authors suggested that the antiferromagnetism could be the reason for this positive mangetoresistence, but its origin is still in dispute. On the other hand, the negative magnetoresistance is attributed to the suppression of the spin fluctuations with the increasing magnetic field.
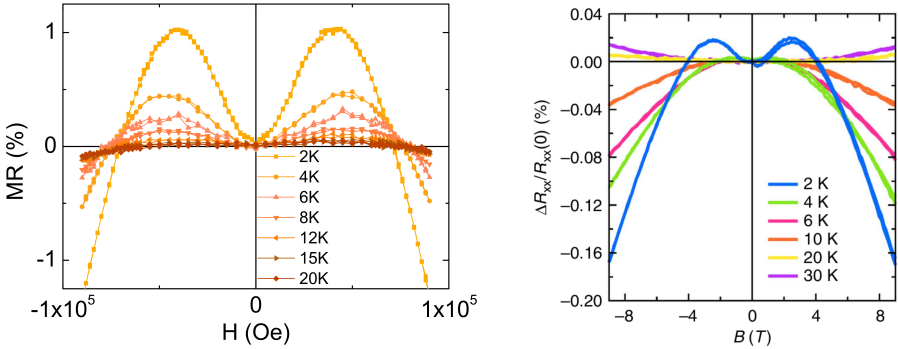
Figure 3.10: Left: Magnetoresistance, for a 50 nm thick film deposited on STO at 10 mTorr ($\Delta t \approx 0.68\%$) for various temperatures. The magnetic field is applied in the plane of the film, perpendicular to the current. Right: Temperature dependence of the magnetoresistance of $SmTiO_3/STO/SmTiO_3$ quantum well. Reprint from [4]

In addition, measuring the perpendicular MR (H out of plane, see Fig. 3.11 [left]), we find out that is a non-monotonically-decreasing function of H. This behavior was also observed in previous report by Brinkman *et al.*, [117] (see Fig. 3.11 [right]) while studying the LAO/STO interface. According to the authors, this behavior is attributed to spin scattering of the conduction electrons off magnetic moments that reside at the interface, stemming from the proposed polar discontinuity. Moreover, this behavior is in principle compatible with a 2D weak anti-localization (WAL) contribution to the magnetoresistance in the presence of a strong spin-orbit coupling. [142] Nevertheless, we have observed this behavior in 50 nm thick, highly distorted films which should rule out the 2D WAL scenario.
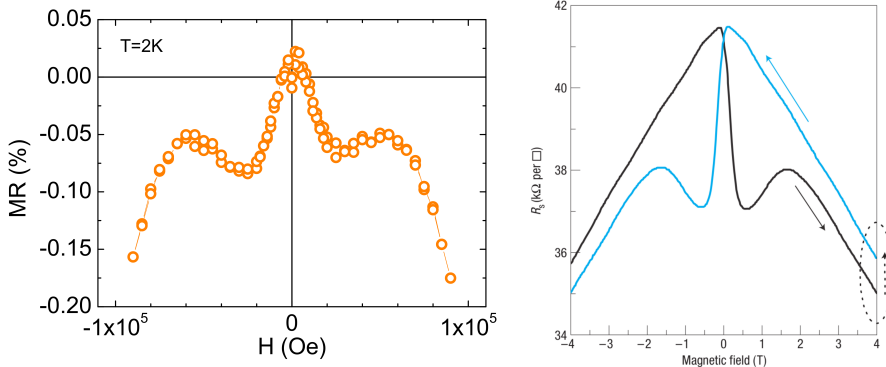
Figure 3.11: Left: Magnetoresistance measured at 2 K for a 50 nm thick film deposited on STO at 10 mTorr (Δt$\approx$ 0.68%). The magnetic field is applied perpendicular to the surface of the film. Right: Magnetoresistance of an *n-type* LAO/STO interface. Reprint from [117]

Additionally to the similar phenomenology that we have observed in the in- and out-of-plane MR in our film, the MR in our film exhibits anisotropic behavior when the magnetic field is rotated from in-plane to out of-plane (see Fig. 3.12) relative to the film's surface. This kind of anisotropy suggests that the source of this spin-orbit scattering is a magnetic phase, rather than independent magnetic moments (isotropic) at Ti^{3+} sites, which was the possible

mechanisms proposed in the two previous examples. Therefore, the main findings of non-linear Hall effect, and AMR (in/out of plane) observed in LAO/STO interfaces, can be also reproduced in thin films of STO under different degrees of strain and concentrations of cationic and anionic vacancies.
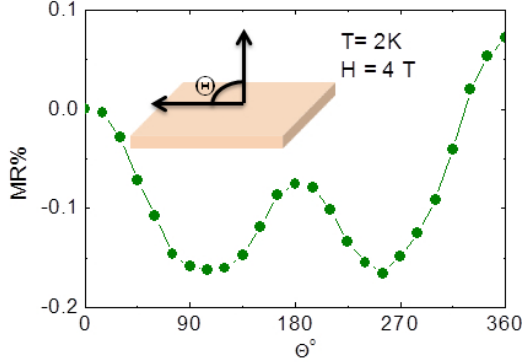
Figure 3.12: Angular dependency of the out of-plane magnetoresistance.

Moreover, although Fe impurities are normally associated to Ti, the fact that the MR is observed below a minimum which depends on strain and not only on the composition of the films, makes highly improbable that the AMR effect is related to the presence of magnetic Fe impurities in the films.

Apart from the influence of the V_O in the transport properties of the films, the change in the crystal structure of the material caused mainly by the cationic defects, is expected to impact its electronic band structure. The band structure and its occupation can be tested experimentally from the temperature dependence of the Seebeck coefficient, for samples under different degree of distortion. Given the band structure of STO, a good approximation for the thermoelectric power of carriers at the bottom of its conduction band could be derived from the Boltzmann equation for a parabolic band (z-fold degenerate; see also Section 1.3.1): [143]

$$S = \left(\frac{k_B}{e}\right)[-y + \delta_r(y)] \tag{3.3}$$

$$\delta_r(y) = \frac{(r+2)F_{r+1}(y)}{(r+1)F_r(y)} \qquad (3.4)$$

where $y = (\mu/k_B T)$ is the reduced chemical potential, r is the scattering parameter for the energy-dependent relaxation time, $\tau(E) = \tau_0 E^r$, which for charged impurities can be taken to be $3/2$, [70, 143, 40] and F_r is the Fermi integral. Using the experimental values of the charge density measured by Hall effect, average $m^* = 1.5 m_e$, from Shubnikov-de Haas [144, 142] and the following relation to calculate the chemical potential:

$$n = z \left(\frac{2\pi m^* k_B T}{h^2} \right)^{\frac{3}{2}} \frac{2}{\sqrt{\pi}} F_{\frac{1}{2}}(y) \qquad (3.5)$$
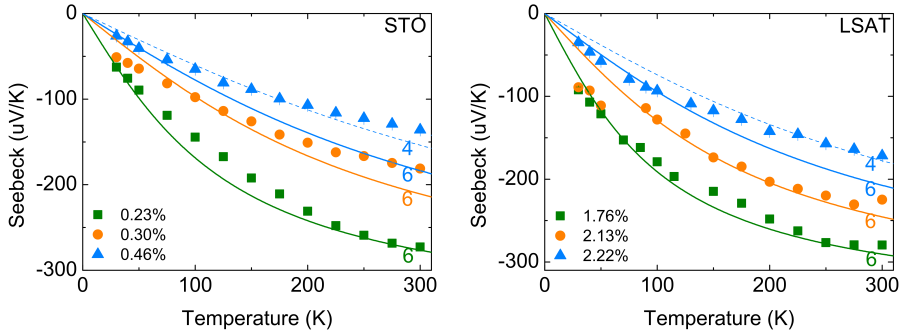
Figure 3.13: Temperature dependence of the Seebeck coefficient for thin films deposited on STO [left] and LSAT [right], for different Δt. The lines are calculations from equation 3.3.

the thermoelectric power can be calculated from Eq. 3.5, taking the band degeneracy z as the only adjustable parameter. The results of the calculation (lines) are shown in Figure 3.13, along with the experimental data (closed symbols). There is a very good agreement between the calculation and the experimental data. But it is also clear from these plots that films with larger Δt, fit better to the curves with $z = 4$, in both STO and LSAT, while the films grown at higher PO$_2$ (Δt small), fit better to the z=6 curve.

These results demonstrate the significant effect of the structural modification to the thermoelectric properties of the films. Since the Seebeck coefficient is sensitive to the electronic band structure and degeneracy, as well as the charge carrier density, it is crucial, for potential thermoelectric applications, to be able to control these parameters during the deposition process of the films.

Density functional theory-based calculations [145, 146] on bulk STO under various degrees of tetragonal distortion $\Delta t \approx$0-3% (allowing for octahedral rotations) were performed by Prof. Victor Pardo at the Applied Physics department of the University of Santiago de Compostela (USC).

Spin-orbit coupling splits the t_{2g} states (effectively an l=-1 triplet) [147] at the Γ-point, into a low-lying doublet and an upper lying singlet (see Fig. 3.14 where the band structure for $\Delta t = 2\%$ is shown) and the tetragonal distortion splits the doublet.
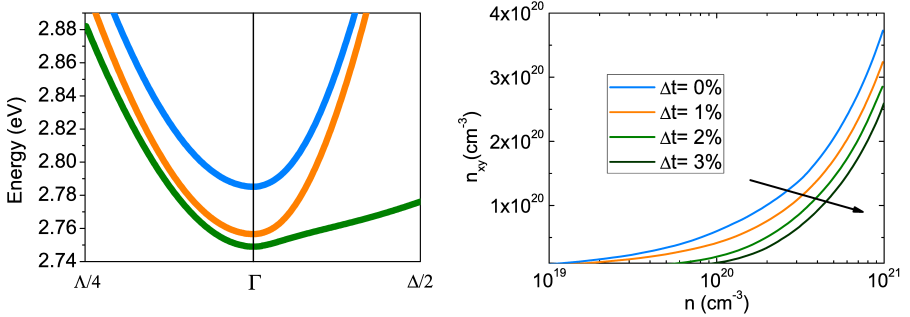
Figure 3.14: Left: Band structure of bulk STO under a tetragonal distortion Δt= 2% with the upper band split by spin-orbit coupling calculated ab-initio. The low-lying doublet is split as a result of the tetragonal distortion. Right: Total number of electrons with d_{xy} symmetry as a function of the total number of d electrons, which decreases as the tetragonal distortion increases.

The calculation showed that the on-site energy of the d_{xy} electrons increases with Δt, as they are relatively destabilized by the octahedral elongation with respect to the $d_{xz,yz}$. Therefore, a reduction of the relative weight of the xy electrons is anticipated from the calculations as Δt and n increase, thus reducing the overall

electron degeneracy inside the t_{2g} manifold. This trend is observed in Figure 3.14, in the range of doping relevant for comparison with our experiments.

Therefore, thermoelectric power and ab-initio calculations support a scenario in which an additional band splitting is produced in Nb:STO due to the presence of V_{Sr}, whose amount is extremely sensitive to deposition conditions. Moving the Fermi energy across these bands will change the relative contribution from heavy/light electrons to the transport properties of the system. Actually, a change from one- to two-carrier transport has been suggested at a universal critical density in LAO/STO interfaces. [134, 135] Our results demonstrate that this is an intrinsic property of STO, under certain conditions of strain and doping.

3.4   Summary and conclusions

To summarize, we synthesized Nb:STO thin films of high crystalline quality and sharp interfaces, whether under in-plane compressive strain or unstrained. By tuning the PO_2 during the deposition process, we were able to provoke a homogeneous tetragonal distortion throughout the whole thickness of the films, mainly due to the creation of cationic vacancies. This tetragonal distortion combined with the increasing influence of oxygen vacancies at lower oxygen pressures dictates the properties of our films, revealing many interesting behaviors, previously observed in systems based on LAO/STO interfaces.

The resistivity of our samples exhibits a minimum and a low temperature saturation, which depends on the degree of the induced tetragonal distortion and thus to the concentration of defects, even though previous similar results in LAO/STO interfaces and gated-STO associated the behavior to Kondo effect. The absence of any anomaly at T* in the S(t) makes this scenario improbable. Moreover, we have observed anomalous Hall effect and the appearance of magnetoresistance, similar to results for LAO/STO interface and

$SmTiO_3/STO/SmTiO_3$ quantum wells, where the behavior was associated with localized magnetic moments at the polar interface, or with proximity effects due to the antiferromagnetic $SmTiO_3$. Nevertheless, the existence of an anisotropy in the MR of our samples, points towards the existence of an intrinsic ordered magnetic phase in defective STO thin films.

Moreover, we have demonstrated, through experiment and ab-initio calculation, that by controlling the degree of the tetragonal distortion in our films, we were able to control the electronic band structure and its occupancy of our films. This has a significant effect on the thermoelectric power and it could suggest new ways of taking advantage of defects and strain for the improvement of the thermoelectric efficiency in perovskite oxides.
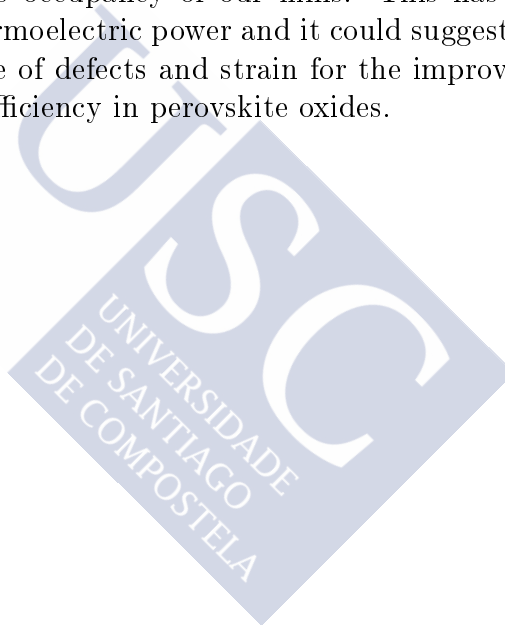
Chapter 4

Influence of ferroelectric domain walls in the thermal conductivity of SrTiO$_3$ thin films

4.1 Introduction

In this chapter we present the analysis of the effect of strain on the thermal conductivity of SrTiO$_3$ thin films. STO is an incipient ferroelectric material, owed to the suppression of ferroelectric transition by a preceding antiferrodistortive (structural) transition. [5] This quantum paraelectric state of STO can be modified by mechanical stress, [148] impurity doping, [149, 150] and Sr non-stoichiometry, [151] among other mechanisms, leading to a stable ferroelectric state or relaxor ferroelectric behavior. As we will demonstrate in this chapter, this phase transition could play a significant role in therms of thermal transport in STO thin films.

Ferroelastic domain walls are natural interfaces occurring within most ferroelectric materials. In the case of BiFeO$_3$ or Pb(Zr,Ti)O$_3$, these domain walls have been shown to be effective scattering centers for phonons, reducing considerably the thermal conductivity

of the material as the domain-wall density increases (see Fig. 4.1). [152, 153]
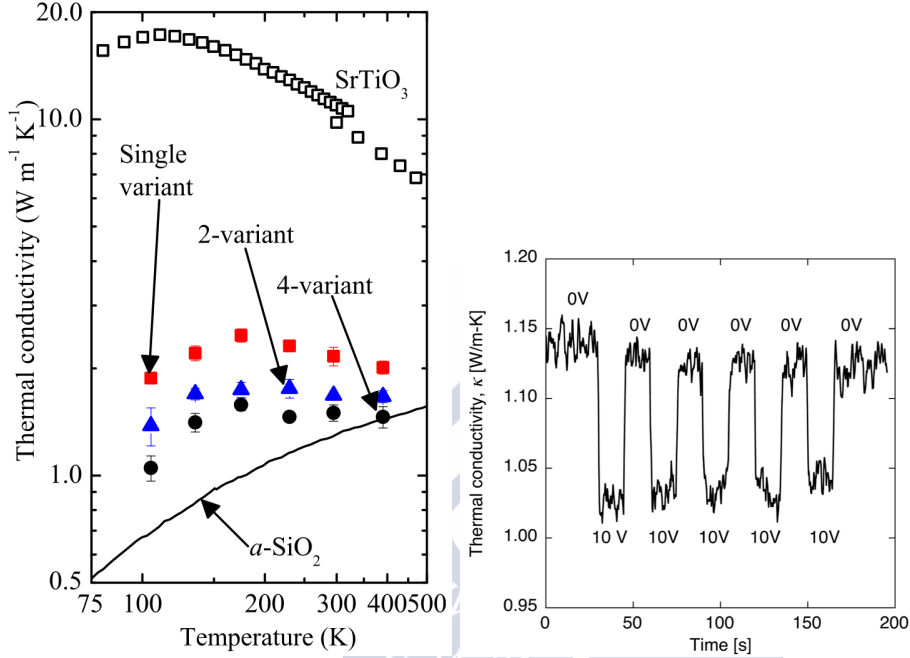
Figure 4.1: Left: Thermal conductivity of $BiFeO_3$ films (filled symbols), as a function of the temperature. The number of domains play a significant role in thermal transport due to phonon scattering in the localized strain field of the domain walls. The number of variants refer to the different types of domains in the samples. They correlate approximately with the density of domain walls. The data of bulk STO (open symbols) and amorphous Si (solid line) are plotted for comparison. Reprint from [152] Right: Real time change of the thermal conductivity of the $PbZr_{0.3}Ti_{0.7}O_3$ of a $Pb(Zr,Ti)O_3$ bilayer film at room temperature, showing the dynamic response of the thermal conductivity tuning effect of the domain wall density through the application of external electric field. Reprint from [153]

In the following, we present the results of thermal conductivity in films of $SrTiO_3$ under different degrees of epitaxial strain. The thin films were deposited on top of three different substrates, with negative (LSAT), zero (STO), and positive (DSO) in-plane epitaxial

strain. As we have discussed in the previous chapter, the structural modification that follows the incorporation of defects, as well as the epitaxial strain plays a significant role, not only the morphological aspect of the thin films, but also on their electronic structure and in the development of a ferroelectric polarization in SrTiO$_3$.

We will discuss the role played by ferroelectricity and domain walls in the large differences observed in the $\kappa(T)$ of STO under different degrees of strain. Finding new ways to reduce the thermal conductivity of STO, which is already considered a potential thermoelectric material, is crucial in the search of achieving acceptable values of ZT in this compound.

The strategy presented in this chapter is general, and can be used to control the thermal conductivity in other ferroelectric and multiferroic oxides.

4.2 Experimental details

Epitaxial thin films of SrTiO$_3$ were grown by PLD (KrF, $\lambda = 248$ nm, and Nd:YAG, $\lambda = 266$ nm, laser fluence 0.9 J/cm^2, 5 Hz, at 800 °C) on top of (001) TiO$_2$-terminated STO (a = 3.905 Å), (001) (LaAlO$_3$)$_{0.3}$(Sr$_2$AlTaO$_6$)$_{0.7}$ (LSAT, a = 3.87Å), and (110) orthorhombic DyScO$_3$ (DSO, a$_{pc}$ = 3.95Å) substrates. The oxygen pressure was varied from 10^{-3} to 0.1 Torr. After deposition the samples were cooled at 5 °C, under the same oxygen pressure. The conditions were optimized to obtain layer-by-layer growth, as has been described in Chapter 3. The thermal conductivity measurements were performed by the FDTR method, as described in section 2.4.1.

4.3 Results and discussion

As we have shown in the previous chapter (Chapter 3), STO thin films grow epitaxially on top of STO and LSAT substrates, regardless the PO$_2$ used during the deposition, exhibiting high quality in-

terfaces and crystalline structure. Likewise, growing the thin films on top of DSO, result in high quality thin films, fully strained to the lattice parameters of the substrate, as it is shown in Figure 4.2 [left]. Moreover, a full width at half maximum (FWHM) of 0.033°of the X-ray rocking curve around the (002) reflection demonstrates the high quality of the STO film grown on DSO (see Fig. 4.2 [right]).
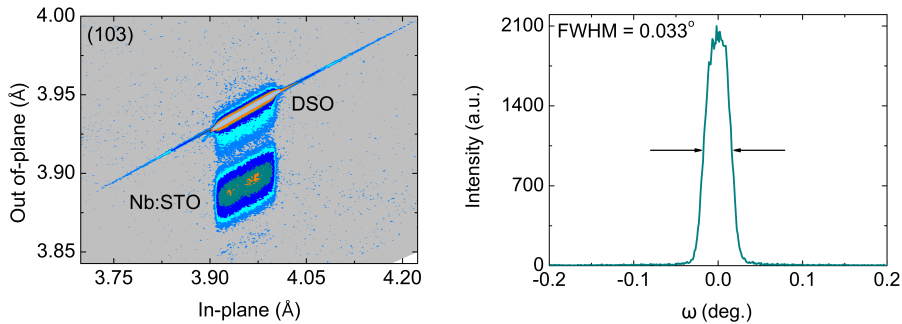
Figure 4.2: Left: High resolution RSM around the (103) asymmetric reflection of a 21 nm thick film of STO deposited on top of a (110) DSO substrate. The reciprocal lattice units were translated to real space lattice parameters for clarity. Right: Rocking curve of the same film, around the (002) reflection of the STO film. The value of the full width-half maximum (FWHM) was determined at 0.033°.

Growing the thin films on top of LSAT imposes an in-plane strain of the order of $\approx -0.9\%$ (compressive strain), while on top of DSO substrates, the in-plane strain is of the order of $\approx +1.15\%$ (tensile strain). Consequent with this, the X-ray diffraction pattern around the (002) peak shows an angular increment as the epitaxial compression decreases. The changes of the out of-plane lattice parameters of the thin films are in good agreement with calculations using a Poisson ratio $\nu = 0.23$, as shown in Figure 4.3 [right]. The slightly larger experimental values of the c-axis can be attributed to an additional elongation provoked by the incorporation of cation vacancies during growth, as it was discussed in Section 3.3.

On the other hand, apart from the epitaxial tension, growing the STO thin films on top of DSO induces a change of the rotation
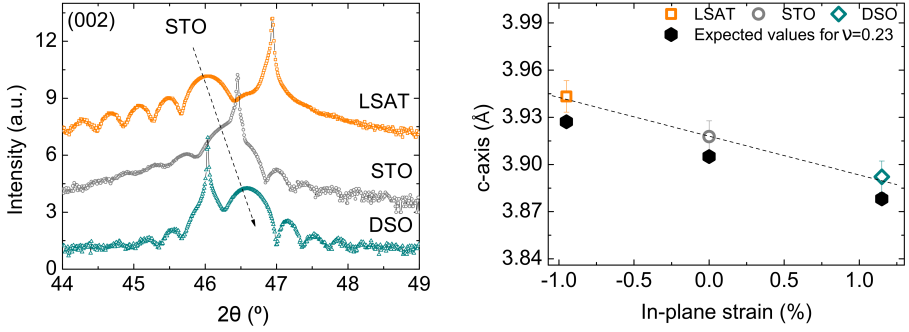
Figure 4.3: Left: XRD patterns of the STO thin films grown on top of LSAT, STO and DSO substrates at a PO$_2$ of 0.1 Torr. Right: Values of the c-axis parameter as a function of the in-plane strain imposed by each substrate. The black symbols correspond to the expected values of the c-axis calculated for STO with a Poisson ratio of $\nu = 0.23$. [131]

pattern of the TiO$_6$ octahedra, compared to those deposited on top of STO or LSAT substrates. As it was reported in our previous work, [154] STO thin films deposited on top of STO and LSAT substrates, present the pattern of $(a^+b^+c^0)$, while the thin films deposited on DSO substrates exhibit the $(a^+b^-c^-)$ or $(a^-b^+c^-)$ rotation pattern, which are compatible with a ferroelectric distortion, and could have significant effects on the properties of the thin films.

Several authors have discussed the possibility of stabilizing a FE distortion on STO thin films by applying epitaxial tensile strain. The antiferrodistortive (structural) transition that occurs in STO at around 105 K, from cubic to tetragonal, precedes and suppresses the ferroelectric instability in this material. [155] One way to avoid the suppression of the FE transition is applying a biaxial strain, which suppresses the structural phase transition. One of the first reports of this effect was by Uwe and Sakudo [148] in 1976, who observed the appearance of ferroelectric soft modes for large values of stress.

In 2004, Haeni *et al.* [156] reported the stabilization of FE phase on STO thin films at room temperature. Their calculations had predicted that the thin films deposited on DSO substrates
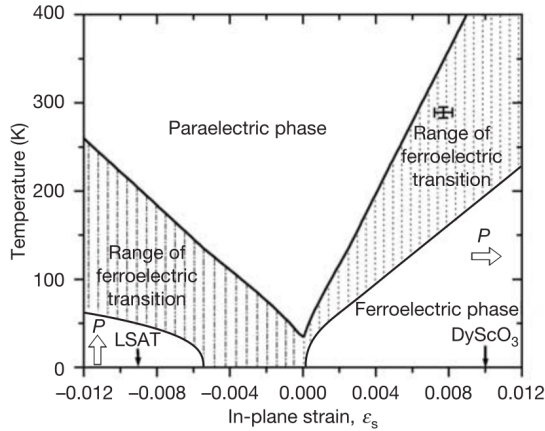
Figure 4.4: Phase diagram with the expected shift in T_C for (001) STO with biaxial in-plane strain, based on thermodynamic analysis. The white arrows indicate the expected direction of the polarization. The black arrows indicate the position of the LSAT and DSO substrates regarding the value of in-plane strain ϵ_s. Reprint from [156]

would exhibit a stable FE phase, with the polarization parallel to the surface of the film, while in the case on the film deposited on LSAT substrate, the polarization would be along the out of-plane axis, happening at a lower temperature (see Fig. 4.4). However, their own (and others) experiments showed that the FE state was suppressed on LSAT (in-plane compressive stress) as the structural transition still occurs at a temperature higher than the FE transition. [5, 157]

On the other hand, for positively strained films, the FE transition occurs in the temperature region of 290-300 K. Small off-stoichiometries lowers the transition to 230-260 K, and results in relaxor-ferroelectric behavior. [158]

In the following, we discuss the results of our study about the effect of the FE domains on the thermal conductivity of STO. For this, we measured the thermal conductivity at room temperature in thin films grown on top of LSAT, STO and DSO substrates. We extended the measurements down to $\approx$100 K for the case of STO on LSAT and DSO, to go across their expected T_C according to
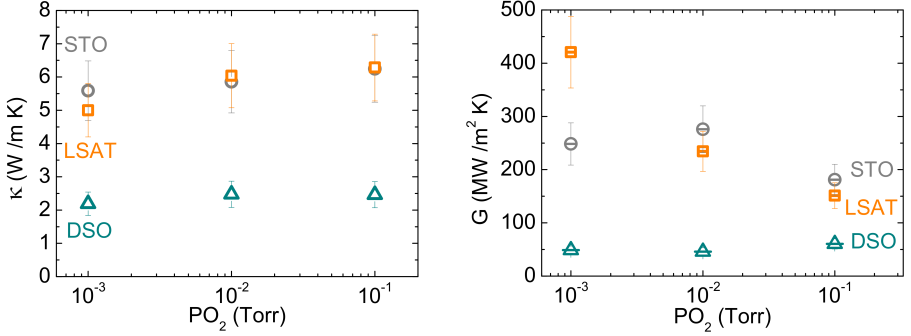
Figure 4.5: Left: Thermal conductivity of the STO thin films deposited on top of LSAT, STO and DSO substrates at $PO_2 = 10^{-1} - 10^{-3}$ Torr. Right: Interface thermal conductance (G) of the same thin films.

Figure 4.4.

In Figure 4.5 are presented the results for the room temperature thermal conductivity (and interface thermal conductance, G) of STO thin films deposited on LSAT, STO and DSO, using three different PO_2 during each deposition. The purpose of using different PO_2 was to introduce cationic/anionic defects, so their effect over κ can be studied and differentiated from any possible effect of a FE distortion. The thermal conductivities were measured by FDTR, as explained in Chapter 2.

Due to the reduced dimensions of the films, they have much lower thermal conductivities than bulk STO ($\kappa_{300K} = 11$ W /m K). [159, 160] For the films deposited on LSAT or STO, this reduction is $\approx 43\%$, but reaches $\approx 78\%$ for the samples deposited at DSO. Although point defects produce a significant decrease of κ in STO (see also the results by Oh *et al.* [161] and Breckenfeld *et al.* [162]), the concentration of defects in the present films is not enough to account for the dramatic reduction observed in STO on DSO. Both X-ray diffraction analysis (see Fig. 4.2) and TEM show a high quality crystalline structure for STO films deposited on DSO, which rules out a massive concentration of defects which could justify this reduction of κ.

On the other hand, the thermal conductivity of the films decreases as PO_2 decreases, due to the incorporation of a higher concentration of vacancies. However, even post-deposition annealing at 10^{-6} Torr in thin films on LSAT in order to induce a very high concentration of V_O, still keeps $\kappa \approx 4$ W/m K (see Fig. 4.6), which is about two times larger than the experimental values in STO on DSO.
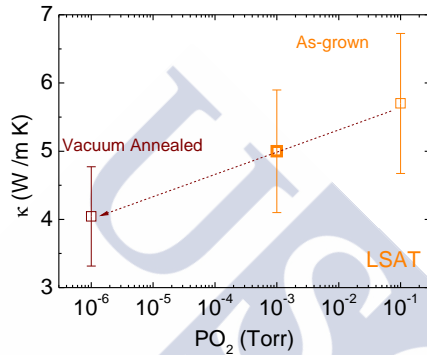
Figure 4.6: Thermal conductivity of STO thin films deposited on top of LSAT substrates. As-grown thin films deposited at $PO_2 = 10^{-1} - 10^{-3}$ Torr (orange symbols) and after ex-situ annealing at 10^{-6} Torr.

On the other hand, the change in volume due to epitaxial stress could have an effect on the thermal conductivity. The thermal conductivity is proportional to the cube of the Debye temperature (Eq. 1.47), and in the Debye approximation, the Grüneisen parameter can be expressed as the change in θ_D with the unit cell volume, $\gamma = -\frac{d \ln \theta_D}{d \ln V}$. Growing STO on LSAT produces a reduction of its unit cell volume of $\approx -1\%$. Taking $\gamma = 1.5$ [163] this change in the volume will result in an increase of $\approx 1.5\%$ of θ_D, and therefore $\approx 3.5\%$ increase of the thermal conductivity. In the case of the film on top of DSO, the relative change in volume is $\approx +2\%$, which would decrease θ_D by $\approx 3\%$, leading to an overall reduction of κ by $\approx 9\%$. However, the reduction of κ of STO on DSO is $\approx 60\%$ with respect to the value in STO or LSAT. Therefore, we conclude that the change in the volume cannot be responsible of the low κ

of STO on DSO.

The thermal conductance, G, also shows large differences between STO deposited on DSO with respect to STO and LSAT. The major factors that contribute to the interface thermal conductance G, are the Debye temperature mismatch across the different interfaces (between the Au/Cr transducer layer and the film, as well as between the film and the substrate) and the quality of each of the interfaces. The Debye temperature for STO is 690 K, for LSAT is 500 K and for DSO is 520 K, while for Au and Cr are 178 K and 424 K, respectively. Since the values for G are very similar for the films grown on top of STO and LSAT substrate, we can assume that the Debye temperature misalignment between the materials does not play the most significant role in this particular case. On the other hand, the surface roughness of the films is similar in every case, so the Au/Cr/film interfaces can be assumed to be also similar.

Therefore, the low values of G in the case of the films on DSO substrates must be interpreted in terms of structural quality of the STO/DSO interface. The major difference between the STO films grown on top of DSO and STO or LSAT is the large degree of the in-plane epitaxial strain, which modifies both the lattice parameters and the rotation pattern of the TiO_6 octahedra. Therefore we think the most plausible explanation for this strong reduction of G is the effect of tensile stress (and orthorhombicity of the substrate) on the rotation pattern of TiO_6 octahedra in the STO film.

In addition, as the PO_2 decreases, the values of G increase for the films deposited on LSAT and STO. This can be anticipated, since as the defect concentration is increased, possible interdiffusion at the interface between the films and the substrates blurs the abrupt interface, and helps the heat transfer across a more gradual interfacial barrier.

On the other hand, based on previous observation of FE at room temperature in STO films on DSO substrates, as well as on the reduction of κ by ferroelectric domain walls, [152] it is very appealing to associate the low κ of positively strained STO to phonon scattering by FE domain walls.

As in other perovskites, the ferroelectric transition in STO is expected to be of the soft-mode type. [164] This means that above T_C, there should be a certain unstable phonon mode (the "soft mode") whose frequency decreases (softens) as T_C is approached, becoming zero at the critical temperature. The corresponding vibration freezes at this temperature, resulting in a different structure, with different symmetry, and with a finite dipole moment. Nuzhnyy *et al.* [165] studied the temperature dependence of active phonon modes in STO by Fourier-transform infrared and time-domain terahertz spectroscopy. They found that there is a soft-mode driven ferroelectric transition below ≈ 280 K in STO on top of DSO, as well as an antiferrodistortive transition below ≈ 175 K.

Therefore, the temperature dependence of κ could provide further information about the effect of a FE phase in the reduction of the thermal conductivity observed at room temperature. Figure 4.7 shows the results for the thermal conductivity of STO thin films on DSO and LSAT substrates, as a function of temperature.
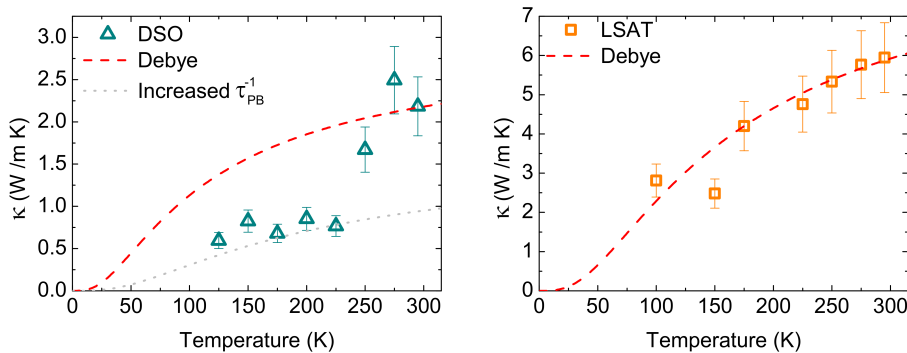
Figure 4.7: Temperature dependent thermal conductivity for STO thin films deposited on top of DSO [left] and LSAT [right] substrate at $PO_2 = 0.1$ Torr. The red dashed lines correspond to fittings according to the Debye model for the respective films. The gray dotted line corresponds to an increased boundary scattering term.

Below ≈ 275 K, there is a large decrease in $\kappa(T)$, of $\approx 60\%$ compared to the room temperature value. The thermal conductiv-

ity remains almost constant below 250 K, without any noticeable effect around the antiferrodistorsive transition temperature reported by Nuzhnyy *et al.*. [165]

Similar temperature dependent measurements for STO grown on an LSAT substrate, reveal a monotonic decrease with temperature, with only a small deviation around 150 K (see Fig. 4.7). This could also be the signature of a FE transtion (see Fig. 4.4), although, with only two points around this temperature, further studies should be performed to confirm this hypothesis.

As it was discussed in section 1.4.2, the lattice thermal conductivity in the Debye approximation is given by Eq. 1.45. The scattering term in that equation would be a sum of all the dominant scattering processes. We can rewrite Eq. 1.46, as a sum of the three dominant scattering processes for our study.

$$
\begin{aligned}
\tau_q^{-1}(x) &= \tau_{PB}^{-1} + \tau_U^{-1} + \tau_{PD}^{-1} \\
&= \frac{v}{d} + \frac{\hbar\gamma^2}{\overline{M}v^2\theta_D}\omega^2 T e^{-\frac{\theta_D}{3T}} + \frac{V}{4\pi v^3}\omega^4 \sum_i f_i (\frac{\overline{M} - m_i}{\overline{M}})^2
\end{aligned} \quad (4.1)
$$

The first term refers to the domain boundary scattering, the second to the *Umklapp* processes and the third includes the scattering processes caused by point defects, such as vacancies, impurities and isotopes.

Using the equations 1.45 and 4.1 it is possible to calculate an approximate temperature dependence for the thermal conductivity.

Fitting the model to the experimental data (see Fig. 4.7 [right]) in the case of the STO film on top of LSAT substrate, was straightforward. As input parameters, we have considered the Debye temperature of STO $\theta_D = 690$ K, the Grüneisen parameter $\gamma = 1.5$ and the sound velocity $v = 7900$ m/s, [163] $\overline{M} = 3.67 \times 10^{-2}$ kg/mol, and an estimated concentration of defects $V_O = 2.5\%$ and $V_{Sr} = 1\%$, since the thin films deposited at $PO_2 = 0.1$ Torr are nearly stoichiometric, as it was discussed in the previous chapter. The resulting scattering times were the following: $\tau_{PB}^{-1} = 7.05 \times 10^{11} s^{-1}$, $\tau_U^{-1} = 9.04 \times 10^{-20} s^{-1}$ and $\tau_{PD}^{-1} = 2.59 \times 10^{-43} s^{-1}$.

In the case of the STO film on the DSO substrate, the fitting to the Debye approximation was not so successful. For the initial fitting, the same values were used as in the case for the film on LSAT substrate, except for the concentration of defects, since a higher epitaxial strain is more likely to induce more vacancies to accommodate the lattice mismatch. As input parameters, the same values for θ_D, γ,v and $\overline{M}$ were used, while an estimated concentration of defects $V_O = 8\%$ and $V_{Sr} = 5\%$ was chosen. The obtained values for the scattering parameters were $\tau_{PB}^{-1} = 7.05 \times 10^{11} s^{-1}$, $\tau_U^{-1} = 9.04 \times 10^{-20} s^{-1}$ and $\tau_{PD}^{-1} = 1.2 \times 10^{-42} s^{-1}$ (red dashed line in Figure 4.7 [left]). In an attempt to approximate the increased boundary scattering form the FE domain walls, we have increased the boundary scattering term one order of magnitude (gray dotted line in Figure 4.7 [left]).

The model is unable to reproduce the abrupt reduction of κ below 275 K and the low temperature values. This is expected, since within the model we cannot take into account the appearance of a ferroelectric state. Nevertheless, increasing the boundary scattering term by an order of magnitude, we could approximate the almost constant lower temperature values, which could serve as an indicator that indeed the thermal conductivity reduction could be a result of increased boundary scattering from FE domain walls.

Therefore, we conclude that the stabilization of a FE state in STO on DSO is responsible for its low thermal conductivity. The low value already at room temperature indicates that the transition region is very broad and extends probably beyond 300 K. Reducing temperature below 275 K probably drives the whole sample into the FE state, resulting in a small and temperature independent thermal conductivity.

4.4   Summary and conclusions

To summarize, we have performed thermal conductivity measurements for STO thin films under different degrees of epitaxial strain.

The goal was to study a possible effect of phonon scattering by fer-roelectric domain walls, which could influence the thermal conductivity of this material. We designed an strategy to differentiate the effect of point defects, such as V_{Sr} and V_O, and FE domain walls, in the thermal conductivity of STO.

We have observed an $\approx 35\%$ reduction of the room temperature thermal conductivity in the films deposited on top of STO and LSAT with respect to the bulk values for the STO. For the case of STO deposited on DSO, this reduction reaches $\approx 78\%$. Even though the reduced dimensionality and the incorporated point defects can explain the reduction in κ for the films on STO and LSAT substrates, the huge reduction for the films on DSO substrates is attributed mostly to the appearance of a FE state. The effect of the FE transition on κ is further demonstrated by temperature dependent measurements of the film on DSO, where there is a sharp decrease of the thermal conductivity around ferroelectric transition temperature.

Chapter 5

Effect of epitaxial strain and vacancies on the ferroelectric -like response of CaTiO$_3$ thin films

5.1 Introduction

In this chapter we will present the study of the effect of epitaxial strain and cationic/anionic vacancies on the transport properties of CaTiO$_3$ thin films. In particular, we are going to examine closely the possibility of establishing a ferroelectric state, previously observed by numerous groups, [11, 12, 166, 167] and study the conditions of its appearance and/or its legitimate ferroelectric nature.

CTO is mostly known for its ideal perovskite structure, however recent works have exhibited its potential for playing an important part in functional applications. CTO is one of the perovskite oxides that was reported to form a 2DEG on its interface with YTiO$_3$, [13] as well on its bare surface. [14] Moreover, it is known to be an incipient ferroelectric material, [10] however it wasn't until recently that it was reported the stabilization of a ferroelectric phase in thin films. [11, 12, 166, 167]

It was proposed that biaxial tensile strain suppresses the out-of plane TiO_6 octahedral rotation and stabilizes a $P4mm/I4mm$ space group, compatible with a ferroelectric distortion. [168]

This FE instability in CTO is highly correlated to the competition between the cation displacements and the TiO_6 octahedra rotation. In order to promote the stabilization of the FE state, the natural rotation of the TO_6 octahedra in CTO must be avoided in favor of the polar instability due to the cation displacements.

However, Yang *et al.* [167] claimed that FE can also be induced by defect-dipoles in strain-free CTO thin films. In this case, the origin of the FE state would be due to the formation of complex defects and clustering of vacancies of the type *Ca-O-O*, showing a net dipolar moment. The existence of nanopolar regions around Sr^{2+} vacancies, has also been proposed as a possible mechanism to explain the origin of the FE state in STO films. [151, 169]

On the other hand, macroscopic measurements of FE polarization by Haislmaier *et al.* [166] in CTO thin films grown by Molecular Beam Epitaxy (MBE), showed that deviations from stoichiometry completely mask and suppress the ferroelectric ordering in CTO. In particular, Ca-rich films introduced CaO rocksalt layers interspersed through the whole film, while Ti-rich films presented TiO_x defect clusters. There is, therefore, a lack of consensus about the role played by defects (cationic and anionic) on stabilizing the FE response observed in CTO, either via formation of nanopolar regions, or by suppression of TiO_6 rotation and stabilization of tetragonal $P4mm/I4mm$ phases.

Most of these reports utilized the local-response piezoelectric force microscopy (PFM) to measure the FE polarization. However, this technique can be severely influenced by changes in the surface potential and local volume due to ionic (mostly oxygen) migration under the influence of a strong electric field. This can be very important in oxides like STO, particularly susceptible to oxygen vacancy creation. [170, 171]

In this chapter we study the role of defects (oxygen and cationic vacancies) on the structural and transport properties of CTO thin

films under compressive/tensile stress. We will discuss if the modified crystal structure is compatible with ferroelectricity, under certain growth conditions. We will also explore the case of the migration of oxygen vacancies under the influence of an electric field and/or a mechanical force (which can be erroneously interpreted as a FE polarization) by EFM and PFM measurements. In addition, we report how the thermal conductivity of the thin films is affected due to the incorporation of the defects, in combination with epitaxial strain.

5.2 Experimental details

Thin films of $CaTiO_3$ (CTO) were deposited at 700℃ by Pulsed Laser Deposition (PLD, KrF $\lambda = 248$ nm, fluence ≈ 1.5 J/cm, 5 Hz) on (001) LAO and (001) LSAT substrates. The sample thickness was kept constant at 22±2 nm. Oxygen pressure was varied from $PO_2{=}1{\times}10^{-1}$ to $1{\times}10^{-6}$ Torr, in different depositions. Samples grown at $PO_2 \geqslant 1{\times}10^{-4}$ Torr were too resistive (GΩ) to be measured in our setup. The thermal conductivity, κ, of the films was measured by FDTR . [112, 172, 111] Additional temperature-dependent measurements were performed using the 3-ω method. [114, 115, 113]

The surface potential and FE behavior of the samples was studied by Electrostatic Force Microscopy Dynamic Contact (EFM-DC) or Piezoelectric Force Microscopy (PFM), and Scanning Kelvin Probe Microscopy (SKPM), in an NX-10 Park Systems AFM. For the experiments, we used Cr/Pt-coated Silicon tips with a force constant of 3 N/m, under an excitation of 20kHz and 2VAC.

5.3 Results and discussion

Bulk CTO presents an orthorhombic structure (Pbnm) with lattice parameters a = 5.379 Å, b = 5.436 Å and c = 7.639 Å (pseudocubic $a_c \approx 3.823$ Å). Therefore, growing CTO in top of LAO ($a_c = 3.790$

Å) and LSAT ($a_c = 3.868$ Å) imposes a degree of in-plane compressive/tensile strain of -0.8% and $+1.24\%$, respectively.
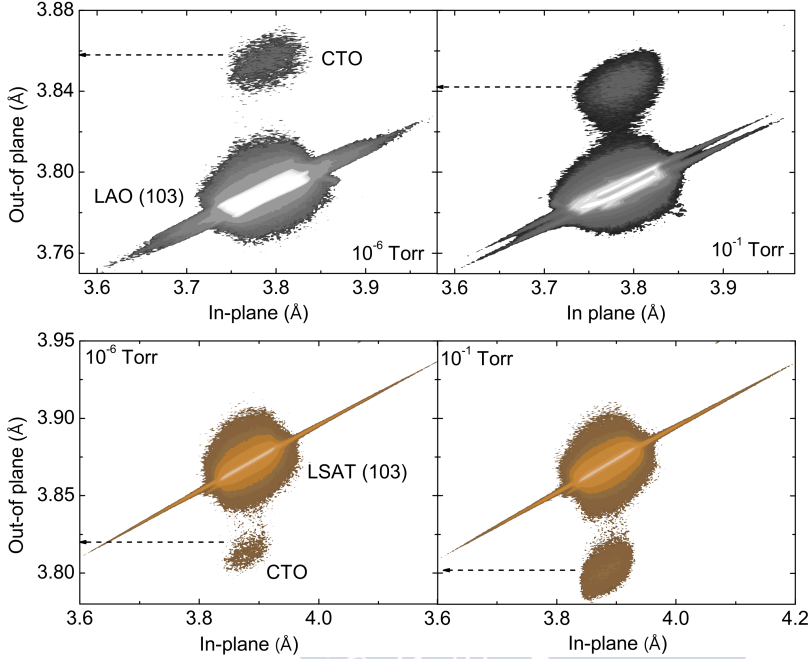
Figure 5.1: Reciprocal Space Maps for the CTO films on LAO [top] and LSAT [bottom] around the asymmetrical (103) reflection, for the two different PO_2 used during the deposition. The arrows indicate the position of the out-of plane lattice parameters of the films. All the films adopt the in-plane lattice parameters of their corresponding substrate.

Figure 5.1 depicts the Reciprocal Space Maps (RSM) performed at asymmetrical reflection (103) for films deposited under different PO_2 on LAO and LSAT substrates. The thin films deposited epitaxially on both substrates managed to adopt the in-plane lattice parameters of the substrate regardless of the PO_2 used during the deposition ($a_f \approx a_s$). The out-of plane lattice parameters obtained from the RSMs are identical to the values obtained from the fitting of the (002) Bragg peak in the XRD patterns shown in Figure 5.2. The results of the variation of the c-axis with the PO_2 is shown in Figure 5.3 for both sets of films.
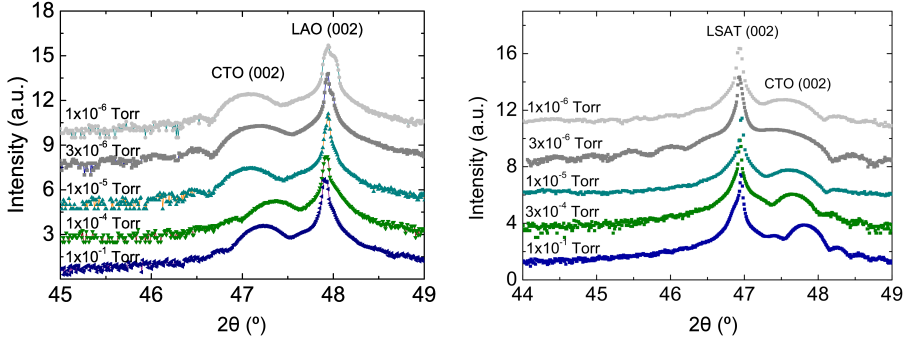
Figure 5.2: X-ray diffraction patterns around the (002) reflection of the films deposited on LAO [left] and LSAT [right] substrates.

The clamping of the thin films to the substrate produces an out-of-plane deformation, which can be quantified according to the Poisson ratio, [132] which for a biaxially strained film is:

$$\frac{2\nu}{(1-\nu)} \qquad \text{where} \qquad \nu = -\frac{\epsilon_z}{\epsilon_x}$$

where $\epsilon_x = (a_f\text{-}a_b)/a_b$; $\epsilon_z = (c_f\text{-}c_b)/c_b$ .The subscripts f and b refer to the values of the lattice parameters of the film and bulk, respectively.

Assuming $\nu \approx 0.23$, like $SrTiO_3$, [131] there should be an expansion of $\approx 6\%$ in the out of plane parameter of the films deposited on LAO. On the other hand, the tensile epitaxial stress imposed by the substrate of LSAT on CTO should result in an out-of-plane contraction of $\approx 6.5\%$. This is in excellent agreement with the experimental results for the samples deposited at the higher PO_2, as seen in Figure 5.3.

On the other hand, reducing PO_2 results in a further elongation of the c-axis, while the in-plane lattice parameters remain clamped to the substrate (see Fig. 5.1). The gradual elongation along the c-axis makes the films on LSAT to approximate the pseudocubic lattice structure of bulk $CaTiO_3$, at low PO_2. On the contrary, the films deposited on LAO depart progressively from this limit as PO_2 decreases, until a certain saturation below $PO_2 \approx 10^{-5}$ Torr.

117
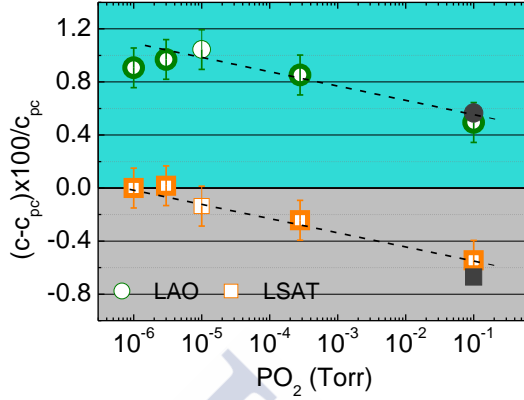
Figure 5.3: c-axis parameter normalized to the pseudocubic value of CTO, for films deposited on LAO (open circles) and LSAT (open squares) under different PO_2. Solid symbols correspond to theoretical values of the c-axis assuming a Poisson ratio of $\nu = 0.23$. The lines are guides to the eye.

The increase of c-axis can be attributed to an increasing amount of Ca^{2+} vacancies at low oxygen pressures, similar to the case of Sr^{2+} in STO. [173]

Haislmaier *et al.* also reported a c-axis elongation as an expression of deviation from the perfect stoichiometry for CTO. They reported that the stoichiometric window of CTO on LSAT would be $c \approx 3.805 - 3.808$ Å (see Fig. 5.4).

Our films are very close to being stoichiometric when deposited at $PO_2 = 0.1$ Torr, while at the lowest PO_2, the concentration of cationic/anionic vacancies increases, as it is confirmed by microscopy analysis.

High-resolution STEM images and EELS analysis on the cross-section lamellae of the films, indeed reveal nanometer-size segregation of Ti-rich regions, compatible with the clustering of Ca vacancies in the samples synthesized at the lower pressures. This contrasts with a more homogeneous distribution of cations in the films deposited at 0.1 Torr (see Fig. 5.5). As discussed before for the case of STO, depositing the films at lower PO_2 will also increase the amount of oxygen vacancies, V_O. However, post-fabrication
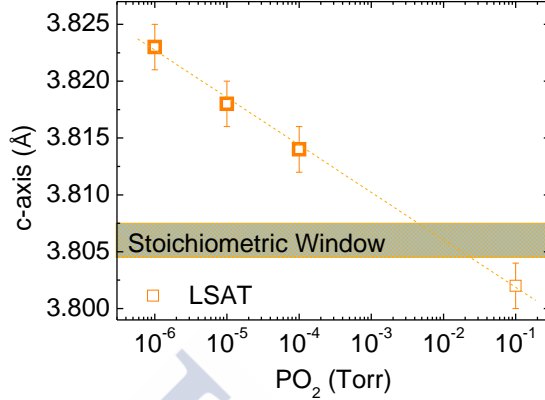
Figure 5.4: c-axis of CTO as a function of the PO_2 during the deposition on LSAT. The stoichiometric window is referred to values of the c-axis that correspond to fully stoichiometric samples, as reported in [166]. The line is guide to the eye.

annealing at different PO_2 showed a negligible effect of V_O on the c-axis expansion, confirming the dominant role of cation vacancies in this effect also for $CaTiO_3$.

The GPA analysis of high-resolution STEM images taken on cross-section lamellae are shown in Figure 5.6. The in-plane elongation ε_{xx} shows a good matching to the film, although a progressive relaxation is clearly visible moving away from the interface with the substrate. This effect is more clearly visible in the samples deposited at the lower pressures, where the amount of defects is increased. Regarding the out of-plane distortion, ε_{zz}, it is more homogeneous throughout the film and confirms the tendencies observed in the X-ray diffraction analysis.

An alternative way of determining the structural quality of the thin films and the influence of the incorporated defects on their properties, is by measuring the thermal transport of the thin films. The room temperature thermal conductivity of the films decreases linearly as the c-axis increases (see Fig. 5.7), reflecting the increasing amount of atomic defects in the films. An increase of c $\approx 1.5\%$ reduces $\kappa(T = 295K)$ by more than 50%, in line with previous
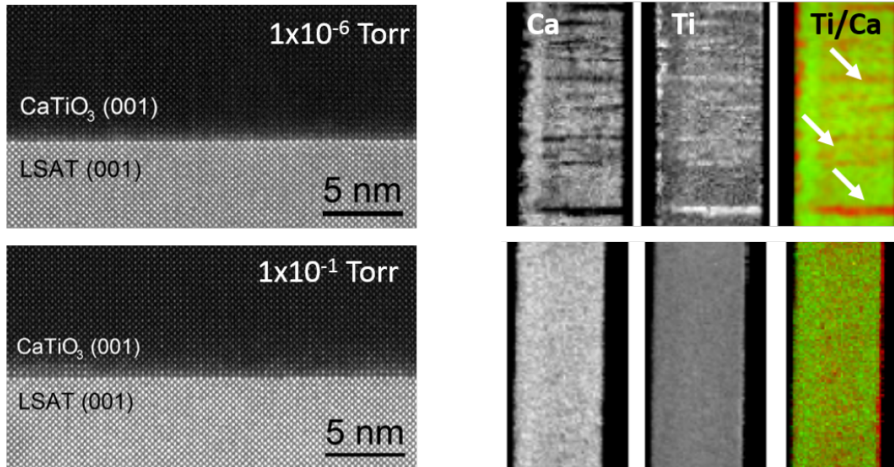
Figure 5.5: Left: High-resolution STEM images of two films deposited on LSAT at different PO_2. Right: Ca/Ti distribution maps from EELS analysis of the same films. The concentration of Ca in the red regions marked by the arrows is $\approx 5\%$ lower than expected.
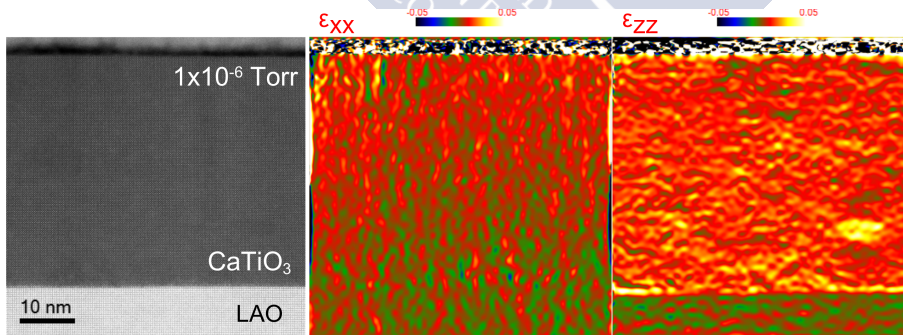
Figure 5.6: STEM and Geometrical phase analysis (GPA) maps for the CTO thin film deposited at $PO_2 = 1 \times 10^{-6}$ Torr. The GPA maps visualize the in-plane (ε_{xx}) and out-of plane (ε_{zz}) deformation of the film, using as reference the interatomic distances of the substrate.

observations in SrTiO$_3$. [161]
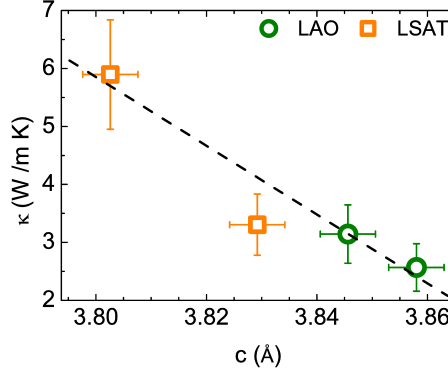
Figure 5.7: Evolution of the room temperature thermal conductivity of CTO with the c-axis lattice parameter. The dashed line is a guide to the eye.

Apart from the cationic/anionic vacancies that act as phonon scattering centers, the effect of the epitaxial strain should be taken into consideration. It is important to remark that the films were deposited on the LAO and LSAT substrates placed side-by-side in the PLD chamber, in a single deposition for each oxygen pressure. This way, the differences in the concentration and distribution of defects, reflect the different way in which the orthorhombic CTO accommodates the compressive/tensile epitaxial stress imposed by each substrate.

Another important factor that has to be considered regarding the thermal conductivity, additional to the increased concentration of defects, is the rotation of the TiO$_6$ octahedral pattern. As it will be discussed later more explicitly, the film of CTO on LSAT deposited at PO$_2 = 1 \times 10^{-1}$ Torr, exhibits the rotation pattern of (a$^+$a$^+$c^0), while the film deposited at PO$_2 = 1 \times 10^{-6}$ Torr exhibits no TiO$_6$ octahedral rotations (a^{0}a^{0}c^0). The reduction between these two samples in terms of thermal conductivity was $\approx 40\%$.

Moreover, we performed temperature dependent thermal conductivity measurements using the $3 - \omega$ technique for one of the films previously measured using the FDTR technique at room temperature. As it was explained in section 2.4.2, the $3 - \omega$ technique

121
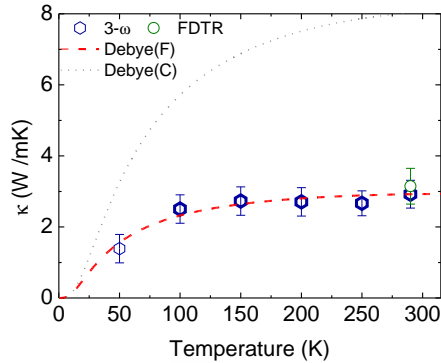
Figure 5.8: Temperature dependent thermal conductivity for the CTO thin-film deposited on LAO substrate at $PO_2 = 0.1$ Torr. The blue polygon symbols correspond to measurements implementing the $3 - \omega$ technique, while the green open circle to room temperature measurement using the FDTR technique. The red dashed line is fitted using the Debye approximation for $\kappa(T)$ with $\tau_{PD}^{-1} = 3.5 \times 10^{-42} s^{-1}$. The gray dotted line corresponds to the initially calculated $\tau_{PD}^{-1} = 4.71 \times 10^{-43} s^{-1}$ defect scattering term for an estimated vacancy concentration of $\approx 6\%$.

has the limitation of not being able to measure electrically conductive samples and moreover, when the thermal conductivity of the substrate is not much higher than the film, is hard to distinguish between the two. For this reason, we were able to perform the temperature dependent measurements for the CTO film deposited on LAO ($\kappa_{LAO} = 12$ W/m K at 300 K) at $PO_2 = 0.1$ Torr, which is insulating.

The results are plotted in Figure 5.8. The agreement between the room temperature values measured by $3 - \omega$ and FDTR is very good. Following the same procedure as in Chapter 4, we fitted the temperature dependence for the thermal conductivity, by calculating the different scattering terms. As input parameters we have considered the Debye temperature for the CTO as $\theta_D = 790$ K, [174] the Grüneisen parameter $\gamma = 1.85$, [174] the sound velocity $v = 5893$ m/s, [175] $\overline{M} = 2.72 \times 10^{-2}$ Kg/mol, and an estimated concentration of defects $V_{Ca} \approx 6\%$ and $V_O \approx 5\%$. The resulting scattering terms were: $\tau_{PB}^{-1} = 5.37 \times 10^{10} s^{-1}$, $\tau_U^{-1} = 2.85 \times 10^{-19} s^{-1}$

and $\tau_{PD}^{-1} = 4.71 \times 10^{-43} s^{-1}$.

However, the resulting $\kappa(T)$ from the calculations according to the Debye model was higher than the experimental data (gray dotted curve in Figure 5.8). Since the concentration of defects is difficult to quantify, we have let the point defect scattering time as a free parameter to see if the fitted value would be within the acceptable limit. The fitted curve (red dashed line) in Figure 5.8 corresponds to a defect scattering term of $\tau_{PD}^{-1} = 3.5 \times 10^{-42} s^{-1}$. This is consistent with a number of Ca/O defects of the order of $\approx 40\%$. This is obviously too large to be realistic. Looking at the clustering of defects observed in Figure 5.5, these results suggest that the inhomogeneous character of the films deposited at low PO_2 is responsible of the low $\kappa(T)$ observed experimentally. The clustering of vacancies is not properly accounted by the ω^4 term in the Debye approximation. This term corresponds to the Rayleigh dispersion, applicable only when the size of the defects is much smaller than the phonon wavelength.

Vacancies play a very important role in the accommodation of epitaxial stress in thin films, which in turn determines the transport properties of the films to a large extent. Apart from compensated (Schottky) defects, uncompensated V_O might form during cooling in low PO_2. Fully ionized V_O donate two electrons to the conduction band, resulting in a measurable electrical conductivity below $PO_2 \approx 1 \times 10^{-5}$ Torr.

The films deposited at the lower oxygen pressure ($PO_2 < 10^{-5}$ Torr) show a metallic like resistivity above T*, and activated behavior with a tendency towards saturation below this temperature (see Fig. 5.9 [left]) similar to the one of STO films and LAO/STO and CTO/YTiO$_3$ interfaces. In fact, both values of the charge density ($n \approx 10^{21}$) and electron mobility ($\mu \approx 1$ cm^{2}V^{-1}s^{-1}) reported by Liu et $al.$ [13] for the CTO/YTiO$_3$ interface, were comparable to the ones obtained in our studies. The electron mobility in our results is of the order of $\mu \approx 1$ cm^{2}V^{-1}s^{-1}, while the charge density varies between $n \approx 2 - 3 \times 10^{20}$cm^{-3}, irrespective of the degree of strain.
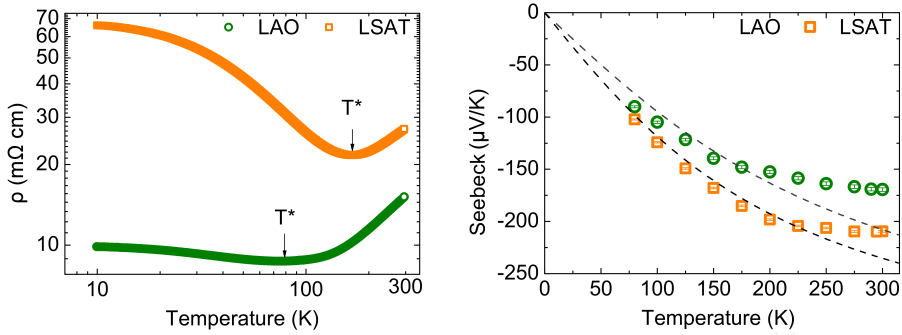
Figure 5.9: Temperature dependence of the electrical resistivity [left] and Seebeck coefficient [right] for CTO deposited at low PO_2 on LAO and LSAT. The dashed lines are the calculated values of the temperature dependent Seebeck coefficient.

Consistent with this, the Seebeck coefficient S(T) is also practically independent of the sign of strain, with a slightly lower value for the CTO on LAO, due to its larger conductivity (see Fig. 5.9). The absence of any anomaly of S(T) around T* suggest that conventional vacancy scattering is responsible for this upturn of $\rho(T<T^*)$, as discussed also for STO. The dashed lines in Figure 5.9 [right] correspond to the calculation of the Seebeck coefficient, based on the same procedure followed in Chapter 3.

This calculation used experimentally obtained data, such as the charge density n, the effective mass m^* and as only free adjustable parameter the degeneracy of the electronic bands, z. For this calculation, the input data were $n = 2.63 \times 10^{20}$ cm^{-3} for the film on LSAT and $n = 2.98 \times 10^{20}$ cm^{-3} for the film on LAO, $m^* = 1.1 m_e$ [176] and the band degeneracy for both films was $z = 6$. This means that the structural distortion due to the c-axis elongation was not enough to split the Ti:3d-t_{2g} bands and lift the degeneracy, as we reported for the case of STO thin films also deposited at low PO_2.

On the other hand, as discussed in the introduction, FE in CTO was hypothesized to be intimately linked to the octahedral rotations which accommodate the epitaxial tension. Therefore, this effect should be strongly influenced by the distribution of vacancies

in the film.

The orthorhombic *Pbnm* structure of CTO at room temperature is characterized by ($a^-a^-c^+$) tilting of the TiO$_6$ octahedra. [90] These rotations occur spontaneously in the perovskite structure to accommodate the mismatch between equilibrium (Ca-O) and (Ti-O) bond-lengths to a situation where (Ca-O)$< \sqrt{2}$(Ti-O). [90, 78] Tilting of TiO$_6$ in CTO compete with the polar instability, and actually can prevent, the occurrence of a ferroelectric distortion of the cationic sublattice in CTO. [177]

Eklund *et al.* [12] proposed that $\approx 1.5\%$ of tensile strain suppresses the octahedral rotations around the c-axis in CTO, thus permitting to the polar instability of CTO to manifest and to induce a FE state, which was also confirmed by further studies performed by Biegalski *et al.*. [11] As discussed before, the effect of vacancies was also reported to be highly detrimental for FE, suppressing the polarization as Ca/Ti deviates from 1. [166] However, whether this suppression is related to a local relaxation of the epitaxial tensile stress, or to a global change in the rotation pattern of the TiO$_6$ octahedra [85] incompatible with the FE distortion, it is an important issue that has not been clarified.

The octahedral tilts in our films were investigated by X-ray diffraction of the half-order reflections characteristic of each pattern (see Fig. 5.10). For CTO on LAO (compressive stress), we identified the half-order reflections compatible with in-phase rotations around the [100] and [010] cubic axis, and out-of-phase rotations around the [001], irrespective of the oxygen pressure. Although the comparison of the relative intensities does not allow us to distinguish between ($a^+a^+c^-$), of tetragonal $P4_2/nmc$ symmetry, and orthorhombic ($a^+b^+c^-$) *Pmmn*, it is clear that these rotations are present in the whole range of PO$_2$ studied in this work.

On the other hand, for CTO on LSAT (tensile stress), the rotation pattern changes from ($a^+a^+c^0$) at 1×10^{-1} Torr, to ($a^0a^0c^0$) at 1×10^{-6} Torr. Therefore, cation/anion vacancies in CTO grown at low PO$_2$, relax the epitaxial stress and suppress the octahedral rotations, changing the structure of CTO from tetragonal ($I4/mmn$) to
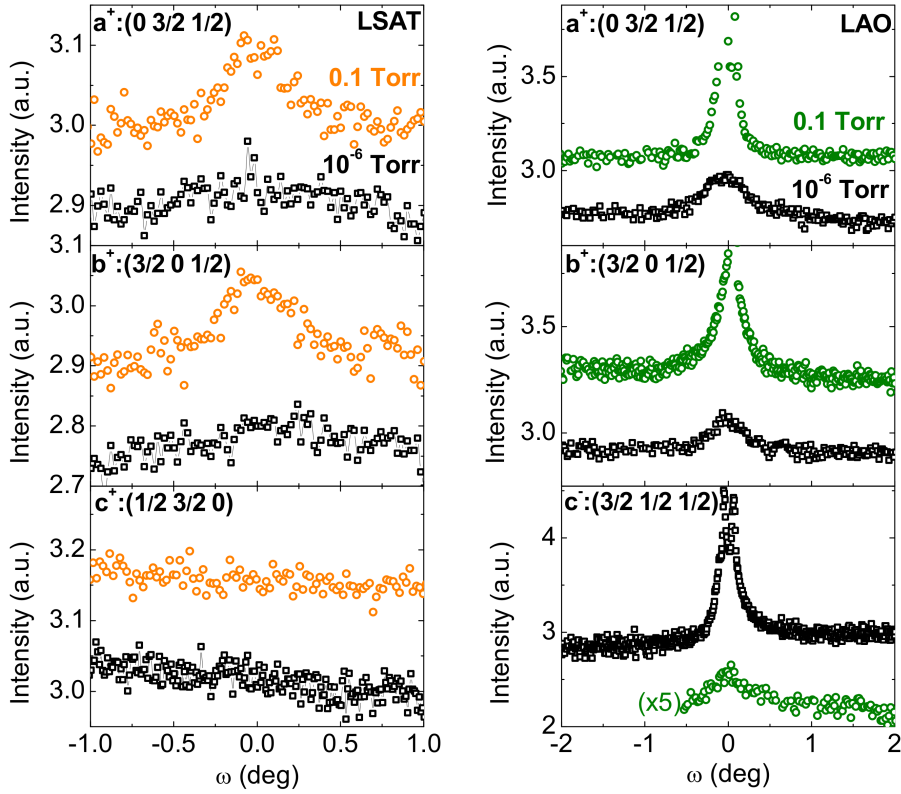
Figure 5.10: ω-scans around different half-order peaks for CaTiO$_3$ films grown on LSAT [left], and LAO [right], at 0.1 Torr and 10^{-6} Torr.

cubic ($Pm3m$). In both cases, rotations of TiO_6 octahedra around the c-axis are suppressed. Therefore, CTO on LSAT shows a structure compatible with the FE distortion, at any pressure, while CTO on LAO does not.

However, a FE response was reported for CTO both on LSAT [11] and LAO. [167] To solve this apparent contradiction we have studied the effect of a local electric field on CTO under different strain. This was monitored by following the surface potential using EFM-DC (PFM) and SKPM. The results for the films deposited at $PO_2 = 1 \times 10^{-6}$ Torr are shown in Figure 5.11. A positive/negative voltage bias applied to the sample produces a clear change in the surface potential, with a change of the phase-voltage of nearly 180°.
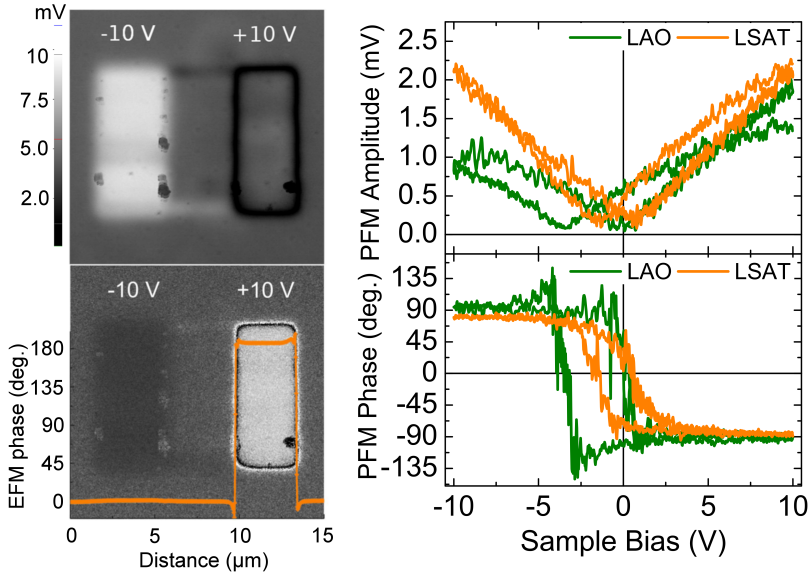
Figure 5.11: Left: EFM amplitude (top) and phase (bottom) for two areas of CTO on LSAT (10×5μm), scanned with $-10V, +10V$. Right: PFM amplitude (top) and phase (bottom) hysteresis loops for the samples on top of LAO and LSAT substrates.

When repeating these experiments on films deposited at an $PO_2 = 0.1$ Torr, with a negligible amount of V_O, we did not observe any measurable change in the SKPM signal with respect to the

background. All these suggests that the displacement of V_O by the electric field is the origin of the amplitude/phase change of the surface potential. These vacancy rich/poor areas achieved after electric field poling correspond to high/low electrical conductivity regions.

The absence of this effect in samples with a negligible amount of V_O, discards electrochemical, [178] triboelectric or surface effects, like the formation of radicals, [179] as the origin of this change in the surface potential. It is also important to note that annealing the samples at lower PO_2 increases the charge density (measured by Hall effect) in good agreement with the expectations for doubly ionized oxygen vacancies. Therefore the possibility that V_O act as charge trapping centers can be also safely discarded.

An electrostatic force acting on the tip due to accumulation/ depletion of charged-vacancies, may produce an effect similar to an electromechanical response on the AFM tip. A paradigmatic example is the FE-like, switchable electromechanical response observed in LAO/STO interfaces due to the reversible movement of oxygen vacancies. [180]

Important information to distinguish intrinsic FE response from the ionic effect can be gained from the relaxation of the signal amplitude. We followed the time decay of the voltage difference, $\Delta V(t)$, between the poled and pristine regions, from t_0 up to ≈ 12 h (see Fig. 5.12). Assuming that V_O diffuse away from the surface after removing the electric field, the solution of the Fick's diffusion equation along the film-thickness, L, leads to the following time decay of the surface potential: [181]

$$V_S(t) = \frac{\Delta V(t_0) - \Delta V(t)}{\Delta V(t_0)} \approx \frac{4}{L\sqrt{\pi}} D^{1/2} (t - t_0)^{1/2} \qquad (5.1)$$

$V_S(t)$ can be satisfactorily fitted to equation (5.1) using a coefficient of diffusion $D(V_O) \approx 2.5 \times 10^{-17} \mathrm{cm}^2/\mathrm{s}$ (see Fig. 5.13). This is very close to the value reported for $D(V_O)$ in bulk STO at room temperature. [182, 181]
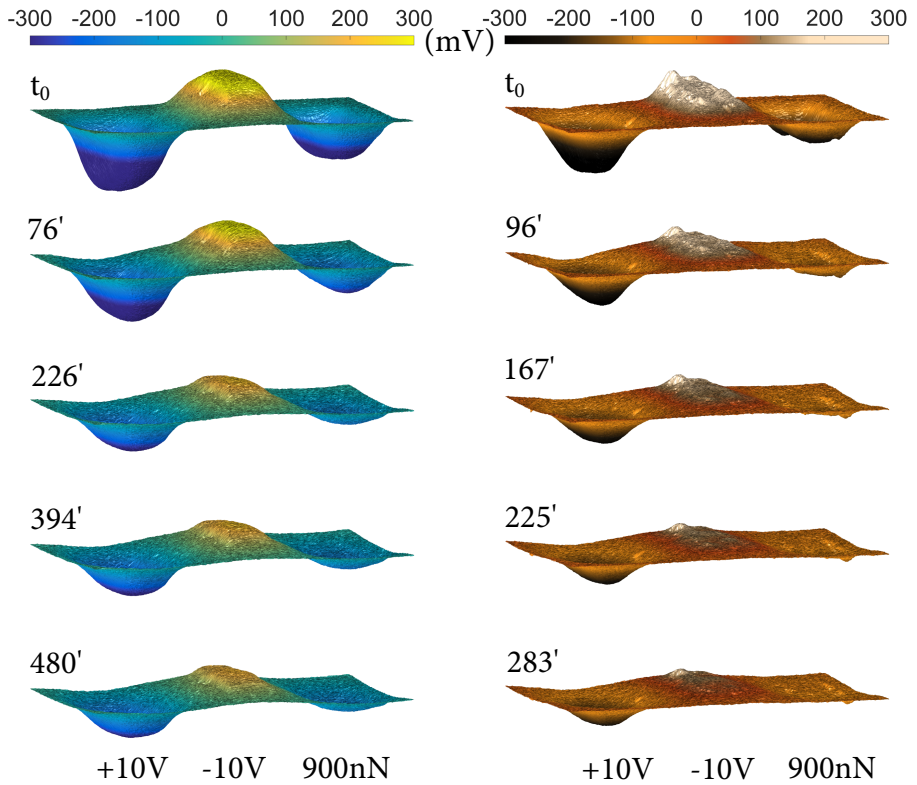
Figure 5.12: Time evolution of the SKPM voltage amplitude maps of the areas after application of an electric field (±10 V) or a mechanical force (900 nN, 0 V) on CTO thin films grown on LAO [left] and LSAT [right] substrates.

In order to further confirm the movement of oxygen vacancies as the origin of the change in the surface potential observed in CTO films, we have also tested the effect of a mechanical force applied with the AFM tip on the distribution of these vacancies. The two electrons donated by each V_O go into a non-bonding band, and produce a local expansion of the crystal lattice. [125] Therefore, the movement of charged oxygen vacancies may, in addition to changing the surface potential, produce a local expansion of the lattice, similar to a piezoelectric effect. [170]
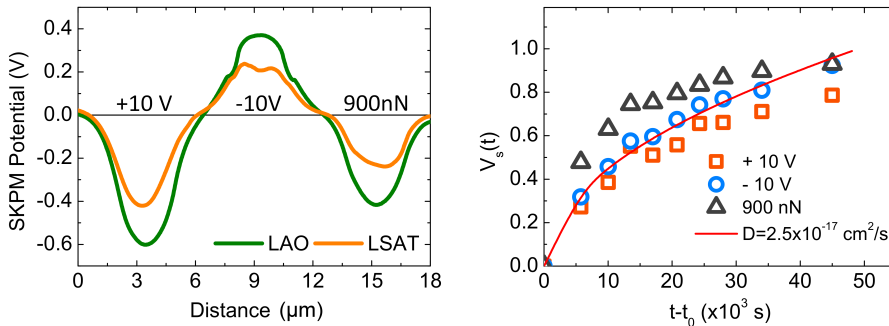
Figure 5.13: Left: Line-scan along the center of the areas after poling with ± 10 V, and mechanical tip force (900 nN, 0 V), for CTO on LSAT and LAO. Right: Time evolution of $V_S(t)$ from Fick's law of diffusion for ± 10 V and 900 nN (0 V). The solid line is the fitting to equation (5.1) for a diffusion coefficient $D \approx 2.5 \times 10^{-17}$ cm^{-3}.

Due to the local lattice expansion associated to oxygen vacancies, pushing against the surface of the film should move the vacancies against the strain gradient generated by the load, and therefore should decrease the surface potential. This is indeed observed in both films, on LAO and LSAT (see Fig. 5.12). The decay of this signal also follows the behavior predicted by equation (5.1), with a similar D (see Fig. 5.13 [right]). Any possible contribution from flexoelectricity [183] should be negligible in this case, due to the relatively large film thickness.

The results presented in this chapter show that an identical FE-like response obtained in CTO deposited on LSAT and LAO,

irrespective of the strain and crystalline phase (compatible or not with a FE distortion). Therefore these results prove that the movement of oxygen vacancies is responsible for the change in the surface potential produced after the application of an electric field and a mechanical force.

5.4 Summary and conclusions

To summarize the results of this study, we have been able to synthesize high quality thin films of CTO and have good control of the concentration of cationic/anionic defects during the deposition process. This control over the defect concentration combined with the different type of in-plane epitaxial strain (compressive or tensile) allows for the control over the manifestation or suppression of the TiO_6 octahedral rotations. The combined effect of these three parameters has a clear effect on the transport and thermoelectric properties of the films.

Due to the incorporation of a sufficiently high concentration of V_O we obtained highly conducting samples, replicating a similar behavior to the one observed as a 2DEG at the $CTO/YTiO_3$ interface. Moreover, by tuning the defect concentration and the rotation pattern of the oxygen octahedra, we were able to achieve an $\approx 40\%$ reduction of the room temperature thermal conductivity in the films on LSAT substrates, suggesting CTO as a potential thermoelectric material.

In principle, a stable FE state could be achieved by suppressing the oxygen octahedral rotations around the c-axis for CTO on LSAT, while no FE state has been predicted for CTO on LAO substrates. While we were able to replicate the conditions required to obtain a stable FE state in CTO on top of LSAT by being able to control the TiO_6 octahedral rotation pattern around the c-axis, we have observed a FE-like response for the CTO films on both substrates.

We have demonstrated that the movement of oxygen vacancies

under the influence of an electric field or a mechanical force produces a local change in the surface potential and a electromechanical-like response, which can be misinterpreted as a FE signal for CTO films on both LSAT and LAO substrates. Finally, irrespective of their origin, our results show that bi-stable states of different electrical conductivity can be written/erased in CTO with an applied electrical field and a mechanical force, opening interesting possibilities for applications in resistive switching devices.

Chapter 6

Conclusions and outlook

In this thesis, we studied the thermoelectric properties of $SrTiO_3$ and $CaTiO_3$ thin films, fabricated in a PLD system. We have been able to achieve high quality thin film with sharp interfaces on substrates that impose different degrees of epitaxial strain, and with a good control over the amount of cationic and anionic vacancies. The main general conclusions derived from these studies are:

1. The main phenomenology found in LAO/STO interfaces, that is:

   (a) a metallic-like temperature dependence of the electrical resistivity at high temperature.

   (b) a Kondo-like upturn of the electrical resistivity at low temperature, below a characteristic T*.

   (c) an anomalous component of Hall effect below T*.

   (d) a large anisotropic magnetoresistance below T*.

   can be reproduced in epitaxial thin films of $SrTiO_3$. Different degrees of strain are accommodated by creating different amounts of cationic/anionic vacancies, which produce local Ti^{3+} magnetic moments, and are responsible of all this rich phenomenology.

2. Cationic vacancies produce a homogeneous tetragonal distortion of the lattice in the whole film. This distortion has an effect in the band structure of the system, changing the effective band occupancy and determining the Seebeck coefficient to a large extent.

3. The presence of ferroelectric domain walls in $SrTiO_3$ grown on $DyScO_3$ produces a large reduction of the thermal conductivity of the material. Temperature dependent measurements of the thermal conductivity show a very good agreement with previous IR and Terahertz spectroscopic characterization of the soft-phonon mode transition in $SrTiO_3$.

4. Epitaxial strain, through the controlled production of vacancies, induced ferroelectric transitions, or the effect on electronic band degeneracy, offers a unique opportunity to control the thermal conductivity, thermoelectric power and electrical conductivity of $SrTiO_3$, partly independent from each other.

5. Most of the phenomenology observed in $SrTiO_3$ can be also reproduced in epitaxial thin films of $CaTiO_3$ under different degrees of epitaxial strain. This oxide, like $SrTiO_3$, combines a high oxygen mobility at room temperature, with a very low energy for vacancy creation. These results further demonstrate that cationic/anionic vacancies are responsible for most of the phenomenology described in polar oxide interfaces. Other oxygen conductors (perovskites, spinels, brownmillerites, etc) with $Ti^{4+/3+}$ active redox pairs, are prone to show this phenomenology, as well.

6. The high oxygen mobility at room temperature in $CaTiO_3$ can be exploited to change the local properties of the films, by using the electric-field or the force produced by an AFM tip. The electromechanical response produced by oxygen vacancies can be erroneously interpreted as a ferroelectric polarization.

7. In terms of pure thermoelectric efficiency, the best values of ZT(300 K) obtained in our films are ≈ 0.025, still too low for any practical application. Combining the best values of S, ρ, and κ obtained in different films at room temperature:

- κ of SrTiO$_3$ on DyScO$_3$, 2.3 Wm^{-1}K^{-1}.
- ρ of SrTiO$_3$ on LSAT, 7.83×10^{-3} Ω cm.
- S of SrTiO$_3$ on SrTiO$_3$, 280 μV K^{-1}.

would produce $ZT(300 \text{ K}) \approx 0.1$. The temperature dependence of S, ρ, and κ does not foresee a better performance at high temperatures.

Therefore, our results show that it is very improbable that a large value of ZT, with practical applications, can be achieved in SrTiO$_3$ or CaTiO$_3$ thin films.

Appendices

Appendix A

Frequency domain solution for the surface temperature of a layered structure

In this section we will describe the theoretical model used to extract the thermal conductivity values during the FDTR measurements. This model was developed by D.G. Cahill. [113]

To find the frequency domain solution [184] we consider a semi-infinite solid, when the surface is heated by a periodic point source of unit power at angular frequency ω

$$g(r) = \frac{e^{-qr}}{2\pi\kappa r} \tag{A.1}$$

where $g(r)$ is the temperature per unit power, $q^2 = (\mathrm{i}\omega/D)$, κ is the thermal conductivity of the solid, D its thermal diffusivity, and r the radial coordinate. Taking advantage of the cylindrical symmetry of the laser beams, we use the Hankel transforms [185, 186] and the solution simplifies to

$$G(k) = \frac{1}{\kappa(4\pi^2 k^2 + q^2)^{1/2}} \tag{A.2}$$

Since in this thesis we are working with thin films, we have to look for the solution for a layered geometry. Feldman [187] has

developed an algorithm that modifies the solution $G(k)$. The final result is obtained iteratively: numbering the layers by $n = 1$ for the surface layer, the iteration starts from the farthest layer from the surface. In reality in an FDTR setup the heat cannot reach the other side of the bottom layer (the substrate), therefore: $B^+ = 0$ and $B^- = 1$.

$$\begin{pmatrix} B^+ \\ B^- \end{pmatrix} = \frac{1}{2\gamma_n} \begin{pmatrix} e^{-u_n L_n} & 0 \\ 0 & e^{u_n L_n} \end{pmatrix} \times \begin{pmatrix} \gamma_n + \gamma_{n+1} & \gamma_n - \gamma_{n+1} \\ \gamma_n + \gamma_{n+1} & \gamma_n + \gamma_{n+1} \end{pmatrix} \begin{pmatrix} B^+ \\ B^- \end{pmatrix}_{n+1} \tag{A.3}$$

where

$$u_n = (4\pi^2 k^2 + q_n^2)^{frac12} \tag{A.4}$$

$$q_n^2 = \frac{i\omega}{D_n} \tag{A.5}$$

$$\gamma_n = \kappa_n u_n \tag{A.6}$$

Each layer n is described by three parameters: the thermal conductivity κ, thermal diffusivity D_n and thickness L_n. This way, for a layered structure we will use as a solution:

$$G(k) = \left(\frac{B_1^+ + B_1^-}{B_1^+ - B_1^-} \right) \frac{1}{\gamma_1} \tag{A.7}$$

The intensity $p(r)$ of the *pump* laser that heats periodically the surface has a Gaussian distribution:

$$p(r) = \frac{2A}{\pi w_0^2} e^{-2r^2/w_0^2} \tag{A.8}$$

where w_0 is the $1/e^2$ radius of the pump laser, A is the amplitude of the heat absorbed by the sample at frequency ω. The Hankel transform of $p(r)$ is

$$P(k) = A e^{\frac{\pi^2 k^2 w_0^2}{2}} \tag{A.9}$$

The distribution of the temperature oscillations $\theta(r)$ at the surface is the inverse product of $G(k)$ and $P(k)$:

$$\theta(r) = 2\pi \int_0^\infty P(k)G(k)J_0(2\pi kr)k\,dk \qquad \text{(A.10)}$$

where J_0 is the Bessel function of the first kind of zero order.

The surface temperature is determined by the changes in the reflectivity with temperature (thermoreflectance), using a *probe* laser, whose reflected intensity changes according to the temperature profile on the surface of the sample. Its intensity presents Gaussian distribution with w_1 the $1/e^2$ radius of the beam. The *probe* beam measures a weighted average of the temperature distribution $\theta(r)$:

$$\Delta T = \frac{4}{w_1^2} \int_0^\infty \theta(r)e^{-2r^2/w_1^2}r\,dr \qquad \text{(A.11)}$$

The integral over r is the Hankel transform of a Gaussian, leaving a single integral over k that must be evaluated numerically:

$$\Delta T = 2\pi A \int_0^\infty G(k)e^{-\pi^2 k^2(w_0^2+w_1^2)/2}k\,dk \qquad \text{(A.12)}$$

This is the final expression that we are using in order to extract the effective thermal conductivity of the samples. Since the laser beam radii for the *pump* and *probe* laser is practically the same, we will use $w_0 = w_1 = w$. The fitting of the data is performed for two variables, the thermal conductivity κ and the beam's radius w. However, previous calibration and determination of the actual radius of the laser beam permit us to fit the data mainly for the value of the thermal conductivity.

In Table A is presented an example of the parameters for a 10.9 nm film of Nb:STO deposited on top of a DSO substrate, with the capping layers of Cr and Au.

141

Parameter	Au Layer	Cr Layer	Film/Interface	Substrate
κ (W/m-K)	117.9	117.9	coef(1)	1.3
ρ (Kg/m^3)	19300	7190	4699	6900
C_p (J/Kg-K)	129	460.5	532	423
L (nm)	72.3	9.9	10.9	500000

The only unknown for the fitting is the *effective* thermal conductivity. In order to separate the contributions of the thin film and the sum of the interfaces, we follow the procedure described in section 2.4.1.

Appendix B

List of publications

1. Electronic degeneracy and intrinsic magnetic properties of epitaxial Nb:SrTiO$_3$ thin films controlled by defects
   A. Sarantopoulos, E. Fereiro-Vila, V. Pardo, C. Magén, M.H. Aguirre and F. Rivadulla
   Physical Review Letters 115 (16), 166801

2. Oxygen vacancies in strained SrTiO$_3$ thin films: Formation enthalpy and manipulation
   L. Iglesias, A. Sarantopoulos, C. Magén and F. Rivadulla
   Physical Review B 95 (16), 165138

3. Effect of epitaxial strain and vacancies on the ferroelectric-like response of CaTiO$_3$ thin films
   A. Sarantopoulos, WL Ong, Jonathan A Malen and F. Rivadulla
   Applied Physics Letters 113 (18), 182902

Appendix C

Resumen en castellano

C.1   Introducción

El comienzo de este siglo ha estado marcado por un avance exponencial de la tecnología, dando como resultado dispositivos más pequeños y rápidos que nunca. Sin embargo, el uso cotidiano de esos dispositivos electrónicos viene acompañado por un consumo excesivo de energía. Por eso es imprescindible el desarrollo de fuentes de energía limpias y sostenibles. En las últimas décadas se ha producido un gran esfuerzo para el desarrollo de fuentes de energía limpias, cómo la energía solar y eólica. Sin embargo, en la mayoría de los procesos de producción y utilización de energía, se pierde una gran parte en forma de calor. Esa energía se puede aprovechar a través de los materiales termoeléctricos. El efecto Seebeck cuantifica la propiedad de los materiales conductores de generar una diferencia de potencial eléctrico como consecuencia de un gradiente de temperatura, en la ausencia de corriente eléctrica.

La eficiencia de la transformación de energía del gradiente térmico a eléctrico (el efecto termoeléctrico) se evalúa a través de la figura de mérito ZT, la cual se define cómo: $ZT = S^2\sigma T/\kappa$. S es el coeficiente de Seebeck, σ es la conductividad eléctrica, κ es la conductividad térmica y T la temperatura absoluta. Los dispositivos comerciales necesitan un $ZT \approx 1$, pero hasta hoy en día, los ma-

teriales termoeléctricos más eficientes están basados en elementos metálicos pesados como el Pb, Sb, y Te, cuáles se pueden degradar a temperaturas muy elevadas y ser tóxicos en algunos casos.

Por ese motivo es necesario el desarrollo de materiales termoeléctricos eficientes basados en elementos más seguros. Sin embargo, aumentar la eficiencia termoeléctrica es un reto difícil, ya que las propiedades responsables están entrelazadas y es muy difícil cambiar uno de los coeficientes de transporte sin afectar a los otros. Para mejorar el ZT, un material necesita presentar un alto coeficiente de Seebeck (semiconductores con baja densidad de portadores), alta conductividad eléctrica (metales) y baja conductividad térmica (aislantes). Una familia de materiales semiconductores que es prometedora, es la de los materiales basados en óxidos que presentan la estructura cristalina de perovskita. Las características de esa familia son la estabilidad térmica y eléctrica, así como su versatilidad química.

Aparte de la selección de los materiales adecuados, también es muy importante el proceso de su fabricación. El gran avance de la tecnología ha permitido el desarrollo de técnicas de deposición física, cómo la deposición por láser pulsado (PLD), la epitaxia de haces moleculares (MBE), la deposición atómica por capas (ALD) y la pulverización catódica (Sputtering). Estas técnicas permiten tener una precisión en nivel atómico al fabricar los materiales lo cuál da la oportunidad de mejorar sus propiedades funcionales. Una vía prometedora para el diseño de nuevos materiales termoeléctricos es la fabricación de películas delgadas, ya que el control sobre su dimensionalidad añade un factor más para poder controlar, de forma separada, sus propiedades de transporte.

En este aspecto, uno de los materiales más interesantes en la familia de los óxidos con estructura de perovskita, es el titanato de estroncio, $SrTiO_3$ (STO). Es un material diamagnético, aislante paraeléctrico quántico, con un ancho de banda de 3.2 eV. Fue el primer óxido superconductor identificado [1] y se puede convertir en conductor eléctrico a través de dopaje catiónico (La, Nb) o aniónico ($SrTiO_{3-\delta}$). También se ha reportado presentar compor-

tamiento ferromagnético, ferroeléctrico y se ha usado cómo material base para aplicaciones de resistive switching. [4, 5, 6] Cuando se reduce su dimensionalidad, exhibe un gran aumento en su eficiencia termoeléctrica, lo cual le coloca entre los materiales termoeléctricos potenciales. [7, 8]

Además, la interfase entre el STO y el, también aislante, $LaAlO_3$ (LAO), presenta un gas bidimensional de electrones (2DEG) de alta movilidad, debido a un desajuste de polaridad entre los dos materiales, lo cual hace que la interfase exhibe comportamiento metálico. [9] Además, se ha reportado la observación de magnetismo, superconductividad y poder termoeléctrico elevado en esta interfase. Esos fenómenos también se han observado en interfases de STO con otros materiales aislantes, o en la superficie de STO en alto vacío. Hasta ahora, no hay un consenso sobre un mecanismo concreto detrás de la formación del 2DEG, pero entre los más importantes son el desajuste de polaridad de la interfase, la creación de vacantes de oxígeno, la adsorción superficial de moléculas polares, o la mezcla de cationes en la interfase entre los dos óxidos.

Otro material interesante de la misma familia es el titanato de calcio, $CaTiO_3$ (CTO). Es un material aislante, pero se convierte en conductor eléctrico cuando es deficiente de oxígeno o cuando se somete en reemplazamiento catiónico. Es un material potencialmente ferroeléctrico, [10, 11, 12] como el STO, y también hay estudios en los cuales se ha observado la formación de un gas bidimensional de electrones en su superficie en condiciones de vacío o cuando está en contacto con el, también aislante, $YTiO_3$. [13, 14] Esa versatilidad del CTO lo hace un material prometedor para dispositivos funcionales o cómo parte de sistemas basados en óxidos más complejos.

El objetivo de esta tesis es estudiar las propiedades fundamentales de transporte de estos dos óxidos basados en Ti, e investigar cómo los cambios en las condiciones de crecimiento, defectos incorporados, y otras modificaciones estructurales relacionadas con la tensión epitaxial, pueden influir sus propiedades funcionales. Empezaremos estudiando el efecto de la tensión epitaxial y la incor-

poración de defectos aniónicos y catiónicos sobre las propiedades del STO, y cómo podemos manipular su estructura para entender su efecto en la respuesta termoeléctrica de este material. A continuación, nos concentramos en el estudio del transporte del calor en el STO y cómo esa manipulación estructural afecta uno de los parámetros más importantes, la conductividad térmica, para la eficiencia termoeléctrica. Por último, presentamos los resultados sobre las propiedades del CTO y cómo la tensión epitaxial combinada con vacantes aniónicos puede cambiar sus propiedades de transporte eléctrico y térmico. Además, demostramos que a través de la manipulación de las vacantes de oxígeno se puede conseguir una respuesta del material parecida a respuesta ferroeléctrica.

C.2 Técnicas experimentales utilizadas en este trabajo

Todas las muestras estudiadas en este trabajo son películas delgadas de espesor nanométrico, fabricadas mediante la deposición por láser pulsado (PLD), una de las técnicas más empleadas para la fabricación de películas delgadas. El equipo de PLD utilizado en este trabajo utiliza dos láseres distintos, un KrF Excimer ($\lambda = 248$nm, duración de pulso ≈ 20 ns) y un láser de estado sólido Nd:YAG (Q-Smart, $\lambda = 266$ nm, duración de pulso ≈ 6 ns). El haz del láser entra en un cámara de alto vacío, la cual puede mantener una atmósfera controlada ($PO_2 = 10^{-8} - 5 \times 10^{-1}$ Torr, de N_2 o O_2), e impacta al blanco del material deseado para la deposición. El impacto crea una pluma de ablación cual transfiere las especies atómicas al sustrato, manteniendo la estequiometria. El sustrato está colocado a una distancia de 5 cm enfrente del blanco y está en contacto con un calentador que puede elevar la temperatura hasta 960℃.

Los blancos de PLD de varias composiciones fueron preparados a través de una reacción de estado sólido de reactivos comerciales. Para la fabricación del blanco de titanato de estroncio

148

dopado con niobio ($Nb_{0.05}SrTi_{0.95}O_3$), polvos comerciales de $SrCO_3$, TiO_2 y Nb_2O_5 fueron mezclados a mano y en un molino de bolas, a continuación, compactados en una prensa hidráulica para formar un blanco circular de 1 pulgada de diámetro. A continuación, el blanco fue sinterizado en horno tubular durante 12 horas a 1200℃ en flujo continuo de gas de 95%N_2 - 5%H_2. El proceso fue repetido con la segunda sinterización a 1300℃. El mismo proceso fue seguido para la fabricación del blanco de $CaTiO_3$, con la diferencia de que la sinterización fue en atmósfera de aire y a temperatura de 1400℃. La composición correcta de los blancos fue comprobada a través de difracción de rayos X y de espectroscopía de energía dispersa (EDS).

Un paso muy importante que mejora la calidad de las películas delgadas es la preparación previa de los sustratos donde se depositarán las películas delgadas. Los sustratos de STO pasan por un proceso de limpieza con agua destilada, un pulido superficial húmedo por ácido clorhídrico para eliminar las capas superficiales de SrO y un tratamiento térmico final a 1000℃ durante 30 min. Después del proceso, la superficie del sustrato se queda con las terrazas atómicamente planas de TiO_2. Los sustratos de $(LaAlO_3)_{0.3}(Sr_2AlTaO_5)_{0.7}$ (LSAT), $LaAlO_3$ (LAO) y $DyScO_3$ (DSO), se han sometido a tratamientos térmicos a 1300℃, 1000℃ y 1200℃, respectivamente, para obtener una terminación superficial más plana.

Una vez fabricadas las muestras, se evalúa el espesor y la estructura cristalina a través de medidas de reflectividad (XRR) y difracción (XRD) de rayos X, respectivamente. En XRR, el haz de rayos X incide a la muestra en ángulos casi rasantes y la interferencia constructiva entre los planos atómicos paralelos a la superficie, produce una oscilación de máximos y mínimos a la señal difractada. Ajustando la señal obtenida se consigue información sobre el espesor y la rugosidad de la superficie de las muestras. En XRD, el haz incide la muestra en ángulo θ y se difracta en ω, manteniendo siempre la relación $\theta = \omega$. Los planos atómicos hkl paralelos a la superficie contribuyen a las reflexiones de Bragg y proporcionan

información sobre la orientación cristalográfica y del parámetro de red cristalina perpendicular a la superficie de la película delgada. La medida que proporciona información sobre los parámetros de red cristalina paralelos a la superficie de la muestra, se puede obtener a través de medidas de cartografía del espacio recíproco (RSM), alrededor de reflexiones de Bragg asimétricas. Es una medida importante, ya que da información sobre si la película delgada ha adoptado los parámetros de red del sustrato o no.

Además, estudiando las reflexiones de Bragg semi-enteras, se puede obtener información sobre la rotación de los octaedros de TiO_6 de la estructura de perovskita, cual puede ser determinante para las propiedades de las películas delgadas. Otras técnicas de caracterización estructural de las películas delgadas son las técnicas de microscopía electrónica de transmisión y barrido (STEM) proporcionando visualización directa de la estructura cristalina de las muestras, y la microscopía de fuerzas atómicas donde examinamos la topografía de la superficie y la respuesta ferro-piezoeléctrica de las muestras.

El siguiente paso es la caracterización del transporte eléctrico y termoeléctrico de las muestras. Para medir la conductividad eléctrica, implementamos la configuración Van der Pauw, donde la muestra se conecta eléctricamente en las cuatro esquinas con hilos de aluminio y se inyecta corriente por dos adyacentes y se mide el voltaje entre las dos de enfrente. Este proceso se repite cuatro veces rotando la posición de inyección de la corriente y la medición del voltaje. Así se pueden eliminar desajustes que introducen ruido en la medida. Usando una configuración similar y aplicando un campo magnético, podemos estudiar el efecto Hall y obtener información sobre la concentración de portadores libres en las muestras.

Para la caracterización termoeléctrica, hemos desarrollado un sistema de medidas propio en nuestro grupo, que garantiza medidas precisas con gran resolución térmica. En la superficie de la película delgada evaporamos líneas de platino diseñadas por litografía óptica, las cuales sirven cómo calentador y termómetros locales. Antes de la medida actual, calibramos los dos termómetros realizando una

rampa de temperatura muy lenta, así asignando un valor de resistencia a una temperatura. En la medida del coeficiente Seebeck, la muestra está estabilizada térmicamente a una temperatura base y empezamos a inyectar corriente eléctrica en el calentador local, cual crea un gradiente térmico en la muestra. Los termómetros capturan la subida local de temperatura y en puntos adyacentes medimos el voltaje de Seebeck al mismo tiempo. Así obtenemos una relación entre gradiente de temperatura y el voltaje Seebeck con alta resolución que nos permite determinar el coeficiente Seebeck de la película delgada.

Para la caracterización del transporte térmico de las películas delgadas se han usado dos técnicas distintas, la termoreflectancia de dominios de frecuencia (FDTR) y la de $3 - \omega$. FDTR es una técnica óptica y de no contacto que se puede implementar en muestras sólidas o líquidas, con la gran ventaja de poder medir muestras eléctricamente conductoras. Tiene una gran versatilidad en el tipo de muestras en la que se puede implementar y tiene un rango de resolución muy grande, ya que puede determinar valores de conductividad térmica desde 1 hasta 1000 W /m K. La preparación previa de las muestras es mínima, ya que sólo se necesita una capa metálica (típicamente de Au) depositada sobre la superficie de la muestra, que actúa como transductor de la energía del pulso de laser en energía e forma de calor a la muestra. Esta técnica utiliza dos láseres continuos co-alineados, de los cuales uno (láser de bombeo) calienta la superficie de la muestra de manera periódica y el otro (láser de medida) se implementa para detectar los cambios de la señal producida por el cambio de la reflectancia de la capa de Au. La señal del láser de medida se analiza y se ajusta en un modelo de transporte térmico, de donde se obtienen los valores de la conductividad térmica y de la conductancia de la interfase.

La técnica de $3 - \omega$ utiliza una línea de platino (Pt) evaporada en la superficie de la muestra, cual sirve cómo calentador y detector de temperatura a la vez. Es una técnica muy implementada para medidas de conductividad térmica en películas delgadas, aunque tiene una limitación importante, ya que solo es aplicable

en muestras eléctricamente aislantes. El procedimiento de la medida empieza con inyectar una corriente alterna en la línea de Pt de frecuencia ω, la cual produce un calentamiento tipo Joule en la superficie de la muestra, en una frecuencia de $2 - \omega$. Estas oscilaciones de temperatura en la superficie de la muestra producen una caída de voltaje a lo largo de la línea de Pt, con una frecuencia de $3 - \omega$. Ese voltaje proporciona información sobre el transporte térmico en la muestra. Cuando se mide una película delgada, la dependencia con frecuencia del voltaje $3 - \omega$ incluye información sobre el transporte térmico de la muestra y el sustrato a la vez. Para aislar la información que corresponde sólo a la película delgada, se procura dejar una parte del sustrato sin película, usando una máscara durante el proceso de deposición. Así, se puede medir a la vez la muestra y solo el sustrato y, restando las dos señales, se puede obtener la conductividad térmica de la película delgada.

C.3   Resultados y conclusiones

Para estudiar el efecto de las vacantes catiónicas y aniónicas sobre las propiedades termoeléctricas del STO, hemos fabricado películas delgadas de STO ligeramente dopadas con Nb (Nb:STO), depositadas en dos sustratos distintos: en STO, que no supone ninguna tensión epitaxial y en LSAT que impone una compresión epitaxial en el plano a la película delgada de STO. Se han realizado varias deposiciones de películas de Nb:STO, usando distintas presiones de oxígeno dentro de la cámara del PLD. Hemos observado que al disminuir la presión de PO_2, la concentración de defectos catiónicos y aniónicos aumenta y eso resulta en una expansión del parámetro de la red cristalina con dirección fuera del plano. Esa expansión combinada con el hecho que el parámetro de red en el plano se mantiene constante, resulta en una distorsión tetragonal homogénea de la celda unidad de la película delgada. Dicha distorsión tetragonal aumenta en función de la disminución de la presión de oxígeno, la cual nos permite controlar las características de las muestras en el

momento de la deposición.

Hemos observado que debido a esa distorsión tetragonal y la presencia de vacantes de oxígeno, las películas presentaron comportamiento similar a lo observado en las interfases de LAO/STO, cómo la presencia de un comportamiento tipo Kondo en la resistividad eléctrica, o la aparición de un efecto Hall anómalo a baja temperatura. Además, hemos observado en nuestras muestras la presencia de magnetoresistencia en- y fuera del plano, un comportamiento idéntico a lo observado en interfases de LAO/STO y de SmTiO$_3$/STO, previamente asociado con la polaridad de la interfase y con momentos magnéticos aislados. Sin embargo, nuestras muestras presentaron una anisotropía magnética, cual indica que la posible fuente de ese comportamiento es una fase magnética ordenada en STO puro, debido a la presencia de vacantes de Sr-O, que inducen la presencia de Ti^{3+} : $3d^1$ magnéticamente polarizable.

Además, la distorsión tetragonal afecta también las propiedades electrónicas y termoeléctricas de las muestras. Controlando la distorsión tetragonal nos permite controlar la ocupación de las bandas electrónicas de Ti:3d-t$_{2g}$, abriendo caminos alternativos para el control y la mejora de la eficiencia termoeléctrica. Por otra parte, hemos realizado estudios sobre el efecto de la tensión epitaxial y los defectos incorporados en la red cristalina de las muestras sobre la conductividad térmica. Hemos depositado películas delgadas sobre sustratos de LSAT, STO y DSO, cual corresponde a una tensión epitaxial compresiva (-0.9%), nula y extensiva ($+1.15\%$), respectivamente, a los parámetros de red de las muestras en el plano. A mayores, hemos realizado deposiciones a tres presiones de oxígenos diferentes, así incorporando distinta concentración de defectos para cada tanta de muestras. El efecto de la dimensionalidad reduce la conductividad térmica de STO, sobre los sustratos de STO y LSAT, a un 43%, comparando con el STO masivo. Cálculos teóricos predicen una reducción de 3.5% por el efecto de la tensión epitaxial debido al sustrato de LSAT, lo que está de acuerdo con los resultados observados experimentalmente. Adicionalmente, creando intencionalmente vacantes de oxígeno, resulta a una reducción adi-

cional de la conductividad térmica, a un porcentaje del 30%.

Sin embargo, el STO sobre DSO tiene una reducción de 78%, en vez de la prevista de un 9% por la tensión epitaxial aplicada a la película delgada. Además, midiendo la conductividad térmica en función de la temperatura, encontramos una disminución abrupta de la conductividad térmica para temperaturas menores que los 275K, la temperatura donde estaba prevista teóricamente y comprobada experimentalmente en otros estudios, la transición ferroeléctrica del STO cuando está depositado en DSO. Por debajo de la temperatura de transición, los valores de la conductividad térmica se mantienen casi constantes. Eso indica que la conductividad tan baja para este caso es muy probable que sea debido a la formación de dominios ferroeléctricos y la fuerte dispersión de los fonones sobre ellos. En la literatura, se han reportado resultados en sistemas parecidos de que los fonones se dispersan fuertemente en las paredes de dominios.

Usando un modelo para la aproximación de Debye sobre la conductividad térmica, pudimos ajustar los datos de la conductividad térmica del STO sobre LSAT, calculando los términos de dispersión de los fonones más importantes para nuestro sistema: la dispersión debido a las fronteras de las películas delgadas, los defectos y de los procesos *Umklapp*. En el caso de STO sobre DSO, el modelo de Debye no reproduce la transición abrupta en la conductividad térmica alrededor de los 275K. Sin embargo, se pudo obtener una descripción general para los dos extremos, para la alta temperatura, con términos de dispersión parecidos al caso de STO sobre LSAT, y para la baja temperatura, calculando un término aumentado de dispersión por las fronteras (en la región ferroeléctrica).

Por último, hemos fabricado y estudiado películas delgadas de CTO en dos diferentes sustratos, LAO y LSAT, imponiendo una tensión epitaxial compresiva y extensiva, respectivamente. En este caso, no hemos realizado sustitución catiónica, así que para obtener muestras eléctricamente conductoras fue necesario crear vacantes de oxígeno (cada vacante de oxígeno ionizada aporta dos electrones en la banda de conducción del Ti:3d). Cómo en el caso de STO, las

vacantes catiónicas provocadas por la deposición de las películas delgadas a baja PO_2, producen una expansión de la red fuera del plano, pero en el caso de CTO, combinado con la tensión epitaxial, se pueden modificar los patrones de las rotaciones de los octaedros TiO_6. La diferencia entre el CTO depositado sobre LSAT de manera estequiométrica y con una cantidad de defectos elevada se refleja por un cambio en el patrón de las rotaciones de los octaedros, de $(a^+a^+a^0)$ a $(a^0a^0a^0)$. La combinación de los defectos elevados y el cambio en el patrón de las rotaciones se refleja en un cambio en la conductividad térmica del 40%, cual colocaría el CTO sobre LSAT cómo posible material termoeléctrico.

Además, creando más vacantes de oxígeno, las muestras se hacen más conductoras eléctricamente, con un comportamiento casi idéntico a los estudios reportados sobre la creación de un gas de electrones bidimensional en la superficie o en la interfase del CTO $/YTiO_3$. Adicionalmente, observamos que el poder termoeléctrico no depende de la tensión epitaxial, cómo en el caso del STO.

El CTO sobre LSAT es compatible con una fase ferroeléctrica mientras haya una supresión de las rotaciones de los octaedros en la dirección fuera del plano y mientras se mantiene la estequiometría del material. Sin embargo, en medidas de microscopía de fuerzas electrostáticas hemos observado comportamiento compatible con una fase ferroeléctrica en las películas delgadas depositadas en ambos sustratos. Este comportamiento se ha observado sólo en muestras eléctricamente conductoras, lo que subraya el papel de los vacantes de oxígeno. Aplicando un voltaje externo o fuerza mecánica, fuimos capaces de manipular las vacantes de oxígeno, reproduciendo una fenomenología parecida a un material ferroeléctrico, debido a la expansión y contracción de la red cristalina cómo resultado del movimiento de las vacantes de oxígeno. Este es un resultado importante, ya que demuestra que el movimiento de vacantes en óxidos tipo perovskita como el STO o el CTO produce un efecto electromecánico similar al de un sistema ferroeléctrico, por lo que ambos efectos pueden confundirse fácilmente.

Bibliography

[1] C. Koonce, M. L. Cohen, J. Schooley, W. Hosler, and E. Pfeiffer, "Superconducting transition temperatures of semiconducting $SrTiO_3$," *Physical Review*, vol. 163, no. 2, p. 380, 1967.

[2] K. Van Benthem, C. Elsässer, and R. French, "Bulk electronic structure of $SrTiO_3$: experiment and theory," *Journal of applied physics*, vol. 90, no. 12, pp. 6156–6164, 2001.

[3] H. Weaver, "Dielectric properties of single crystals of $SrTiO_3$ at low temperatures," *Journal of Physics and Chemistry of Solids*, vol. 11, no. 3-4, pp. 274–277, 1959.

[4] C. A. Jackson, J. Y. Zhang, C. R. Freeze, and S. Stemmer, "Quantum critical behaviour in confined $SrTiO_3$ quantum wells embedded in antiferromagnetic $SmTiO_3$," *Nature communications*, vol. 5, p. 4258, 2014.

[5] Y. Li, S. Choudhury, J. Haeni, M. Biegalski, A. Vasudevarao, A. Sharan, H. Ma, J. Levy, V. Gopalan, S. Trolier-McKinstry, *et al.*, "Phase transitions and domain structures in strained pseudocubic (100) $SrTiO_3$ thin films," *Physical Review B*, vol. 73, no. 18, p. 184112, 2006.

[6] A. Sawa, "Resistive switching in transition metal oxides," *Materials today*, vol. 11, no. 6, pp. 28–36, 2008.

[7] H. Ohta, S. Kim, Y. Mune, T. Mizoguchi, K. Nomura, S. Ohta, T. Nomura, Y. Nakanishi, Y. Ikuhara, M. Hirano, *et al.*, "Giant thermoelectric seebeck coefficient of a two-dimensional electron gas in $SrTiO_3$," *Nature materials*, vol. 6, no. 2, p. 129, 2007.

[8] H. Ohta, Y. Mune, K. Koumoto, T. Mizoguchi, and Y. Ikuhara, "Critical thickness for giant thermoelectric seebeck coefficient of 2DEG confined in $SrTiO_3/SrTi_{0.8}Nb_{0.2}O_3$ superlattices," *Thin Solid Films*, vol. 516, no. 17, pp. 5916–5920, 2008.

[9] A. Ohtomo and H. Hwang, "A high-mobility electron gas at the $LaAlO_3/SrTiO_3$ heterointerface," *Nature*, vol. 427, no. 6973, p. 423, 2004.

[10] V. Lemanov, A. Sotnikov, E. Smirnova, M. Weihnacht, and R. Kunze, "Perovskite $CaTiO_3$ as an incipient ferroelectric," *Solid State Communications*, vol. 110, pp. 611–614, may 1999.

[11] M. D. Biegalski, L. Qiao, Y. Gu, A. Mehta, Q. He, Y. Takamura, A. Borisevich, and L.-Q. Chen, "Impact of symmetry on the ferroelectric properties of $CaTiO_3$ thin films," *Applied Physics Letters*, vol. 106, no. 16, p. 162904, 2015.

[12] C.-J. Eklund, C. Fennie, and K. Rabe, "Strain-induced ferroelectricity in orthorhombic $CaTiO_3$ from first principles," *Physical Review B*, vol. 79, no. 22, p. 220101, 2009.

[13] X. Liu, D. Choudhury, Y. Cao, M. Kareev, S. Middey, and J. Chakhalian, "Metallic interface in non-$SrTiO_3$ based titanate superlattice," *Applied Physics Letters*, vol. 107, no. 19, p. 191602, 2015.

[14] S. Muff, M. Fanciulli, A. P. Weber, N. Pilet, Z. Ristić, Z. Wang, N. C. Plumb, M. Radović, and J. H. Dil, "Observation of a two-dimensional electron gas at $CaTiO_3$ film surfaces," *Applied Surface Science*, vol. 432, pp. 41–45, 2018.

[15] J. Mannhart and D. Schlom, "Oxide interfaces - an opportunity for electronics," *Science*, vol. 327, no. 5973, pp. 1607–1611, 2010.

[16] N. Shanthi and D. Sarma, "Electronic structure of electron doped $SrTiO_3$: $SrTiO_{3-\delta}$ and $Sr_{1-x}La_xTiO_3$," *Physical Review B*, vol. 57, no. 4, p. 2153, 1998.

[17] H. Frederikse, W. Thurber, and W. Hosler, "Electronic transport in strontium titanate," *Physical Review*, vol. 134, no. 2A, p. A442, 1964.

[18] J. Schooley, W. Hosler, and M. L. Cohen, "Superconductivity in semiconducting $SrTiO_3$," *Physical Review Letters*, vol. 12, no. 17, p. 474, 1964.

[19] G. Koster, B. L. Kropman, G. J. Rijnders, D. H. Blank, and H. Rogalla, "Quasi-ideal strontium titanate crystal surfaces through formation of strontium hydroxide," *Applied Physics Letters*, vol. 73, no. 20, pp. 2920–2922, 1998.

[20] M. Kawasaki, K. Takahashi, T. Maeda, R. Tsuchiya, M. Shinohara, O. Ishiyama, T. Yonezawa, M. Yoshimoto, and H. Koinuma, "Atomic control of the $SrTiO_3$ crystal surface," *Science*, vol. 266, no. 5190, pp. 1540–1542, 1994.

[21] M. Kareev, S. Prosandeev, J. Liu, C. Gan, A. Kareev, J. Freeland, M. Xiao, and J. Chakhalian, "Atomic control and characterization of surface defect states of TiO_2 terminated srtio$_3$ single crystals," *Applied Physics Letters*, vol. 93, no. 6, p. 061909, 2008.

[22] J. Nishimura, A. Ohtomo, A. Ohkubo, Y. Murakami, and M. Kawasaki, "Controlled carrier generation at a polarity-discontinued perovskite heterointerface," *Japanese journal of applied physics*, vol. 43, no. 8A, p. L1032, 2004.

[23] P. Perna, D. Maccariello, M. Radovic, U. Scotti di Uccio, I. Pallecchi, M. Codda, D. Marré, C. Cantoni, J. Gazquez, M. Varela, *et al.*, "Conducting interfaces between band insulating oxides: The $LaGaO_3/SrTiO_3$ heterostructure," *Applied Physics Letters*, vol. 97, no. 15, p. 152111, 2010.

[24] Y. Hotta, T. Susaki, and H. Hwang, "Polar discontinuity doping of the $LaVO_3/SrTiO_3$ interface," *Physical review letters*, vol. 99, no. 23, p. 236805, 2007.

[25] J. Biscaras, N. Bergeal, A. Kushwaha, T. Wolf, A. Rastogi, R. C. Budhani, and J. Lesueur, "Two-dimensional superconductivity at a mott insulator/band insulator interface $LaTiO_3/SrTiO_3$," *Nature communications*, vol. 1, p. 89, 2010.

[26] Z. Huang, K. Han, S. Zeng, M. Motapothula, A. Y. Borisevich, S. Ghosh, W. Lu, C. Li, W. Zhou, Z. Liu, *et al.*, "The effect of polar fluctuation and lattice mismatch on carrier mobility at oxide interfaces," *Nano letters*, vol. 16, no. 4, pp. 2307–2313, 2016.

[27] P. Moetakef, T. A. Cain, D. G. Ouellette, J. Y. Zhang, D. O. Klenov, A. Janotti, C. G. Van de Walle, S. Rajan, S. J. Allen, and S. Stemmer, "Electrostatic carrier doping of $GdTiO_3/SrTiO_3$ interfaces," *Applied Physics Letters*, vol. 99, no. 23, p. 232116, 2011.

[28] Y. Chen, F. Trier, T. Kasama, D. V. Christensen, N. Bovet, Z. I. Balogh, H. Li, K. T. S. Thydén, W. Zhang, S. Yazdi, *et al.*, "Creation of high mobility two-dimensional electron gases via strain induced polarization at an otherwise nonpolar complex oxide interface," *Nano letters*, vol. 15, no. 3, pp. 1849–1854, 2015.

[29] Y. Chen, N. Bovet, F. Trier, D. Christensen, F. Qu, N. H. Andersen, T. Kasama, W. Zhang, R. Giraud, J. Dufouleur, *et al.*, "A high-mobility two-dimensional electron gas at the

spinel/perovskite interface of γ-Al$_2$O$_3$/SrTiO$_3$," *Nature communications*, vol. 4, p. 1371, 2013.

[30] D. V. Christensen, Y. Frenkel, P. Schütz, F. Trier, S. Wissberg, R. Claessen, B. Kalisky, A. Smith, Y. Chen, and N. Pryds, "Electron mobility in γ-Al$_2$O$_3$/SrTiO$_3$," *Physical Review Applied*, vol. 9, no. 5, p. 054004, 2018.

[31] C. A. Jackson and S. Stemmer, "Interface-induced magnetism in perovskite quantum wells," *Physical Review B*, vol. 88, no. 18, p. 180403, 2013.

[32] P. King, R. He, T. Eknapakul, P. Buaphet, S.-K. Mo, Y. Kaneko, S. Harashima, Y. Hikita, M. Bahramy, C. Bell, *et al.*, "Subband structure of a two-dimensional electron gas formed at the polar surface of the strong spin-orbit perovskite KTaO$_3$," *Physical review letters*, vol. 108, no. 11, p. 117602, 2012.

[33] C. Jia, S. Mi, M. Faley, U. Poppe, J. Schubert, and K. Urban, "Oxygen octahedron reconstruction in the SrTiO$_3$/LaAlO$_3$ heterointerfaces investigated using aberration-corrected ultrahigh-resolution transmission electron microscopy," *Physical Review B*, vol. 79, no. 8, p. 081405, 2009.

[34] J.-L. Maurice, C. Carrétéro, M.-J. Casanove, K. Bouzehouane, S. Guyard, É. Larquet, and J.-P. Contour, "Electronic conductivity and structural distortion at the interface between insulators SrTiO$_3$ and LaAlO$_3$," *physica status solidi (a)*, vol. 203, no. 9, pp. 2209–2214, 2006.

[35] V. Vonk, M. Huijben, K. Driessen, P. Tinnemans, A. Brinkman, S. Harkema, and H. Graafsma, "Interface structure of SrTiO$_3$/LaAlO$_3$ at elevated temperatures studied in situ by synchrotron x rays," *Physical Review B*, vol. 75, no. 23, p. 235417, 2007.

[36] M. Huijben, G. Rijnders, D. H. Blank, S. Bals, S. Van Aert, J. Verbeeck, G. Van Tendeloo, A. Brinkman, and H. Hilgenkamp, "Electronically coupled complementary interfaces between perovskite band insulators," *Nature materials*, vol. 5, no. 7, p. 556, 2006.

[37] R. Pentcheva, M. Huijben, K. Otte, W. E. Pickett, J. Kleibeuker, J. Huijben, H. Boschker, D. Kockmann, W. Siemons, G. Koster, *et al.*, "Parallel electron-hole bilayer conductivity from electronic interface reconstruction," *Physical review letters*, vol. 104, no. 16, p. 166804, 2010.

[38] Z. S. Popović, S. Satpathy, and R. M. Martin, "Origin of the two-dimensional electron gas carrier density at the $LaAlO_3$ on $SrTiO_3$ interface," *Physical review letters*, vol. 101, no. 25, p. 256801, 2008.

[39] R. Pentcheva and W. E. Pickett, "Electronic phenomena at complex oxide interfaces: insights from first principles," *Journal of Physics: Condensed Matter*, vol. 22, no. 4, p. 043001, 2010.

[40] P. Delugas, A. Filippetti, V. Fiorentini, D. I. Bilc, D. Fontaine, and P. Ghosez, "Spontaneous 2-dimensional carrier confinement at the n-type $SrTiO_3/LaAlO_3$ interface," *Physical review letters*, vol. 106, no. 16, p. 166807, 2011.

[41] S. Thiel, G. Hammerl, A. Schmehl, C. Schneider, and J. Mannhart, "Tunable quasi-two-dimensional electron gases in oxide heterostructures," *Science*, vol. 313, no. 5795, pp. 1942–1945, 2006.

[42] A. Kalabukhov, R. Gunnarsson, J. Börjesson, E. Olsson, T. Claeson, and D. Winkler, "Effect of oxygen vacancies in the $SrTiO_3$ substrate on the electrical properties of the $LaAlO_3/SrTiO_3$ interface," *Physical Review B*, vol. 75, no. 12, p. 121404, 2007.

[43] W. Siemons, G. Koster, H. Yamamoto, W. A. Harrison, G. Lucovsky, T. H. Geballe, D. H. Blank, and M. R. Beasley, "Origin of charge density at laalo$_3$ on srtio$_3$ heterointerfaces: Possibility of intrinsic doping," *Physical review letters*, vol. 98, no. 19, p. 196802, 2007.

[44] M. Basletic, J.-L. Maurice, C. Carrétéro, G. Herranz, O. Copie, M. Bibes, É. Jacquet, K. Bouzehouane, S. Fusil, and A. Barthélémy, "Mapping the spatial distribution of charge carriers in LaAlO$_3$/SrTiO$_3$ heterostructures," *Nature materials*, vol. 7, no. 8, p. 621, 2008.

[45] Y. Chen, "13 - high-mobility two-dimensional electron gases at complex oxide interfaces," in *Metal Oxide-Based Thin Film Structures* (N. Pryds and V. Esposito, eds.), Metal Oxides, pp. 283 – 300, Elsevier, 2018.

[46] M. Warusawithana, C. Richter, J. Mundy, P. Roy, J. Ludwig, S. Paetel, T. Heeg, A. Pawlicki, L. Kourkoutis, M. Zheng, *et al.*, "LaAlO$_3$ stoichiometry is key to electron liquid formation at LaAlO$_3$/SrTiO$_3$ interfaces," *Nature communications*, vol. 4, p. 2351, 2013.

[47] G. Herranz, F. Sánchez, N. Dix, M. Scigaj, and J. Fontcuberta, "High mobility conduction at (110) and (111) LaAlO$_3$/SrTiO$_3$ interfaces," *Scientific reports*, vol. 2, p. 758, 2012.

[48] C. Cancellieri, N. Reyren, S. Gariglio, A. Caviglia, A. Fête, and J.-M. Triscone, "Influence of the growth conditions on the LaAlO$_3$/SrTiO$_3$ interface electronic properties," *EPL (Europhysics Letters)*, vol. 91, no. 1, p. 17004, 2010.

[49] L. Yu and A. Zunger, "A polarity-induced defect mechanism for conductivity and magnetism at polar–nonpolar oxide interfaces," *Nature communications*, vol. 5, p. 5118, 2014.

[50] A. Santander-Syro, O. Copie, T. Kondo, F. Fortuna, S. Pail-hes, R. Weht, X. Qiu, F. Bertran, A. Nicolaou, A. Taleb-Ibrahimi, *et al.*, "Two-dimensional electron gas with universal subbands at the surface of SrTiO$_3$," *Nature*, vol. 469, no. 7329, p. 189, 2011.

[51] F. Y. Bruno, J. Tornos, M. G. Del Olmo, G. S. Santolino, N. Nemes, M. Garcia-Hernandez, B. Mendez, J. Piqueras, G. Antorrena, L. Morellón, *et al.*, "Anisotropic magnetotrans-port in SrTiO$_3$ surface electron gases generated by Ar$^+$ irra-diation," *Physical Review B*, vol. 83, no. 24, p. 245120, 2011.

[52] S. M. Walker, A. De La Torre, F. Y. Bruno, A. Tamai, T. Kim, M. Hoesch, M. Shi, M. Bahramy, P. King, and F. Baumberger, "Control of a two-dimensional electron gas on SrTiO$_3$ (111) by atomic oxygen," *Physical review letters*, vol. 113, no. 17, p. 177601, 2014.

[53] M. Zhang, Z. Chen, B. Mao, Q. Li, H. Bo, T. Ren, P. He, Z. Liu, and Y. Xie, "Origin of interfacial conductivity at com-plex oxide heterointerfaces: Possibility of electron transfer from water chemistry at surface oxygen vacancies," *Physical Review Materials*, vol. 2, no. 6, p. 065002, 2018.

[54] K. A. Brown, S. He, D. J. Eichelsdoerfer, M. Huang, I. Levy, H. Lee, S. Ryu, P. Irvin, J. Mendez-Arroyo, C.-B. Eom, *et al.*, "Giant conductivity switching of LaAlO$_3$/SrTiO$_3$ heterointer-faces governed by surface protonation," *Nature communica-tions*, vol. 7, p. 10681, 2016.

[55] N. Bristowe, P. Littlewood, and E. Artacho, "Surface defects and conduction in polar oxide heterostructures," *Physical Re-view B*, vol. 83, no. 20, p. 205405, 2011.

[56] L. Qiao, T. C. Droubay, T. Varga, M. E. Bowden, V. Shut-thanandan, Z. Zhu, T. C. Kaspar, and S. A. Cham-bers, "Epitaxial growth, structure, and intermixing at the

LaAlO$_3$/SrTiO$_3$ interface as the film stoichiometry is varied," *Physical Review B*, vol. 83, no. 8, p. 085408, 2011.

[57] N. Nakagawa, H. Y. Hwang, and D. A. Muller, "Why some interfaces cannot be sharp," *Nature materials*, vol. 5, no. 3, p. 204, 2006.

[58] P. Willmott, S. Pauli, R. Herger, C. Schlepütz, D. Martoccia, B. Patterson, B. Delley, R. Clarke, D. Kumah, C. Cionca, *et al.*, "Structural basis for the conducting interface between LaAlO$_3$ and SrTiO$_3$," *Physical Review Letters*, vol. 99, no. 15, p. 155502, 2007.

[59] M. Imada, A. Fujimori, and Y. Tokura, "Metal-insulator transitions," *Reviews of modern physics*, vol. 70, no. 4, p. 1039, 1998.

[60] K. Ueno, S. Nakamura, H. Shimotani, A. Ohtomo, N. Kimura, T. Nojima, H. Aoki, Y. Iwasa, and M. Kawasaki, "Electric-field-induced superconductivity in an insulator," *Nature materials*, vol. 7, no. 11, p. 855, 2008.

[61] H. Nakamura, H. Tomita, H. Akimoto, R. Matsumura, I. H. Inoue, T. Hasegawa, K. Kono, Y. Tokura, and H. Takagi, "Tuning of metal-insulator transition of quasi-two-dimensional electrons at Parylene/SrTiO$_3$ interface by electric field," *Journal of the Physical Society of Japan*, vol. 78, no. 8, pp. 083713–083713, 2009.

[62] N. Reyren, S. Thiel, A. Caviglia, L. F. Kourkoutis, G. Hammerl, C. Richter, C. Schneider, T. Kopp, A.-S. Rüetschi, D. Jaccard, *et al.*, "Superconducting interfaces between insulating oxides," *Science*, vol. 317, no. 5842, pp. 1196–1199, 2007.

[63] A. Caviglia, S. Gariglio, N. Reyren, D. Jaccard, T. Schneider, M. Gabay, S. Thiel, G. Hammerl, J. Mannhart, and J.-M.

Triscone, "Electric field control of the $LaAlO_3$/$SrTiO_3$ interface ground state," *Nature*, vol. 456, no. 7222, p. 624, 2008.

[64] S. Goswami, E. Mulazimoglu, L. M. Vandersypen, and A. D. Caviglia, "Nanoscale electrostatic control of oxide interfaces," *Nano letters*, vol. 15, no. 4, pp. 2627–2632, 2015.

[65] J. Jeong, N. Aetukuri, T. Graf, T. D. Schladt, M. G. Samant, and S. S. Parkin, "Suppression of metal-insulator transition in VO_2 by electric field-induced oxygen vacancy formation," *Science*, vol. 339, no. 6126, pp. 1402–1405, 2013.

[66] H. Ohta, T. Mizuno, S. Zheng, T. Kato, Y. Ikuhara, K. Abe, H. Kumomi, K. Nomura, and H. Hosono, "Unusually large enhancement of thermopower in an electric field induced two-dimensional electron gas," *Advanced Materials*, vol. 24, no. 6, pp. 740–744, 2012.

[67] M. Dresselhaus, G. Dresselhaus, X. Sun, Z. Zhang, S. Cronin, and T. Koga, "Low-dimensional thermoelectric materials," *Physics of the Solid State*, vol. 41, no. 5, pp. 679–682, 1999.

[68] M. S. Dresselhaus, G. Chen, M. Y. Tang, R. Yang, H. Lee, D. Wang, Z. Ren, J.-P. Fleurial, and P. Gogna, "New directions for low-dimensional thermoelectric materials," *Advanced materials*, vol. 19, no. 8, pp. 1043–1053, 2007.

[69] I. Pallecchi, F. Telesio, D. Marré, D. Li, S. Gariglio, J.-M. Triscone, and A. Filippetti, "Large phonon-drag enhancement induced by narrow quantum confinement at the $LaAlO_3$/$SrTiO_3$ interface," *Physical Review B*, vol. 93, no. 19, p. 195309, 2016.

[70] J. M. Ziman, *Principles of the Theory of Solids*. Cambridge university press, 1979.

[71] J. M. Ziman, *Electrons and phonons: the theory of transport phenomena in solids*. Oxford university press, 2001.

[72] R. R. Heikes and R. W. Ure, *Thermoelectricity: science and engineering.* Interscience Publishers, 1961.

[73] W. Koshibae and S. Maekawa, "Effects of spin and orbital degeneracy on the thermopower of strongly correlated systems," *Physical review letters*, vol. 87, no. 23, p. 236603, 2001.

[74] T. M. Tritt, *Thermal conductivity: theory, properties, and applications.* Springer Science & Business Media, 2005.

[75] D. T. Morelli and G. A. Slack, "High lattice thermal conductivity solids," in *High Thermal Conductivity Materials*, pp. 37–68, Springer, 2006.

[76] G. A. Slack and S. Galginaitis, "Thermal conductivity and phonon scattering by magnetic impurities in CdTe," *Physical Review*, vol. 133, no. 1A, p. A253, 1964.

[77] P. Klemens, "The scattering of low-frequency lattice waves by static imperfections," *Proceedings of the Physical Society. Section A*, vol. 68, no. 12, p. 1113, 1955.

[78] J. B. Goodenough and J.-S. Zhou, "Localized to itinerant electronic transitions in transition-metal oxides with the perovskite structure," *Chemistry of Materials*, vol. 10, no. 10, pp. 2980–2993, 1998.

[79] http://abulafia.mt.ic.ac.uk/shannon/.

[80] C. Randall, A. Bhalla, T. Shrout, and L. Cross, "Classification and consequences of complex lead perovskite ferroelectrics with regard to B-site cation order," *Journal of Materials Research*, vol. 5, no. 4, pp. 829–834, 1990.

[81] S. Pei, J. Jorgensen, B. Dabrowski, D. Hinks, D. Richards, A. Mitchell, J. Newsam, S. Sinha, D. Vaknin, and A. Jacobson, "Structural phase diagram of the $Ba_{1-x}K_xBiO_3$ system," *Physical Review B*, vol. 41, no. 7, p. 4126, 1990.

[82] J. M. Rondinelli and N. A. Spaldin, "Electron-lattice instabilities suppress cuprate-like electronic structures in $SrFeO_3/SrTiO_3$ superlattices," *Physical Review B*, vol. 81, no. 8, p. 085109, 2010.

[83] Y. Wang, Y. Sui, P. Ren, L. Wang, X. Wang, W. Su, and H. J. Fan, "Correlation between the structural distortions and thermoelectric characteristics in $La_{1-x}A_xCoO_3$ (A= Ca and Sr)," *Inorganic chemistry*, vol. 49, no. 7, pp. 3216–3223, 2010.

[84] A. Millis, "Lattice effects in magnetoresistive manganese perovskites," *Nature*, vol. 392, no. 6672, p. 147, 1998.

[85] A. Vailionis, H. Boschker, W. Siemons, E. P. Houwman, D. H. Blank, G. Rijnders, and G. Koster, "Misfit strain accommodation in epitaxial ABO_3 perovskites: Lattice rotations and lattice modulations," *Physical Review B*, vol. 83, no. 6, p. 064101, 2011.

[86] W. Lu, W. Song, P. Yang, J. Ding, G. M. Chow, and J. Chen, "Strain engineering of octahedral rotations and physical properties of $SrRuO_3$ films," *Scientific reports*, vol. 5, 2015.

[87] J. M. Rondinelli and N. A. Spaldin, "Structure and properties of functional oxide thin films: insights from electronic-structure calculations," *Advanced Materials*, vol. 23, no. 30, pp. 3363–3381, 2011.

[88] S. May, J.-W. Kim, J. Rondinelli, E. Karapetrova, N. Spaldin, A. Bhattacharya, and P. Ryan, "Quantifying octahedral rotations in strained perovskite oxide films," *Physical Review B*, vol. 82, no. 1, p. 014110, 2010.

[89] A. Glazer, "The classification of tilted octahedra in perovskites," *Acta Crystallographica Section B: Structural Crystallography and Crystal Chemistry*, vol. 28, no. 11, pp. 3384–3392, 1972.

[90] A. Glazer, "Simple ways of determining perovskite structures," *Acta Crystallographica Section A: Crystal Physics, Diffraction, Theoretical and General Crystallography*, vol. 31, no. 6, pp. 756–762, 1975.

[91] P. M. Woodward, "Octahedral tilting in perovskites. I. Geometrical considerations," *Acta Crystallographica Section B*, vol. 53, no. 1, pp. 32–43, 1997.

[92] P. M. Woodward, "Octahedral tilting in perovskites. II. Structure stabilizing forces," *Acta Crystallographica Section B*, vol. 53, no. 1, pp. 44–66, 1997.

[93] D. Dijkkamp, T. Venkatesan, X. Wu, S. Shaheen, N. Jisrawi, Y. Min-Lee, W. McLean, and M. Croft, "Preparation of Y-Ba-Cu oxide superconductor thin films using pulsed laser evaporation from high T_c bulk material," *Applied Physics Letters*, vol. 51, no. 8, pp. 619–621, 1987.

[94] D. Schlom, J. Eckstein, E. Hellman, S. Streiffer, J. Harris Jr, M. Beasley, J. Bravman, T. Geballe, C. Webb, K. Von Dessonneck, *et al.*, "Molecular beam epitaxy of layered Dy-Ba-Cu-O compounds," *Applied physics letters*, vol. 53, no. 17, pp. 1660–1662, 1988.

[95] E. Kay, "Impact evaporation and thin film growth in a glow discharge," in *Advances in Electronics and Electron Physics*, vol. 17, pp. 245–322, Elsevier, 1963.

[96] R. W. Schwartz, T. Schneller, and R. Waser, "Chemical solution deposition of electronic oxide films," *Comptes Rendus Chimie*, vol. 7, no. 5, pp. 433 – 461, 2004.

[97] E. Breckenfeld, R. Wilson, J. Karthik, A. R. Damodaran, D. G. Cahill, and L. W. Martin, "Effect of growth induced (non)stoichiometry on the structure, dielectric response, and thermal conductivity of $SrTiO_3$ thin films," *Chemistry of Materials*, vol. 24, no. 2, pp. 331–337, 2012.

[98] D. J. Keeble, S. Wicklein, L. Jin, C. L. Jia, W. Egger, and R. Dittmann, "Nonstoichiometry accommodation in SrTiO$_3$ thin films studied by positron annihilation and electron microscopy," *Phys. Rev. B*, vol. 87, p. 195409, May 2013.

[99] A. Biswas, C.-H. Yang, R. Ramesh, and Y. H. Jeong, "Atomically flat single terminated oxide substrate surfaces," *Progress in Surface Science*, vol. 92, no. 2, pp. 117–141, 2017.

[100] M. Kareev, S. Prosandeev, J. Liu, C. Gan, A. Kareev, J. W. Freeland, M. Xiao, and J. Chakhalian, "Atomic control and characterization of surface defect states of TiO$_2$ terminated SrTiO$_3$ single crystals," *Applied Physics Letters*, vol. 93, no. 6, p. 061909, 2008.

[101] M. Birkholz, *Thin film analysis by X-ray scattering*. John Wiley & Sons, 2006.

[102] J. M. Rondinelli, S. J. May, and J. W. Freeland, "Control of octahedral connectivity in perovskite oxide heterostructures: An emerging route to multifunctional materials discovery," *MRS bulletin*, vol. 37, no. 3, pp. 261–270, 2012.

[103] N. A. Benedek, A. T. Mulder, and C. J. Fennie, "Polar octahedral rotations: a path to new multifunctional materials," *Journal of Solid State Chemistry*, vol. 195, pp. 11–20, 2012.

[104] E. Moon, R. Colby, Q. Wang, E. Karapetrova, C. Schlepütz, M. Fitzsimmons, and S. J. May, "Spatial control of functional properties via octahedral modulations in complex oxide superlattices," *Nature communications*, vol. 5, p. 5710, 2014.

[105] E. Bousquet, M. Dawber, N. Stucki, C. Lichtensteiger, P. Hermet, S. Gariglio, J.-M. Triscone, and P. Ghosez, "Improper ferroelectricity in perovskite oxide artificial superlattices," *Nature*, vol. 452, no. 7188, p. 732, 2008.

[106] G. Binnig, C. F. Quate, and C. Gerber, "Atomic force microscope," *Physical review letters*, vol. 56, no. 9, p. 930, 1986.

[107] ParkSystems, *NX10 User's Manual*, 2016.

[108] P. Girard, "Electrostatic force microscopy: principles and some applications to semiconductors," *Nanotechnology*, vol. 12, no. 4, p. 485, 2001.

[109] ParkSystems, *Electrostatic Force Microscopy (EFM)*, 2016.

[110] L. Van der Pauw, "A method of measuring specific resistivity and Hall effect of discs of arbitrary shape," *Philips research reports*, vol. 13, pp. 1–9, 1958.

[111] A. J. Schmidt, R. Cheaito, and M. Chiesa, "A frequency-domain thermoreflectance method for the characterization of thermal properties," *Review of scientific instruments*, vol. 80, no. 9, p. 094901, 2009.

[112] J. A. Malen, K. Baheti, T. Tong, Y. Zhao, J. A. Hudgings, and A. Majumdar, "Optical measurement of thermal conductivity using fiber aligned frequency domain thermoreflectance," *Journal of Heat Transfer*, vol. 133, no. 8, p. 081601, 2011.

[113] D. G. Cahill, "Analysis of heat flow in layered structures for time-domain thermoreflectance," *Review of scientific instruments*, vol. 75, no. 12, pp. 5119–5122, 2004.

[114] D. G. Cahill and R. O. Pohl, "Thermal conductivity of amorphous solids above the plateau," *Physical review B*, vol. 35, no. 8, p. 4067, 1987.

[115] D. G. Cahill, M. Katiyar, and J. Abelson, "Thermal conductivity of a-Si:H thin films," *Physical review B*, vol. 50, no. 9, p. 6077, 1994.

[116] C. López-Bueno, D. Bugallo, V. Leborán, and F. Rivadulla, "Sub-μL measurements of the thermal conductivity and heat capacity of liquids," *Physical Chemistry Chemical Physics*, vol. 20, no. 10, pp. 7277–7281, 2018.

[117] A. Brinkman, M. Huijben, M. van Zalk, J. Huijben, U. Zeitler, J. C. Maan, W. G. van der Wiel, G. Rijnders, D. Blank, and H. Hilgenkamp, "Magnetic effects at the interface between non-magnetic oxides," *Nat. Mat.*, vol. 6, pp. 493–496, Jul 2007.

[118] T. Ohnishi, M. Lippmaa, T. Yamamoto, S. Meguro, and H. Koinuma, "Improved stoichiometry and misfit control in perovskite thin film formation at a critical fluence by pulsed laser deposition," *Applied Physics Letters*, vol. 87, no. 24, pp. –, 2005.

[119] D. Keeble, S. Wicklein, R. Dittmann, L. Ravelli, R. Mackie, and W. Egger, "Identification of *A*- and *B*-site cation vacancy defects in perovskite oxide thin films," *Phys. Rev. Lett.*, vol. 105, p. 226102, Nov 2010.

[120] Y. Kozuka, Y. Hikita, C. Bell, and H. Y. Hwang, "Dramatic mobility enhancements in doped $SrTiO_3$ thin films by defect management," *Applied Physics Letters*, vol. 97, no. 1, pp. –, 2010.

[121] S. Wicklein, A. Sambri, S. Amoruso, X. Wang, R. Bruzzese, A. Koehl, and R. Dittmann, "Pulsed laser ablation of complex oxides: The role of congruent ablation and preferential scattering for the film stoichiometry," *Applied Physics Letters*, vol. 101, no. 13, pp. –, 2012.

[122] E. Breckenfeld, A. B. Shah, and L. W. Martin, "Strain evolution in non-stoichiometric heteroepitaxial thin-film perovskites," *J. Mater. Chem. C*, vol. 1, pp. 8052–8059, 2013.

[123] Y. Tokuda, S. Kobayashi, T. Ohnishi, T. Mizoguchi, N. Shibata, Y. Ikuhara, and T. Yamamoto, "Strontium vacancy clustering in Ti-excess $SrTiO_3$ thin film," *Applied Physics Letters*, vol. 99, no. 3, p. 033110, 2011.

[124] C. Xu, S. Wicklein, A. Sambri, S. Amoruso, M. Moors, and R. Dittmann, "Impact of the interplay between nonstoichiometry and kinetic energy of the plume species on the growth mode of $SrTiO_3$ thin films," *Journal of Physics D: Applied Physics*, vol. 47, no. 3, p. 034009, 2013.

[125] U. Aschauer, R. Pfenninger, S. M. Selbach, T. Grande, and N. A. Spaldin, "Strain-controlled oxygen vacancy formation and ordering in $CaMnO_3$," *Phys. Rev. B*, vol. 88, p. 054111, Aug 2013.

[126] S. Kobayashi, Y. Tokuda, T. Ohnishi, T. Mizoguchi, N. Shibata, Y. Sato, Y. Ikuhara, and T. Yamamoto, "Cation off-stoichiometric $SrMnO_{3-\delta}$ thin film grown by pulsed laser deposition," *Journal of Materials Science*, vol. 46, no. 12, pp. 4354–4360, 2011.

[127] J.-P. Maria, S. Trolier-McKinstry, D. G. Schlom, M. E. Hawley, and G. W. Brown, "The influence of energetic bombardment on the structure and properties of epitaxial $SrRuO_3$ thin films grown by pulsed laser deposition," *Journal of Applied Physics*, vol. 83, no. 8, pp. 4373–4379, 1998.

[128] A. R. Damodaran, E. Breckenfeld, Z. Chen, S. Lee, and L. W. Martin, "Enhancement of ferroelectric Curie temperature in $BaTiO_3$ films via strain-induced defect dipole alignment," *Advanced Materials*, vol. 26, no. 36, pp. 6341–6347, 2014.

[129] C. M. Brooks, L. F. Kourkoutis, T. Heeg, J. Schubert, D. A. Muller, and D. G. Schlom, "Growth of homoepitaxial $SrTiO_3$ thin films by molecular-beam epitaxy," *Applied Physics Letters*, vol. 94, no. 16, pp. –, 2009.

173

[130] J. Ravichandran, W. Siemons, M. L. Scullin, S. Mukerjee, M. Huijben, J. E. Moore, A. Majumdar, and R. Ramesh, "Tuning the electronic effective mass in double-doped $SrTiO_3$," *Phys. Rev. B*, vol. 83, p. 035101, Jan 2011.

[131] H. Ledbetter, M. Lei, and S. Kim, "Elastic constants, Debye temperatures, and electron-phonon parameters of superconducting cuprates and related oxides," *Phase Transitions: A Multinational Journal*, vol. 23, no. 1, pp. 61–70, 1990.

[132] M. Foerster, M. Iliev, N. Dix, X. Martí, M. Barchuk, F. Sánchez, and J. Fontcuberta, "The poisson ratio in $CoFe_2O_4$ spinel thin films," *Advanced Functional Materials*, vol. 22, no. 20, pp. 4344–4351, 2012.

[133] T. Tanaka, K. Matsunaga, Y. Ikuhara, and T. Yamamoto, "First-principles study on structures and energetics of intrinsic vacancies in $SrTiO_3$," *Phys. Rev. B*, vol. 68, p. 205213, Nov 2003.

[134] A. Joshua, S. Pecker, J. Ruhman, E. Altman, and S. Ilani, "A universal critical density underlying the physics of electrons at the $LaAlO_3/SrTiO_3$ interface," *Nat. Commun.*, vol. 3, p. 1129, 2012.

[135] M. Ben Shalom, A. Ron, A. Palevski, and Y. Dagan, "Shubnikov–de Haas oscillations in $SrTiO_3/LaAlO_3$ interface," *Phys. Rev. Lett.*, vol. 105, p. 206401, Nov 2010.

[136] M. Lee, J. Williams, S. Zhang, C. Frisbie, and D. Goldhaber-Gordon, "Electrolyte gate-controlled Kondo effect in $SrTiO_3$," *Phys. Rev. Lett.*, vol. 107, p. 256601, Dec 2011.

[137] M. Li, T. Graf, T. Schladt, X. Jiang, and S. Parkin, "Role of percolation in the conductance of electrolyte-gated $SrTiO_3$," *Phys. Rev. Lett.*, vol. 109, p. 196803, Nov 2012.

[138] M. Ben Shalom, M. Sachs, D. Rakhmilevitch, A. Palevski, and Y. Dagan, "Tuning spin-orbit coupling and superconductivity at the $SrTiO_3/LaAlO_3$ interface: A magnetotransport study," *Phys. Rev. Lett.*, vol. 104, p. 126802, Mar 2010.

[139] A. F. Santander-Syro, F. Fortuna, C. Bareille, T. C. Rödel, G. Landolt, N. C. Plumb, J. H. Dil, and M. Radović, "Giant spin splitting of the two-dimensional electron gas at the surface of $SrTiO_3$," *Nature*, vol. 13, p. 1085, Oct 2010.

[140] S. Seri and L. Klein, "Antisymmetric magnetoresistance of the $SrTiO_3/LaALO_3$ interface," *Phys. Rev. B*, vol. 80, p. 180410, Nov 2009.

[141] M. Ben Shalom, C. W. Tai, Y. Lereah, M. Sachs, E. Levy, D. Rakhmilevitch, A. Palevski, and Y. Dagan, "Anisotropic magnetotransport at the $SrTiO_3/LaAlO_3$ interface," *Phys. Rev. B*, vol. 80, p. 140403, Oct 2009.

[142] A. D. Caviglia, S. Gariglio, C. Cancellieri, B. Sacépé, A. Fête, N. Reyren, M. Gabay, A. F. Morpurgo, and J.-M. Triscone, "Two-dimensional quantum oscillations of the conductance at $LaALO_3/SrTiO_3$ interfaces," *Phys. Rev. Lett.*, vol. 105, p. 236802, Dec 2010.

[143] T. Okuda, K. Nakanishi, S. Miyasaka, and Y. Tokura, "Large thermoelectric response of metallic perovskites: $Sr_{1-x}La_xTiO_3$," *Phys. Rev. B*, vol. 63, p. 113104, Mar 2001.

[144] B. Jalan, S. Stemmer, S. Mack, and S. J. Allen, "Two-dimensional electron gas in δ-doped $SrTiO_3$," *Phys. Rev. B*, vol. 82, p. 081103, Aug 2010.

[145] P. Hohenberg and W. Kohn, "Inhomogeneous electron gas," *Phys. Rev.*, vol. 136, p. B864, 1964.

[146] R. O. Jones and O. Gunnarsson, "The density functional formalism, its applications and prospects," *Rev. Mod. Phys.*, vol. 61, p. 689, 1989.

[147] P. Fazekas, *Lecture Notes on Electron Correlation and Magnetism.* London: World Scientific, 1999.

[148] H. Uwe and T. Sakudo, "Stress-induced ferroelectricity and soft phonon modes in SrTiO$_3$," *Physical Review B*, vol. 13, no. 1, p. 271, 1976.

[149] C. Ang, Z. Yu, P. Vilarinho, and J. Baptista, "Bi:SrTiO$_3$: A quantum ferroelectric and a relaxor," *Physical Review B*, vol. 57, no. 13, p. 7403, 1998.

[150] J. Bednorz and K. Müller, "Sr$_{1-x}$Ca$_x$TiO$_3$: An XY Quantum Ferroelectric with Transition to Randomness," *Physical Review Letters*, vol. 52, no. 25, p. 2289, 1984.

[151] H. Jang, A. Kumar, S. Denev, M. D. Biegalski, P. Maksymovych, C. Bark, C. T. Nelson, C. Folkman, S. H. Baek, N. Balke, *et al.*, "Ferroelectricity in strain-free SrTiO$_3$ thin films," *Physical Review Letters*, vol. 104, no. 19, p. 197601, 2010.

[152] P. E. Hopkins, C. Adamo, L. Ye, B. D. Huey, S. R. Lee, D. G. Schlom, and J. F. Ihlefeld, "Effects of coherent ferroelastic domain walls on the thermal conductivity and Kapitza conductance in bismuth ferrite," *Applied Physics Letters*, vol. 102, no. 12, p. 121903, 2013.

[153] J. F. Ihlefeld, B. M. Foley, D. A. Scrymgeour, J. R. Michael, B. B. McKenzie, D. L. Medlin, M. Wallace, S. Trolier-McKinstry, and P. E. Hopkins, "Room-temperature voltage tunable phonon thermal conductivity via reconfigurable interfaces in ferroelectric thin films," *Nano letters*, vol. 15, no. 3, pp. 1791–1795, 2015.

[154] L. Iglesias, A. Sarantopoulos, C. Magén, and F. Rivadulla, "Oxygen vacancies in strained SrTiO$_3$ thin films: Formation enthalpy and manipulation," *Physical Review B*, vol. 95, no. 16, p. 165138, 2017.

[155] A. Yamanaka, M. Kataoka, Y. Inaba, K. Inoue, B. Hehlen, and E. Courtens, "Evidence for competing orderings in strontium titanate from hyper-Raman scattering spectroscopy," *EPL (Europhysics Letters)*, vol. 50, no. 5, p. 688, 2000.

[156] J. Haeni, P. Irvin, W. Chang, R. Uecker, P. Reiche, Y. Li, S. Choudhury, W. Tian, M. Hawley, B. Craigo, *et al.*, "Room-temperature ferroelectricity in strained SrTiO$_3$," *Nature*, vol. 430, no. 7001, p. 758, 2004.

[157] N. Pertsev, A. Tagantsev, and N. Setter, "Phase transitions and strain-induced ferroelectricity in SrTiO$_3$ epitaxial thin films," *Physical Review B*, vol. 61, no. 2, p. R825, 2000.

[158] C.-H. Lee, V. Skoromets, M. D. Biegalski, S. Lei, R. Haislmaier, M. Bernhagen, R. Uecker, X. Xi, V. Gopalan, X. Martí, *et al.*, "Effect of stoichiometry on the dielectric properties and soft mode behavior of strained epitaxial SrTiO$_3$ thin films on DyScO$_3$ substrates," *Applied Physics Letters*, vol. 102, no. 8, p. 082905, 2013.

[159] D. G. Cahill, H. E. Fischer, T. Klitsner, E. Swartz, and R. Pohl, "Thermal conductivity of thin films: Measurements and understanding," *Journal of Vacuum Science & Technology A: Vacuum, Surfaces, and Films*, vol. 7, no. 3, pp. 1259–1266, 1989.

[160] S.-M. Lee and D. G. Cahill, "Heat transport in thin dielectric films," *Journal of applied physics*, vol. 81, no. 6, pp. 2590–2595, 1997.

[161] D.-W. Oh, J. Ravichandran, C.-W. Liang, W. Siemons, B. Jalan, C. M. Brooks, M. Huijben, D. G. Schlom, S. Stemmer, L. W. Martin, *et al.*, "Thermal conductivity as a metric for the crystalline quality of SrTiO$_3$ epitaxial layers," *Applied Physics Letters*, vol. 98, no. 22, p. 221904, 2011.

[162] E. Breckenfeld, N. Bronn, J. Karthik, A. R. Damodaran, S. Lee, N. Mason, and L. W. Martin, "Effect of growth induced (non)stoichiometry on interfacial conductance in $LaAlO_3/SrTiO_3$," *Phys. Rev. Lett.*, vol. 110, p. 196804, May 2013.

[163] A. Beattie and G. Samara, "Pressure dependence of the elastic constants of $SrTiO_3$," *Journal of Applied Physics*, vol. 42, no. 6, pp. 2376–2381, 1971.

[164] R. Migoni, H. Bilz, and D. Bäuerle, "Origin of Raman scattering and ferroelectricity in oxidic perovskites," *Physical Review Letters*, vol. 37, no. 17, p. 1155, 1976.

[165] D. Nuzhnyy, J. Petzelt, S. Kamba, P. Kužel, C. Kadlec, V. Bovtun, M. Kempa, J. Schubert, C. Brooks, and D. Schlom, "Soft mode behavior in $SrTiO_3/DyScO_3$ thin films: Evidence of ferroelectric and antiferrodistortive phase transitions," *Applied physics letters*, vol. 95, no. 23, p. 232902, 2009.

[166] R. C. Haislmaier, E. D. Grimley, M. D. Biegalski, J. M. LeBeau, S. Trolier-McKinstry, V. Gopalan, and R. Engel-Herbert, "Unleashing strain induced ferroelectricity in complex oxide thin films via precise stoichiometry control," *Advanced Functional Materials*, vol. 26, no. 40, pp. 7271–7279, 2016.

[167] S. M. Yang, S. J. Moon, T. H. Kim, and Y. S. Kim, "Observation of ferroelectricity induced by defect dipoles in the strain-free epitaxial $CaTiO_3$ thin film," *Current Applied Physics*, vol. 14, no. 5, pp. 757–760, 2014.

[168] S. M. Nakhmanson, K. Rabe, and D. Vanderbilt, "Predicting polarization enhancement in multicomponent ferroelectric superlattices," *Physical Review B*, vol. 73, no. 6, p. 060101, 2006.

[169] D. Lee, H. Lu, Y. Gu, S. Y. Choi, S. D. Li, S. Ryu, T. R. Paudel, K. Song, E. Mikheev, S. Lee, S. Stemmer, D. A. Tenne, S. H. Oh, E. Y. Tsymbal, X. Wu, L. Q. Chen, A. Gruverman, and C. B. Eom, "Emergence of room-temperature ferroelectricity at reduced dimensions," *Science*, vol. 349, no. 6254, pp. 1314–1317, 2015.

[170] N. Balke, P. Maksymovych, S. Jesse, A. Herklotz, A. Tselev, C.-b. Eom, I. I. Kravchenko, P. Yu, and S. V. Kalinin, "Differentiating Ferroelectric and Effects with Scanning Probe Microscopy," *ACS Nano*, vol. 9, no. 6, pp. 6484–6492, 2015.

[171] M. Andrä, F. Gunkel, C. Bäumer, C. Xu, R. Dittmann, and R. Waser, "The influence of the local oxygen vacancy concentration on the piezoresponse of strontium titanate thin films," *Nanoscale*, vol. 7, no. 34, pp. 14351–14357, 2015.

[172] K. Regner, S. Majumdar, and J. A. Malen, "Instrumentation of broadband frequency domain thermoreflectance for measuring thermal conductivity accumulation functions," *Review of Scientific Instruments*, vol. 84, no. 6, p. 064901, 2013.

[173] A. Sarantopoulos, E. Ferreiro-Vila, V. Pardo, C. Magén, M. H. Aguirre, and F. Rivadulla, "Electronic degeneracy and intrinsic magnetic properties of epitaxial $Nb:SrTiO_3$ thin films controlled by defects," *Phys. Rev. Lett.*, vol. 115, p. 166801, Oct 2015.

[174] K. S. Knight, "Structural and thermoelastic properties of $CaTiO_3$ perovskite between 7 k and 400 k," *Journal of Alloys and Compounds*, vol. 509, no. 22, pp. 6337–6345, 2011.

[175] A. Boudali, A. Abada, M. D. Khodja, B. Amrani, K. Amara, F. D. Khodja, and A. Elias, "Calculation of structural, elastic, electronic, and thermal properties of orthorhombic $CaTiO_3$," *Physica B: Condensed Matter*, vol. 405, no. 18, pp. 3879–3884, 2010.

[176] T. C. Rödel, M. Vivek, F. Fortuna, P. Le Fèvre, F. Bertran, R. Weht, J. Goniakowski, M. Gabay, and A. F. Santander-Syro, "Two-dimensional electron systems in ATiO$_3$ perovskites (A= Ca, Ba, Sr): Control of orbital hybridization and energy order," *Physical Review B*, vol. 96, no. 4, p. 041121, 2017.

[177] E. Cockayne and B. P. Burton, "Phonons and static dielectric constant in CaTiO$_3$ from first principles," *Phys. Rev. B*, vol. 62, pp. 3735–3743, Aug 2000.

[178] L. Collins, A. Belianinov, S. Somnath, N. Balke, S. V. Kalinin, and S. Jesse, "Full data acquisition in Kelvin Probe Force Microscopy: Mapping dynamic electric phenomena in real space," *Scientific Reports*, vol. 6, no. 1, p. 30557, 2016.

[179] E. Rowicka, D. Kashyn, M. a. Reagan, T. Hirano, P. B. Paramonov, I. Dolog, R. R. Mallik, and S. F. Lyuksyutov, "Influence of Water Condensation on Charge transport and Electric Breakdown Between an Atomic Force Microscope Tip, Polymeric, and Semiconductor CdS Surfaces," *Current Nanoscience*, vol. 4, no. 2, p. 166, 2008.

[180] C. Bark, P. Sharma, Y. Wang, S. H. Baek, S. Lee, S. Ryu, C. Folkman, T. R. Paudel, A. Kumar, S. V. Kalinin, *et al.*, "Switchable induced polarization in LaAlO$_3$/SrTiO$_3$ heterostructures," *Nano letters*, vol. 12, no. 4, pp. 1765–1771, 2012.

[181] S. Das, B. Wang, Y. Cao, M. R. Cho, Y. J. Shin, S. M. Yang, L. Wang, M. Kim, S. V. Kalinin, L.-Q. Chen, *et al.*, "Controlled manipulation of oxygen vacancies using nanoscale flexoelectricity," *Nature Communications*, vol. 8, no. 1, p. 615, 2017.

[182] R. A. De Souza, V. Metlenko, D. Park, and T. E. Weirich, "Behavior of oxygen vacancies in single-crystal SrTiO$_3$: Equilibrium distribution and diffusion kinetics," *Physical Review*

B - Condensed Matter and Materials Physics, vol. 85, no. 17, pp. 1–11, 2012.

[183] P. Zubko, G. Catalan, and A. K. Tagantsev, "Flexoelectric effect in solids," *Annual Review of Materials Research*, vol. 43, no. 1, pp. 387–421, 2013.

[184] H. Carslaw and J. Jaeger, *Conduction of heat in solids: Oxford Science Publications*. Oxford, England, 1959.

[185] R. N. Bracewell and R. N. Bracewell, *The Fourier transform and its applications*, vol. 31999. McGraw-Hill New York, 1986.

[186] Y. Ohsone, G. Wu, J. Dryden, F. Zok, and A. Majumdar, "Optical measurement of thermal contact conductance between wafer-like thin solid samples," *Journal of heat transfer*, vol. 121, no. 4, pp. 954–963, 1999.

[187] A. Feldman, "Algorithm for solutions of the thermal diffusion equation in a stratified medium with a modulated heating source," *High Temperatures. High Pressures*, vol. 31, no. 3, pp. 293–298, 1999.